A BIOMATERIALS APPROACH TO INCREASING THE PERSISTENCE OF INDUCED NEURAL STEM CELLS IN THE GLIOBLASTOMA TUMOR RESECTION CAVITY

Hunter Nicole Bomba

A dissertation submitted to the faculty at the University of North Carolina at Chapel Hill in partial fulfillment of the requirements for the degree of Doctor of Philosophy in the Department of Pharmaceutical Sciences in the Eshelman School of Pharmacy.

Chapel Hill
2021

Approved by:

Aaron Anselmo

Brian Diekman

Ronit Freeman

Shawn Hingtgen

Juliane Nguyen

Kevin Sheets

ABSTRACT

Hunter Nicole Bomba: A Biomaterials Approach to Increasing the Persistence of Induced Neural Stem Cells in the Glioblastoma Tumor Resection Cavity
(Under the direction of Shawn Hingtgen)

Despite medical and technological advances, the survival statistics for patients diagnosed with glioblastoma have remained stagnant for more than three decades. The invasiveness and high recurrence rate of glioblastoma leave both local and systemic therapies ineffective and the median survival at an abysmal 12-15 months post-diagnosis. To combat this deadly disease, researchers have employed induced neural stem cells (iNSCs). Derived from a patient's fibroblasts, iNSCs have shown the remarkable ability to home to and kill distant tumor foci when engineered with lentiviruses encoding cytotoxic proteins and a stem cell-specific transcription factor. Yet, when injected into the brain parenchyma in a saline suspension, iNSCs are cleared in less than two weeks, thus limiting therapeutic durability. Previous studies have reported that by encapsulating iNSCs in a biomaterial matrix, persistence can be significantly improved. This dissertation explores how increasing the persistence of iNSCs *in vivo* impacts therapeutic durability and overall survival. Additionally, the safety and toxicity profile of iNSCs, delivered in both a biomaterial matrix and injected intracerebroventricularly, is characterized in a canine model. Lastly, a bio-inspired matrix for reducing cost and increasing throughput of cell therapy studies is presented.

This work is dedicated to my family, friends, and canine companions.
Thank you for everything.

ACKNOWLEDGEMENTS

First and foremost, I would like to thank the members of the Hingtgen Lab. To my fellow lab mates, thank you for the endless scientific support, brainstorming sessions, and laughter. Even on the tough days, you always offered encouragement, and I will be forever grateful for your friendship. I would like to specifically thank Alison Mercer-Smith and Shaye Hagler for their immeasurable kindness and unwavering support. To my undergraduate mentees, Abigail Carey-Ewend, Ingrid Findlay, and Morgan Goetz, thank you for your enthusiasm, hard work, and bold ideas. You were instrumental to the success of these projects, and I could not have done this without your help. Thank you for opportunity to be your mentor. I cannot wait to see what great things you accomplish, and I hope you continue to inspire and support the next generation of women in STEM. Finally, I would like to thank Dr. Shawn Hingtgen. I am incredibly grateful for the opportunity to work under your mentorship. You instilled in me the importance of translational science and keeping the patient at the forefront of discovery and innovation. Thank you for shaping me into the scientist I have become.

Karina Kinghorn, Carly Sanderson, and Rashmi Kumar, you are three of the most amazing women I know, and I am proud to know you. You are friends I now consider family. Thank you for listening to me, being there for me day and night, and offering reassurance when I needed it most. Abbey Augustine and Natalie Vranich, thank you for befriending me in middle school; I can't imagine not having you in my life.

Thank you to all of the dogs and dog owners who've come into my life. To my goldendoodle, Willis, thank you for always greeting me when I got home, cuddling with me after

a long day in lab, and reminding me that sometimes all you need is a long walk to clear your mind. To my second furchild, Pilot, thank you for being the goofball in my life I didn't know I needed. To Remi and Luke, I love you (almost) as much as I love Willis and Pilot. To my Canine Chemistry family, thank you for caring for Willis and me. Training sessions, pack walks, and get togethers are memories I will cherish forever.

I also owe a huge thanks to my family and mentors. To my parents, Ann Marie and David, thank you for helping me accomplish all of my goals. I cannot put into words how much I appreciate the countless science summer camps, traveling to attend TSA competitions, and pushing me to try new things. To my brother, Connor, and my grandmothers, Barbara Bomba and Judy Newton, thank you for never being more than a phone call away. I appreciate all of the visits, brunches, and inside jokes. Brandt Hutzel and Dr. Tanner Huffman, you are the best STEM educators in the country; I am honored to have been a student in your classrooms and this is as much your accomplishment as it is mine.

To my fiancé, Alexander Rackl, thank you for loving and supporting me for the past seven years. You believed in me and encouraged me even when the imposter syndrome was at its worst. I am so grateful for the days you cooked me dinner when I was too tired after a long day of animal surgeries, the pots of coffee always at the ready, and the car rides to and from campus so I didn't have to wait for the bus. We've endured grueling engineering courses together and studied for what felt like days in EB III and Hunt Library. We survived graduate school and three years of a long-distance relationship together. I'm so proud of everything you've accomplished. You may be a rocket scientist, but remember, that don't impress me much. I think it's safe to say we're officially a power couple.

Grad school was tough. Grad school during the COVID-19 pandemic was even more challenging, but the combination of grad school, a pandemic, and undiagnosed chronic illnesses was at times unbearable. To my medical team, thank you for detecting the symptoms that other physicians missed for over a decade. I cannot express how thankful I am to have official diagnoses and effective treatments plans. You greatly improved my quality of life.

Lastly, I would like to thank the members of my committee and collaborators for their guidance and contributions to this work. Drs. Aaron Anselmo, Brian Diekman, Ronit Freeman, Juliane Nguyen, and especially Kevin Sheets provided mentorship, career advice, and excellent scientific guidance throughout this journey. Thank you to my collaborators: Sue Mecham, PhD; Jillian Perry, PhD; Addis Tessema, PhD; Rui Zhang, PhD; Juli Bago, PhD; Kathryn Moore, PhD; Elizabeth Graham-Gurysh, PhD; Chris Mariani, DVM, PhD; Laura Ruterbories; Simon Khagi, MD; and Matt Ewend, MD. I would also like to acknowledge the staff of the Biomedical Research Imaging Core, Chapel Hill Analytical and Nanofabrication Laboratory, Translational Pathology Lab, and Division of Comparative Medicine.

TABLE OF CONTENTS

LIST OF TABLES

LIST OF FIGURES

LIST OF ABBREVIATIONS

231-BR	MDA-MB-231-BR cell line
2D	two-dimensional
3D	three-dimensional
Ace-DEX	acetylated dextran
ALT	alanine aminotransferase
AST	aspartate aminotransferase
AUC	area under the curve
BBB	blood-brain barrier
BBM	bio-inspired brain matrix
BLI	bioluminescence imaging
$CaCl_2$	calcium chloride
CO_2	carbon dioxide
CLIP	continuous liquid interface production
CP	canine patient
CD	cytosine deaminase
CD44	cluster of differentiation 44
C-MYC	cellular myelocytomatosis
CSF	cerebrospinal fluid
CSPG4	chondroitin sulfate proteoglycan 4
CXCR4	chemokine receptor 4
DMEM	Dulbecco's Modified Eagle Medium
DOXY	doxycycline

EDTA	Ethylenediaminetetraacetic acid
EGF	epidermal growth factor
eGFP	enhanced green fluorescent protein
FBS	fetal bovine serum
FGFR2	fibroblast growth factor receptor 2
FLT1	Fms-related receptor tyrosine kinase 1
Fluc	firefly luciferase
FSE	fast spin echo
GBM	glioblastoma
GCV	ganciclovir
GCV-TP	ganciclovir triphosphate
GDNF	glial cell line-derived neurotropic factor
GFAP	glial fibrillary acidic protein
GFP	green fluorescent protein
HB1.F3	human-derived allogeneic neural stem cell line
HB1.F3.CD	human-derived allogeneic neural stem cell line expressing cytosine deaminase
HIF-1α	hypoxia-inducible factor 1α
HSPA5	heat shock protein family A member 5
hTERT	human telomerase reverse transcriptase
IC	intracerebrally
ICV	intracerebroventricular
iNSC	induced neural stem cell
IL-1R	interleukin-1 receptor

IL-6R	interleukin-6 receptor
IP	intraperitoneally
IV	intravenously
IVIS	*in vivo* fluorescent imaging system
KI67	marker of proliferation 67
LV	lentivirus
LSM	light-sheet microscopy
LT	left tumor
mCh	mCherry
MRI	magnetic resonance imaging
NANOG	a homeobox transcription factor
NESTIN	neuroepithelial stem cell marker
NHF1	normal human fibroblast
NIM	neural induction medium
NSC	neural stem cell
OCT	optimal cutting compound
P2RX7	P2X purinoceptor 7
PAX6	paired box 6
PBS	phosphate buffered saline
PIK3CD	phosphoinositide 3-kianse catalytic subunit delta
PLA	poly-L-lactic acid
PLAUR	plasminogen activator, urokinase receptor
PODXL	podocalyxin-like protein

po	oral administration
q	every
qd	every day
RARE	rapid acquisition with relaxation enhancement
RNAseq	ribonucleic acid sequencing
rtTA	reverse tetracycline-controlled transactivator
RT	right tumor
SEM	scanning electron microscope
SDC1	syndecan 1
SDF-1	stromal cell-derived factor 1
SOX2	SRY-box transcription factor 2
SOX9	SRY-box transcription factor 9
SQ	subcutaneous
STC1	stanniocalcin-1
SWI	susceptibility-weighted imaging
TK	thymidine kinase
TNC	tenascin C
TRAIL	tumor necrosis factor α-related apoptosis inducing ligand
TUBB3	tubulin βe class III
UV	ultraviolet
VCAM-1	vascular cell adhesion protein 1
VEGF	vascular endothelial growth factor
VGCV	valganciclovir

VMAC	vimentin-type intermediate filament-associated coiled-coil protein
v-myc	viral homolog of cellular myelocytomatosis
WBC	white blood cell
w/v	weight per volume

CHAPTER 1: INTRODUCTION

1.1. GLIOBLASTOMA

1.1.1. CLINICAL SIGNIFICANCE

Glioblastoma (GBM) is classified by the World Health Organization as a Grade IV tumor and can present *de novo* or as a derivative of a pre-existing tumor.[1,2] The median age of GBM diagnosis is approximately 64 and varies by sex, as males are nearly twice as likely to be diagnosed than females.[1,3] GBM is a complex disease with high rates of mortality. Moreover, GBM survival statistics have remained static for 30 years, leaving the median patient survival at an abysmal 15 months post-diagnosis.[1,4]

Several factors contribute to the complexity of GBM and subsequent dismal survival statistics. First, the blood-brain (BBB) barrier is a major hindrance to the delivery of systemic therapeutics. The BBB is composed of several cell types: astrocytes, pericytes, and endothelial cells which work together to form tight junctions.[5] Tight junctions, along with highly selective efflux transporters, work to maintain homeostasis in the brain and place strict limits on the types of molecules and proteins that can reach the brain parenchyma.[5–7] While the BBB plays an important role in protecting the brain, it poses a substantial drug delivery challenge. Larger, more hydrophilic drugs delivered systemically are unlikely to be transported across the BBB and reach target areas in the brain tissue.[5] Second, the invasive and diffusive nature of GBM makes surgical intervention arduous. GBM primarily presents as a singular tumor at disease onset, these tumor cells are highly migratory, and are known to cross into the contralateral hemisphere.[8] Surgical resection is most feasible in the initial stages of diagnosis when smaller, infiltrative tumor foci are

absent.[9] Third, GBM is classified as immunologically cold. The lack of infiltrative immune cells significantly reduces the anti-tumor response and poses risk for GBM recurrence.[10,11] Moreover, immunologically cold tumors like GBM have notoriously low mutational rates, which contributes to decreased neo-antigen presentation and decreased efficacy of immune checkpoint inhibitors.[12–14] Fourth, the overall GBM tumor microenvironment adds an additional layer of complexity. Histologically, the structure of GBM closely mimics that of glial cells, a major cell population in the brain.[15] Furthermore, the tumor and surrounding microenvironment contribute to increased and disorganized blood vessel formation, regions of necrosis, and abnormal cancer stem cell niches are present throughout the tumor.[16–18] Together, these components make for a complex tumor microenvironment.

Due to this pathophysiology, treatments for GBM patients have focused on highly cytotoxic radiation and chemotherapy. Currently, standard of care follows the Stupp protocol–maximal safe tumor resection surgery followed by radiotherapy and concomitant temozolomide.[9,19,20] While temozolomide is administered orally or intravenously (IV), a more direct therapeutic delivery strategy can also be used in patients with GBM.[21] Intracerebroventricular (ICV) reservoirs are often implanted at the time of tumor resection. These devices consist of a catheter that is fed through the parenchyma into the lateral ventricle; the catheter is connected to a reservoir that sits on top of the skull but below the skin. These devices, commonly referred to as Ommaya or Rickham reservoirs, are used to deliver chemotherapeutics directly into the cerebrospinal fluid (CSF) whilst avoiding challenges of the BBB.[22,23] More recently, the FDA approved tumor-treating fields as an adjuvant therapy for GBM patients.[24] The Optune® device emits tumor-treating fields which are pulses of electromagnetic waves which work to slow tumor cell proliferation by targeting rapidly dividing cells.[25] Despite these

interventions, GBM tumors inevitably recur and continue to invade the brain, resulting in decreased life spans and poor quality of life in patients.[9]

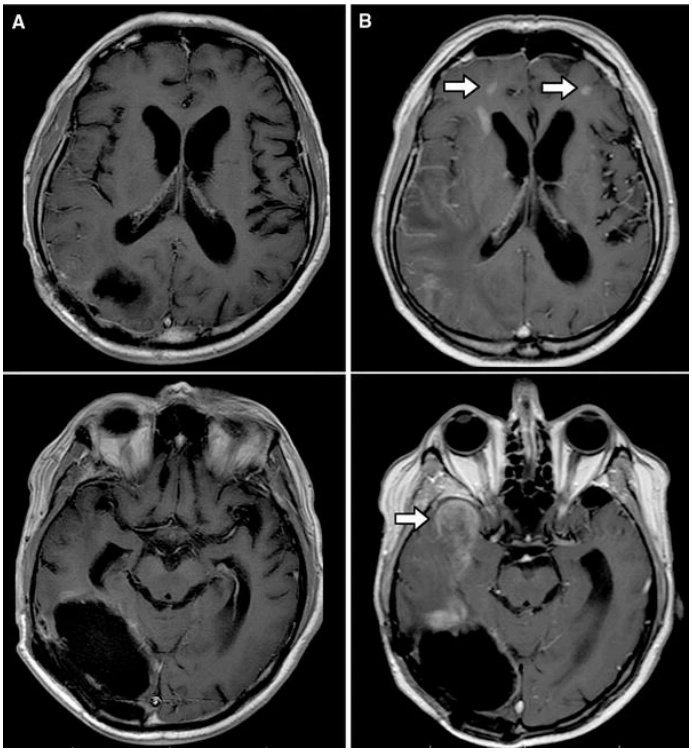

Figure 1.1. Magnetic Resonance Imaging of GBM. Scans of a patient (A) post-resection and (B) after receiving temozolomide and immunotherapy for 3 months. White arrows indicate regions of recurrence. Figure reproduce with permission from Springer and the Journal of Neuro-Oncology.[26]

1.1.2. *IN VITRO* AND *IN VIVO* MODELS OF GLIOBLASTOMA

The complexity of GBM makes studying the disease challenging, and this is clearly reflected in the models currently available (Table 1.1). To date, there is no 'best model' widely agreed upon by clinicians and researchers. Instead, scientists are tasked with selecting the model that is readily accessible, cost effective, and meets the needs of their study. Often, these criteria are met to the detriment of equally important criteria like clinical relevance.

Table 1.1. Models of GBM.

Category	Model	Origin	Considerations	References
Cell Lines	A172	Human	Not classified at tumorigenic by ATCC	27,28
	LN18	Human	Produce high levels of fibronectin	27,29,30
	LN229	Human	Forms vascularized tumors *in vivo*	27,31
	U87	Human	Does not mimic tumor invasion observed clinically. Fully sequenced genome.	27,32,33
	T98G	Human	Not classified at tumorigenic by ATCC	33,34
	U251	Human	Potentially cross-contaminated with other GBM lines.	35,36
	M059K	Human	Untreated GBM tumor. Cells grown from culture of excised tumor sample.	37,38
	M059J	Human	Same patient sample as M059K. Tumor sample was enzymatically dissociated prior to culture.	27,38
	GBM8	Human	Invasive tumor that mimics clinical observations.	38
	C6	Wistar Rat	N-ethyl-nitrosourea-induced glioma	27,32
	F98	Fischer Rat	N-ethyl-nitrosourea-induced glioma. Invasive tumor that mimics clinical observations.	27,39,40
	9L	Fischer Rat	N-ethyl-nitrosourea-induced glioma. Tumor can be established in Winstar rats.	32,39
	BT4C	BD IX Rat	N-ethyl-nitrosourea-induced glioma. High cellularity and irregular vasculature.	32,39
	RT-2	Fischer Rat	Avian sarcoma virus-induced glioma	39
	RG2	Fischer Rat	N-ethyl-nitrosourea-induced glioma	27,32,39
	GL261	C57BL/6N Mouse	3-methylcholantrene-induced glioma	32,41,42
	GL26	C57BL/6N Mouse	3-methylcholantrene-induced glioma. Increased necrosis and vascularity compared to GL261.	41,42
	CT-2A	C57BL/6J Mouse	Methylcholanthrene-induced glioma	41,43
	P560	VM/Dk Mouse	Isolated from a spontaneous tumor	44,45
In vivo	Xenograft	Varies	Immunocompromised animal may be required	
	Patient Derived Xenograft	Human	Must use immunocompromised animal model to avoid rejection	41
	Genetically Modified	Mouse	Investigate oncogenic genes of interest, expensive	41,46
	Spontaneous	Canine	Time to establish tumors and inevitable variability amongst animals	47
Ex vivo	Organotypic Tissue Slices	Rat	Improved modeling over plastic culture dishes, high throughput	35,41,48,49
	Organoids	Varies	High throughput	37,41
Synthetic	Tissue-mimicking	Polymer	Cost-effective and high throughput. Lack critical biologic features.	37,50,51

1.2. STEM CELL THERAPY FOR THE TREATMENT OF GLIOBLASTOMA

1.2.1. ALLOGENEIC NEURAL STEM CELL THERAPY

Neural stem cells (NSCs) are found in the subventricular and subgranular zones of adult brain tissue.[17,52,53] To isolate NSCs, biopsies from the NSC-rich regions of the brain must first be obtained.[54] The biopsy is then placed into an enzymatic digestion medium to dissociate the cells and create a single cell suspension. Finally, the NSCs are segregated from the pool using fluorescence-activated cell sorting. While this process yields a homogeneous NSC population, it results in a low yield which then have to be substantially expanded in culture.[55,56] Ultimately, this process is inefficient and cannot be easily implemented in the clinic.

To circumvent the challenges of isolating autologous NSCs, researchers established an allogeneic NSC line. This cell line, known as HB1.F3, was generated by sequestering NSCs from human fetal brain tissue, immortalizing the cells with a v-myc oncogene, and finally selecting a specific clone.[57] *In vitro* studies demonstrated that the HB1.F3 cell line retained nestin and vimentin expression, two characteristic stem cell markers, after repeated passaging.[58,59] Additional *in vivo* studies demonstrated the ability of these cells to differentiate into astrocytes and neurons once engrafted into brain tissue, thus verifying their pluripotency.[58,60] However, what is most unique about NSCs is their innate ability to migrate to tumors.[61] Although the exact molecular mechanisms that drive tumoritropic NSC migration have yet to be elucidated, there is some evidence to suggest that cytokines released by the tumor, such as vascular endothelial growth (VEGF) and stromal cell-derived factor 1 (SDF-1), play a role.[61]

Researchers have already begun to exploit this migratory behavior to deliver cytotoxic payloads to distant tumor foci. However, it is important to note that HB1.F3 cells exhibited differences in their ability to reach the tumor foci based on route of administration, IV or

intracerebrally (IC), as well as dose. Interestingly, as the number of cells in a single dose increased, fewer cells ultimately reached tumor foci. Moreover, cells administered IC were significantly more likely to reach the tumor focus (≥50%) compared to cells administered IV (<2%). This study also noted that there is likely a minimum tumor volume threshold that must be reached in order to attract HB1.F3 cells; the authors hypothesized that the lower quantity of cytokines and immune cells in the smaller tumor microenvironment is likely the cause of this phenomena.[62] Nevertheless, understanding the migratory properties of NSCs is just one crucial component of the therapy; the cytotoxic capabilities of the cells are the second half of the equation.

HB1.F3 cells have been engineered to express cytosine deaminase (CD), fragmented human metalloproteinase-2, interferon type I-β, or carboxylesterase and has demonstrated efficacy against several cancers, including GBM.[61] Of these engineering strategies, HB1.F3 cells expressing CD (HB1.F3.CD) have shown immense potential in pre-clinical studies. In one study, immunocompromised mice were implanted with human GBM cells, and subsequently received one of three HB1.F3.CD cell dose levels 0.5 millimeters (mm) caudal-laterally to the tumor implantation site. Mice were then administered the prodrug 5-fluorocytosine intraperitoneally (IP) twice per day for five days followed by once per day for two days. Significantly smaller tumor volumes (15.5 μm^3) were observed in the mice that received NSCs and the prodrug compared to those that did not receive combination therapy (16.6 μm^3). Additionally, blood and tissue samples from mice were collected post-mortem for analysis, and importantly, no abnormal findings were observed.[63]

Due to the success of NSCs in pre-clinical models, several clinical trials have been conducted to better understand the safety and efficacy of allogeneic NSCs (NCT02015819, NCT03072134, NCT02192359, NCT01172964, NCT02055196).[64] Of these trials, NCT01172964

explored the safety and toxicity of HB1.F3.CD cells in HLA-matched recurrent human GBM patients. Secondary aims of the study sought to explore the immunogenicity as well as the migratory abilities of HB1.F3.CD cells. Of the enrolled GBM patients, 15 participated in the study, and 12 patients were evaluated for safety and toxicity measures. Patients consisted of both sexes and were 22 to 63 years old. Serial blood analyses confirmed the absence of anti-HB1.F3.CD antibodies, thus demonstrating safety and reduced risk of therapy clearance. The cells were also observed to migrate into the contralateral hemisphere in one patient. Furthermore, while efficacy was not an objective of this Phase I study, the investigators noted significance in overall survival between patients who received a higher dose (5×10^7) versus a lower dose (1×10^7) of cells.[65,66] Overall, this study validated the HB1.F3.CD cell line and laid the groundwork for future NSC clinical trials.

1.2.2. AUTOLOGOUS NEURAL STEM CELL THERAPY

While allogeneic NSCs have proven efficacious *in vitro* and have made headway in human clinical trials, autologous NSCs would substantially reduce the risk of an acute immune reaction and negate potential long-term toxicity.[67] As aforementioned, isolation of autologous NSCs is a tedious and laborious process, thus limiting the use of these cells clinically. However, recent advances in cellular engineering have allowed researchers to overcome this challenge.

In a novel approach, fibroblasts, a major cell population in the dermis of the skin, have been transformed into neural stem cell-like cells, known as induced neural stem cells (iNSCs), using a combination of genetic engineering and transdifferentiation techniques.[68,69] Using a normal newborn foreskin fibroblast cell line (NHF1), researchers transduced the cells to express SOX2, reverse tetracycline-controlled transactivator (rtTA), tumor necrosis factor-related apoptosis inducing ligand (TRAIL), and thymidine kinase (TK).[26,68,69] SOX2, a transcription factor, is a

defining marker of NSCs; it plays a vital role in regulating NSC proliferation, differentiation, and migration.[70,71] To temporally control the expression of SOX2, an rtTA promoter was used. Lastly, the anti-cancer proteins TRAIL and/or TK were constitutively expressed by the iNSCs. TRAIL binds to death receptors 4 and 5, which are over expressed on some glioma cells, and activates caspase-mediated apoptosis.[72,73] On the other hand, TK functions as part of a prodrug system with valganciclovir (VGCV). Following administration, VGCV is hydrolyzed and converted to ganciclovir (GCV). GCV is then converted to GCV monophosphate intracellularly. Then, GCV monophosphate is converted to GCV triphosphate via TK. Finally, GCV triphosphate inhibits DNA polymerase, subsequently inducing cellular apoptosis; this process not only kills the iNSC but also adjacent tumor cells via the bystander effect. Of note, all transductions were performed using replication-incompetent recombinant lentiviruses.[74]Also, while previous cell differentiation strategies have taken cells through the pluripotent stage, converting fibroblasts into iNSCs uses transdifferentiation.[75] By surpassing the pluripotent phase, the risk of teratoma formation is significantly reduced.[76,77] As a whole, the rational design of iNSCs provides several advantages over other cell types.

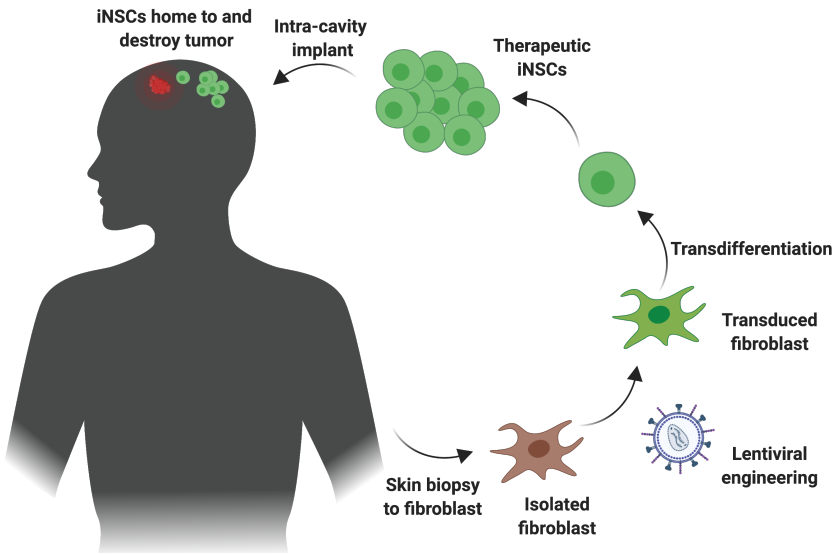

Figure 1.2. Autologous iNSC Production Process.

Furthermore, iNSCs exhibit robust anti-tumor properties. *In vitro*, iNSCs exhibit directional migration towards tumor cells whereas precursor fibroblasts and transduced fibroblasts migrate in a Brownian manner.[69] Co-culture assays have also demonstrated the efficacy TRAIL, TK, and combination therapy. Here, iNSCs are able to significantly reduce GBM tumor burden as early as 48 hrs after plating, and continued decline in tumor viability is observed through day seven.[68,69] The drug concentration, which is governed by the ratio of iNSCs to tumor cells, also plays an important role in time to response. As the ratio increases, the faster the tumor cells are eradicated. For example, when iNSCs and GBM cells are cultured in a ratio of 0.5:1, a 0.4-fold change in tumor viability is observed in three days; however, when cultured at a 4:1 ratio, the GBM cells are nearly completed killed in three days.[68] Importantly, these anti-tumor properties translate to a potent *in vivo* response as well. Using xenograft models of human GBM, iNSCs have been shown to migrate to the contralateral hemisphere containing a GBM tumor by day 21. Notably, mice treated with therapeutic iNSCs survived on average 34 days longer than mice receiving non-therapeutic iNSCs.[68]

In addition to assessing the migration and therapeutic potential of iNSCs, extensive genetic characterization has also been performed. Using ribonucleic acid sequencing (RNAseq), expression changes in genes involved in migration, differentiation, immune response, as well as others have been studied to compare fibroblasts and endogenous NSCs to iNSCs. Interestingly, iNSCs are phenotypic intermediates of fibroblasts and endogenous NSCs, with some gene expression levels more similar to those of fibroblasts (e.g. *CXCR4*, *FLT1*) and others mirroring those of endogenous iNSCs (e.g. *HIF1α*). Moreover, iNSCs were determined to have high expression of NESTIN and SOX2, two NSC markers, and importantly, when forced into differentiation, expressed low levels of NANOG and OCT-4, two pluripotency markers.[69] While

these experiments provided a first look at the genes involved in generating and maintaining an iNSC phenotype using NHF1s, subsequent studies have utilized primary human fibroblasts.

By studying the transdifferentiation of primary human fibroblasts, several key observations were made. First and foremost, inter-patient variability was observed in isolated fibroblasts prior to and following transdifferentiation. This variability included differences in proliferation rate, gene expression, and TRAIL output. When these patient-derived iNSCs were implanted into athymic nude mice bearing human xenograft GBM tumors, variations in therapeutic durability and survival were also observed. However, extensive RNAseq also identified possible quality control markers to identify iNSCs that are more likely to be stronger therapeutic candidates. These include proliferation genes (*NAMPT* and *IL1*), markers of transduction efficiency (TRAIL and SOX2), and migration genes (*SEMA3B*, *PIK3CD*, and *WWC1*).[78]

As a whole, autologous iNSCs have shown immense potential as a GBM therapy. These studies provided groundbreaking evidence to further propel iNSCs to the clinic. However, what remains to be shown is the safety of autologous iNSCs in an immune-competent, large animal model and the optimal delivery method.

1.3. DELIVERY OF NEURAL STEM CELL THERAPIES

To date, studies investigating scaffold systems have primarily reported on their regenerative medicine or tissue engineering capabilities – cartilage, bone, skin, and cardiac tissues being the most frequently reported.[79–83] The matrices are designed from a plethora of natural and synthetic materials with the goal of releasing a drug, growth factor, protein, and/or other agent to promote healing.[84–87] Researchers have pushed this framework even further and created cellularized scaffolds using a variety of cell types, ranging from fibroblasts to stem cells.[88] In these studies, the cells are intended to integrate into the host tissue while the scaffold simultaneously

integrates or degrades.[89–92] Moreover, a handful of cellular and acellular scaffold products have been approved by the FDA, including, but not limited to, MACI®[93], GINTUIT™ [94], TransCyte™ [93], and Osteoplug™ [93]. Other promising cellularized scaffolds products are currently in clinical trials (NCT04188262, NCT03258658, NCT04339764, NCT03463239).[95–98] While extensive research has been conducted to determine the ideal properties of scaffolds for tissue engineering and regenerative medicine, significantly less work has been published on the delivery of more specialized cells, like iNSCs, which need unobstructed pathways for migration in order to achieve their full therapeutic potential.

Given the success of iNSCs in early *in vivo* models, there is reason to believe that increasing the persistence of iNSCs would result in increased TRAIL AUC and subsequently improve survival outcomes. By encapsulating iNSCs in a biocompatible matrix, it is believed that the cells would be sheltered from the acute immune response in the post-surgical resection cavity.[99,100] While confined within the matrix, iNSCs could continuously secrete cytotoxic proteins to attack tumor cells in the immediate vicinity. Then, three to five days after resection, the iNSCs could migrate to tumor foci to produce a more durable, anti-tumor response. All the while, the material used to deliver the iNSCs could be engineered to further support the cells and reduce tumor burden.

A handful of studies have investigated this hypothesis. Early experiments employed electrospun poly-L-lactic (PLA), Gelfoam®, HySTEM™ , TISSEEL®, and acetylated dextran (Ace-DEX) scaffolds for the delivery of therapeutic stem cells.[69,101–104] When the stem cells are injected into the brain parenchyma in a saline suspension, nearly all are cleared 10 days post-implantation; however, stem cells seeded in PLA, Gelfoam®, HySTEM™ , TISSEEL®, and Ace-DEX scaffolds persisted out to 7, 19, 28+, 28, and 120 days, respectively.[69,101–104] To explore how

increased stem cell persistence correlated to survival outcomes, mice were implanted with GBM tumors. The tumors were then resected, leaving residual cells, to mimic clinical procedures. As hypothesized, the mice receiving encapsulated therapeutic cells survived, on average, 14, 15, and 21 days longer when treated with therapeutic stem cells on HySTEM™, Gelfoam®, and TISSEEL® scaffolds, respectively, compared to mice that received scaffolds containing non-therapeutic cells.[69,102,103] While these increases may seem trivial, they could correlate to significant survival outcomes improvements in human patients down the road, as newly developed therapies, like Optune®, are revered for their ability to increase median overall survival by 4.7 months.[105] Despite the substantial evidence to support the benefit of delivering iNSCs via a delivery matrix, the optimal material remains unknown.

1.4. SCOPE AND AIMS

GBM remains a terminal disease despite extensive research. Although allogeneic NSCs have been investigating extensively preclinically and have entered human patient trials, autologous iNSCs have yet to reach these milestones. To further propel autologous iNSCs to human clinical trials, this work investigated delivery strategies to optimize iNSC therapy and develop novel models to study GBM through the following aims:

1.4.1. AIM 1: CHARACTERIZE FLOSEAL AS A SCAFFOLD DELIVERY SYSTEM TO INCREASE PERSISTENCE OF iNSCs

In Aim 1, the use of FLOSEAL®, an FDA-approved hemostatic agent, is investigated for its utility in increasing the persistence of iNSCs in the tumor resection cavity, and how this impacts treatment efficacy. FLOSEAL®'s impact on iNSC gene expression profile is also explored.

1.4.2. AIM 2: DETERMINE THE SAFETY, TOXICITY, AND PERSISTENCE OF AUTOLOGOUS iNSCs IN A CANINE MODEL

In Aim 2, the safety profile of iNSCs is explored in an immune-competent canine model. Two, clinically relevant administration routes are used, intracerebroventricular infusion and FLOSEAL® scaffold implantation into the surgical resection cavity, as well as two dose levels.

1.4.3. AIM 3: DEVELOP A HIGH THROUGHPUT, COST-EFFECTIVE MODEL TO STUDY GBM AND EVALUATE STEM CELL THERAPIES

In Aim 3, bio-inspired matrices are developed with special considerations made for scale-up and optical imaging. Tumor growth, iNSC migration, and efficacy studies are used to evaluate the model as an alternative to animal studies.

CHAPTER 2: IMPACT OF A GELATIN-FIBRIN COMPOSITE SCAFFOLD ON INDUCED NEURAL STEM CELL PHENOTYPE, PERSISTENCE, AND EFFICACY

2.1. INTRODUCTION

Glioblastoma (GBM) is an aggressive, stage IV brain cancer and is the most common malignant brain tumor in adults.[106,107] Current standard of care includes tumor resection, radiation therapy, chemotherapy, and alternating electric field therapy.[108,109] However, complete tumor resection is often unachievable, as GBM is characterized by highly migratory cells that disperse far from the primary tumor mass, often into the contralateral hemisphere.[10,108] The aggressive, infiltrative nature of GBM results in a high mortality rate and a median patient survival of just 15 months.[106]

To combat the migratory nature of GBM, neural stem cells (NSCs) have been investigated as drug delivery vehicles due to their innate tumor-tropism. Several pre-clinical studies have investigated the persistence, migration, and efficacy of immortalized NSCs bearing a range of therapeutic agents in mice.[63,110,111] Moreover, immortalized, allogeneic NSC therapy has entered human clinical trials for the treatment of GBM (NCT02015819, NCT03072134, NCT01172964, NCT02055196, and NCT02192359).[112–116] While NSC therapy shows promise, harvesting a sufficient quantity of autologous NSCs is challenging, and immortalized, allogeneic cells pose an immunogenic risk and have potential for unrestrained proliferation.[117,118] We have improved upon NSC therapy by developing a rapid, single-transcription factor reprogramming that allows for the direct conversion of fibroblasts to NSCs, known as induced neural stem cells or iNSCs. Here, fibroblasts are isolated from patient skin and stably engineered with lentiviral constructs encoding

for the neural stem cell transcription factor *SOX2* and the cytotoxic protein TNFα-related apoptosis-inducing ligand (TRAIL). Transduced fibroblasts are then cultured in transdifferentiation media to produce therapeutic, tumor-homing iNSCs.[69]

While iNSCs are efficacious, persistence in the tumor resection cavity remains a limiting factor. When iNSCs are administered to the resection cavity in saline, more than 50% of iNSCs are cleared by day 10, and nearly all iNSCs are cleared by day 25 post-implantation.[69] To address this, previous studies have demonstrated that seeding mesenchymal stem cells on TISSEEL®, a fibrin product, and poly(l-lactic acid) significantly improves cell persistence compared to cells injected in saline.[102,119] Additionally, increased persistence of iNSCs has been observed when seeded on Gelfoam®, a gelatin matrix, compared to injection in saline.[120] However, the optimal characteristics of an iNSC delivery matrix and the relationship between efficacy and increased persistence remain unknown.

Herein, we investigated the use of the FDA-approved, hemostatic agent, FLOSEAL®, a gelatin and thrombin mixture, as a delivery matrix and its impact on iNSC persistence and efficacy. When subjected to an area with active bleeding, the thrombin component of FLOSEAL® polymerizes with circulating fibrinogen to form fibrin.[121,122] We postulated that this rapid polymerization would instantly encapsulate iNSCs, and the gelatin granules would swell to create a physical barrier, thus providing ample protection from the post-surgical immune response in the resection cavity. As FLOSEAL® degrades, the iNSCs would be expected to migrate out of the scaffold after the post-surgical immune response has subsided. We theorized that the 6- to 8-week resorption timeframe of FLOSEAL® would drastically improve iNSC persistence. In this study, we demonstrate that a FLOSEAL®-based transplant significantly improves iNSC persistence compared to Gelfoam®, TISSEEL®, and saline injection. The marked increase in persistence lead

to improved survival outcomes compared to control-treated animals using two unique GBM xenograft models, but extensions over therapeutic cells delivered without a scaffold were modest. These results indicate that persistence alone is inadequate as a predictive marker for therapeutic efficacy, and further research is needed to develop the optimal iNSC delivery matrix.

2.2. RESULTS

2.2.1. ENCAPSULATING CELLS IN FLOSEAL®

Figure 2.1A depicts the scaffold fabrication process. First, acellular FLOSEAL® scaffolds were observed via SEM. The gelatin particles in the FLOSEAL® kit were found to be heterogeneous in shape and size; on average, particles were determined to be 250 μm at their largest dimension (Fig. 2.1Bi). When combined with thrombin and polymerized with fibrinogen, the gelatin particles become wrapped in a fibrin web (Figure 2.1Bii-iii). Similar to the gelatin particles, iNSCs were also found to be encased in the fibrin web, and this cell-fibrin network encases the gelatin particles (Fig. 2.1Ci-iii).

2.2.2. SEEDING EFFICIENCY

After understanding the interaction between cells and FLOSEAL®, seeding efficiency, defined as the number of cells calculated to be in the scaffold divided by the theoretical cell count, was determined. FLOSEAL® scaffolds were determined to have a 43.43% ± 17.40% seeding efficiency on average. The total concentration of DNA per sample was 10.6 ng/μL ± 3.5 ng/μL (Fig. 2.1D). Each batch of FLOSEAL® produces six scaffolds contained in a single syringe. To ensure consistency between samples, the seeding variability between scaffolds was also analyzed. The DNA concentration was found to be 12±7, 9±3, 9±2, 10±3, 12±5, and 10±1 ng/μL for scaffolds plated first through sixth, respectively, using linear regression. The total number of cells was found to be $4.99\times10^5\pm3.20\times10^5$, $4.46\times10^5\pm2.11\times10^5$, $3.68\times10^5\pm1.23\times10^5$,

$3.83\times10^5\pm1.48\times10^5$, $4.89\times10^5\pm2.25\times10^5$, and $4.21\times10^5\pm0.30\times10^5$ for scaffolds plated first through sixth, respectively. Importantly, no statistical significance was observed between any comparison by one-way ANOVA with Šidák correction (Fig. 2.1E).

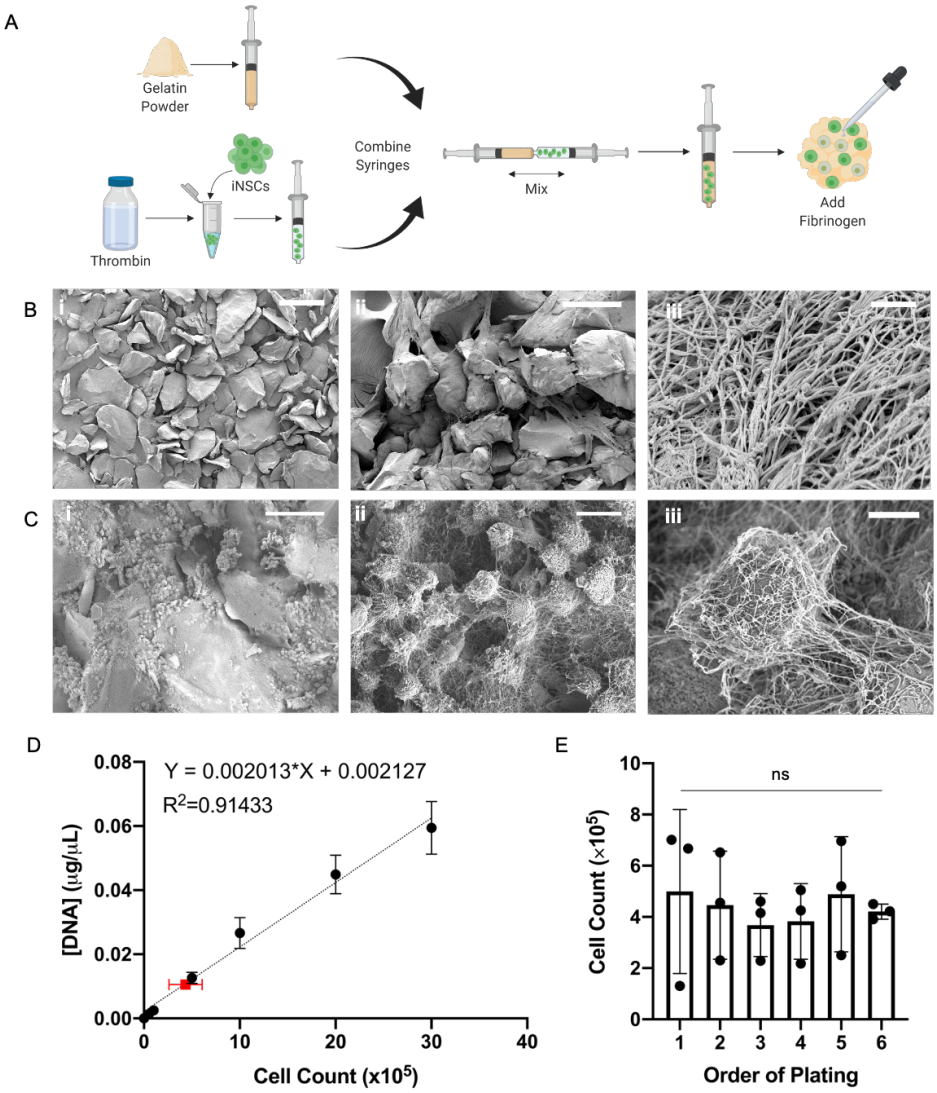

Figure 2.1. FLOSEAL® Material Characterization. A) Schematic depicting FLOSEAL® scaffold fabrication. B) SEM images of i) dry gelatin particulate (Scale bar, 500 µm), ii) FLOSEAL® scaffold (Scale bar, 200 µm), and iii) fibrin clot structure (Scale bar, 1 µm). C) SEM images of i) gelatin, fibrin, and iNSCs (Scale bar, 200 µm), ii) multiple iNSCs entrapped in fibrin (Scale bar, 10 µm), iii) high magnification view of a single iNSC trapped in fibrin (Scale Bar, 5 µm). D) Seeding efficiency of fibroblasts in FLOSEAL quantified via DNA concentration. Black points represent standard curve (n=3 per cell density). Red point represents average cell count and DNA concentration of FLOSEAL® samples (n=18). E) Impact of plating order on the number of cells in each scaffold; all comparisons not significant. Data presented as mean ± standard deviation.

2.2.3. IMPACT OF FLOSEAL® ON iNSC GENE EXPRESSION

Previous studies have shown that a material's physiochemical properties can influence gene expression, particularly as it relates to markers of differentiation, proliferation, and migration.[123–126] To understand FLOSEAL®'s transcriptomic impact, therapeutic iNSCs were encapsulated in FLOSEAL® and cultured up to two weeks in the matrix using transwell inserts, which prevents dissolution of the scaffold in liquid media, to study how the material influenced iNSC gene expression (Fig. 2.2A). Gene expression of iNSCs in scaffolds was compared to both non-transdifferentiated fibroblasts (Fig. 2.4A-F) and to day 0 iNSCs (Fig. 2.2B-G). 'Day 0 iNSCs' denotes fibroblasts that have been transduced and transdifferentiated to become iNSCs but not placed into a scaffold. Neural stem cell (NSC), differentiation, proliferation, pluripotency, migration, therapy, and anti-apoptosis markers were monitored. The differentiation markers, namely *GFAP*, *TUBB3*, and *VMAC*, were found to remain fairly constant in their expression levels over time, but downregulated compared to the day 0 iNSCs (Fig. 2.2B). Of the NSC markers, *NESTIN* was the only one found to be upregulated (Fig. 2.2C). All pluripotency markers were downregulated; however, *NANOG* was virtually unchanged at the day 7 and 14 timepoints (Fig. 2.2D). Interestingly, *Ki67* and *IL-1R*, two proliferation markers, were also downregulated (Fig. 2.2E). Of note, *TRAIL* and *HSPA5*, an anti-apoptosis marker, were downregulated (Fig. 2.2F). Lastly, we observed wide variability in the expression of migration markers (Fig, 2.2G). *SOX2*, *P2RX7*, *STC1*, *VCAM-1*, *FLT-1*, and *CXCR4* were the most profound upregulations observed.

To further confirm our findings, we opted to repeat this experiment using three unique batches of iNSCs for the day 14 timepoint. In sharp contrast to the findings presented in Fig. 2.2B, *GFAP* was upregulated while *TUBB3* and *VMAC* remained downregulated (Fig. 2.3A). Similar to the first gene expression experiment, *NESTIN* was the only NSC marker to be upregulated, and similar trends were observed for *NANOG* (Fig. 2.3B-C). The proliferation, anti-apoptosis, and therapy

markers remained downregulated as well (Fig. 2.3D-E). As for the migration genes, similar trends were observed wherein *SOX2*, *STC1*, *VCAM-1*, *FLT-1*, and *CXCR4* were upregulated; however, *P2RX7* was slightly downregulated in this experiment (Fig. 2.3F).

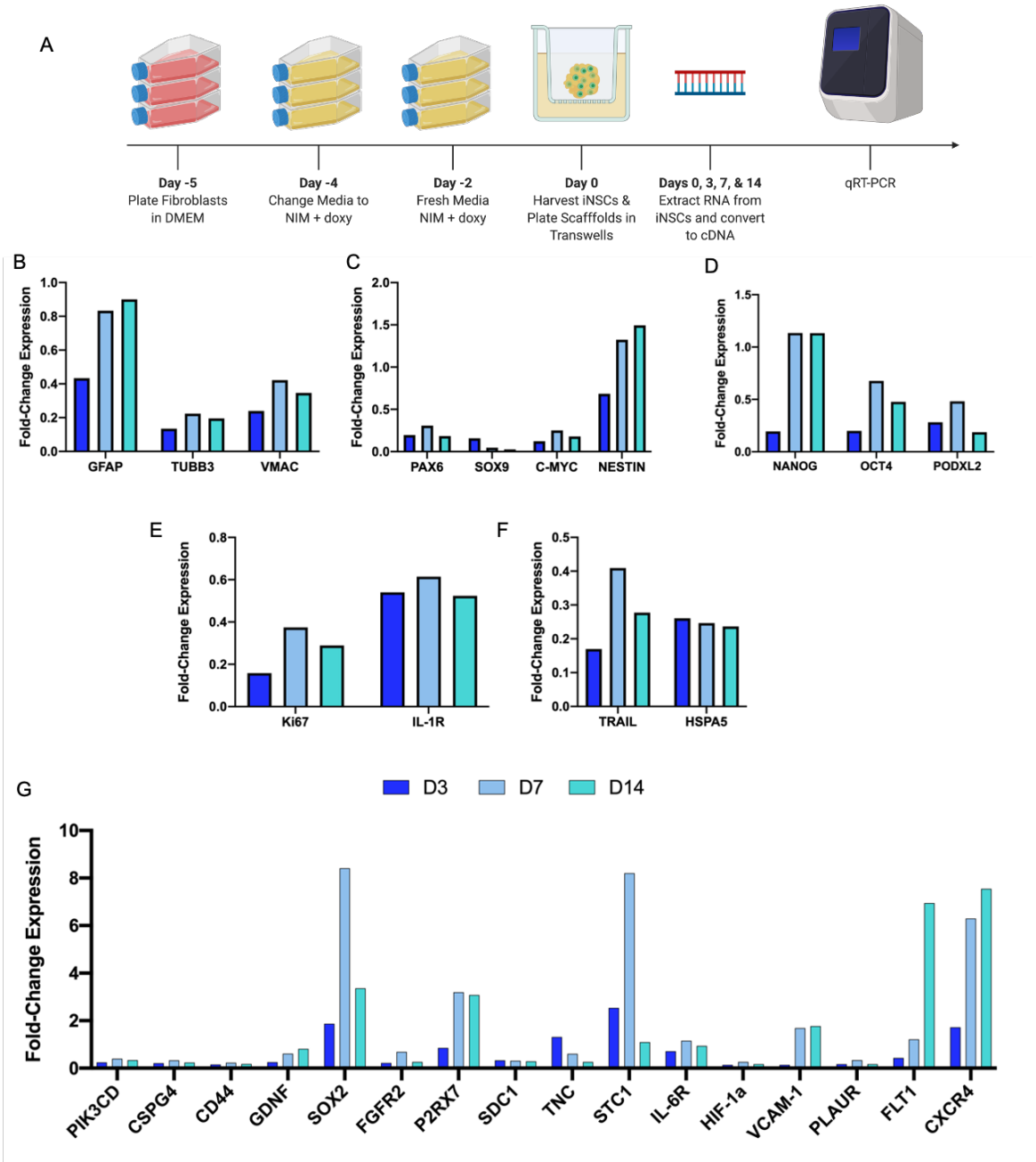

Figure 2.2. Impact of FLOSEAL® on iNSC Phenotype Over Time. A) qRT-PCR experimental design. Gene expression of iNSCs in FLOSEAL® relative to day 0 iNSCs for B) differentiation, C) NSC, D) pluripotency, E) proliferation, F) other, and G) migration markers (5 scaffolds pooled per time point).

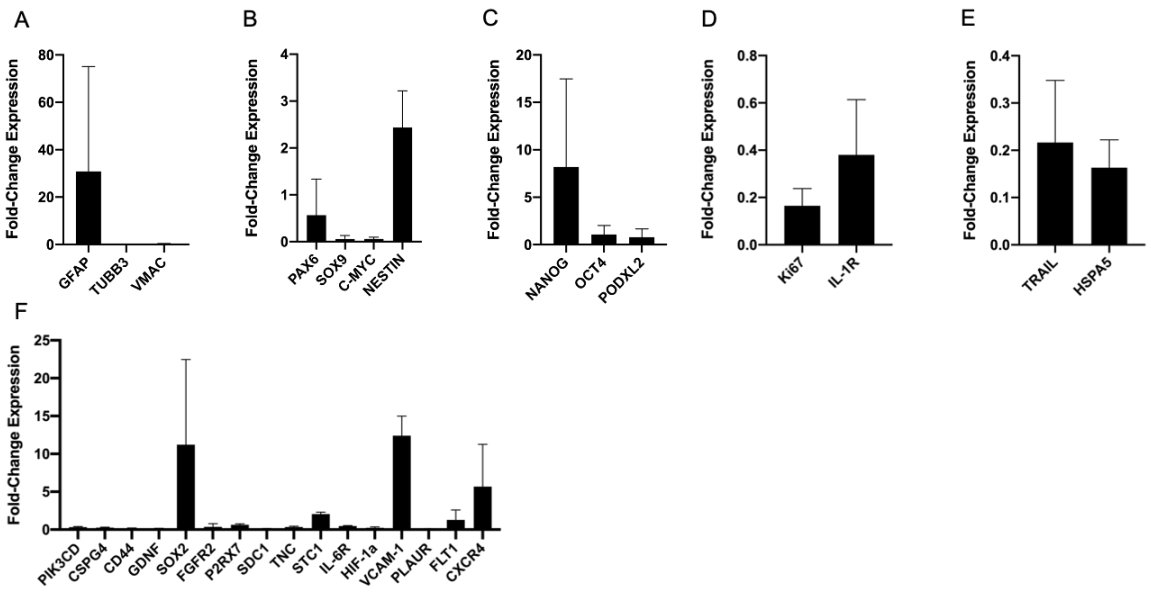

Figure 2.3. Impact of FLOSEAL® on Day 14 iNSC Gene Expression. Gene expression of iNSCs in FLOSEAL® relative to day 0 iNSCs for A) differentiation, B) NSC, C) pluripotency, D) proliferation, E) other, and F) migration markers (n=3 iNSC batches, 6 scaffolds pooled per batch).

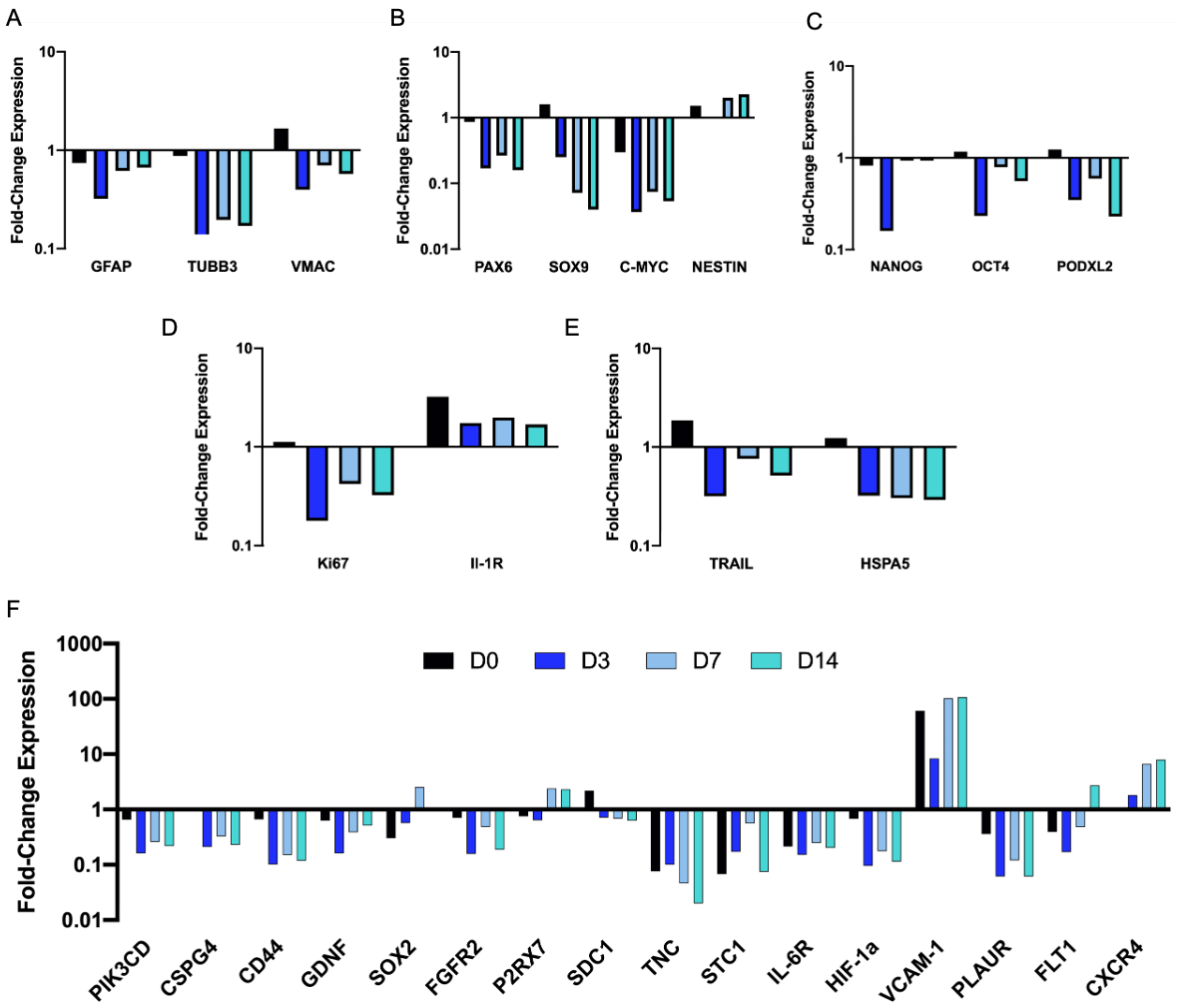

Figure 2.4. Impact of FLOSEAL® on iNSC Phenotype Over Time. A) qRT-PCR experimental design. Gene expression of iNSCs in FLOSEAL® relative to day NHF1-hTERT-SOX2-rtTA-GFP-TRAIL cells for B) differentiation, C) NSC, D) pluripotency, E) proliferation, F) other, and G) migration markers (5 scaffolds pooled per time point).

2.2.3. IN VIVO iNSC PERSISTENCE

Next, we sought to compare the persistence of non-therapeutic iNSCs using four different implantation techniques: direct injection or encapsulation in FLOSEAL®, TISSEEL®, or Gelfoam®. Using bioluminescence imaging (BLI), we observed significant differences in Fluc-tagged iNSC persistence. iNSCs encapsulated in FLOSEAL® persisted significantly longer than iNSCs implanted via direct injection, TISSEEL®, or Gelfoam®. In FLOSEAL®, iNSCs appear

to proliferate 21-fold by day 23 post-implantation and show strong BLI signal 95 days post-implantation. In contrast, iNSCs encapsulated in Gelfoam® and TISSEEL® show near complete clearance on or before day 20 and little proliferation is observed (Fig. 2.5A-B). iNSCs delivered by direct injection in 1X PBS showed near background signal by day 20, also indicating significant clearance. Mice implanted with iNSCs encapsulated in FLOSEAL® were euthanized on day 95, and brains were harvested for analysis. Significantly, iNSCs remained clustered in the mock resection cavity at this time (Fig. 2.5C).

2.2.4. IN VIVO iNSC EFFICACY

After observing significantly improved iNSC persistence with the aid of FLOSEAL®, we sought to determine if increased persistence correlated to enhanced therapeutic durability and improved survival in mice. We first tested therapeutic durability using the GBM line GBM8. This tumor line was selected for its ability to mimic the invasive nature of tumors seen in the clinic. Three days after implantation, tumors were resected to reflect clinical procedures and treatments were administered into the resection cavity. Tumor size was monitored over time via BLI (Fig. 2.6A). Mice treated with iNSCs encapsulated in FLOSEAL® initially showed steady tumor growth; however, by day 25, some mice began to show decreased tumor growth (Fig. 2.6B, E). The direct injection and TISSEEL® groups showed an initial decrease in tumor volume over the first 5-10 days; however, this was followed by exponential tumor volume increase in the proceeding days (Fig. 2.6C-D). Mice administered non-therapeutic iNSCs displayed rapid tumor growth and significantly shorter lifespans compared to all other groups (Fig. 2.6F-G). In contrast, mice treated with therapeutic iNSCs survived significantly longer compared to mice treated with non-therapeutic iNSCs. The FLOSEAL® low TRAIL ($P=0.030$), FLOSEAL® high TRAIL ($P=0.010$), and TISSEEL® TRAIL ($P=0.022$) groups all survived significantly longer compared to the FLOSEAL® control group. Despite a trend, a significant difference was not observed in

survival between the mice treated with a direct injection of therapeutic iNSCs and the FLOSEAL® high TRAIL (P=0.704) or FLOSEAL® low TRAIL groups. (P=0.4595).

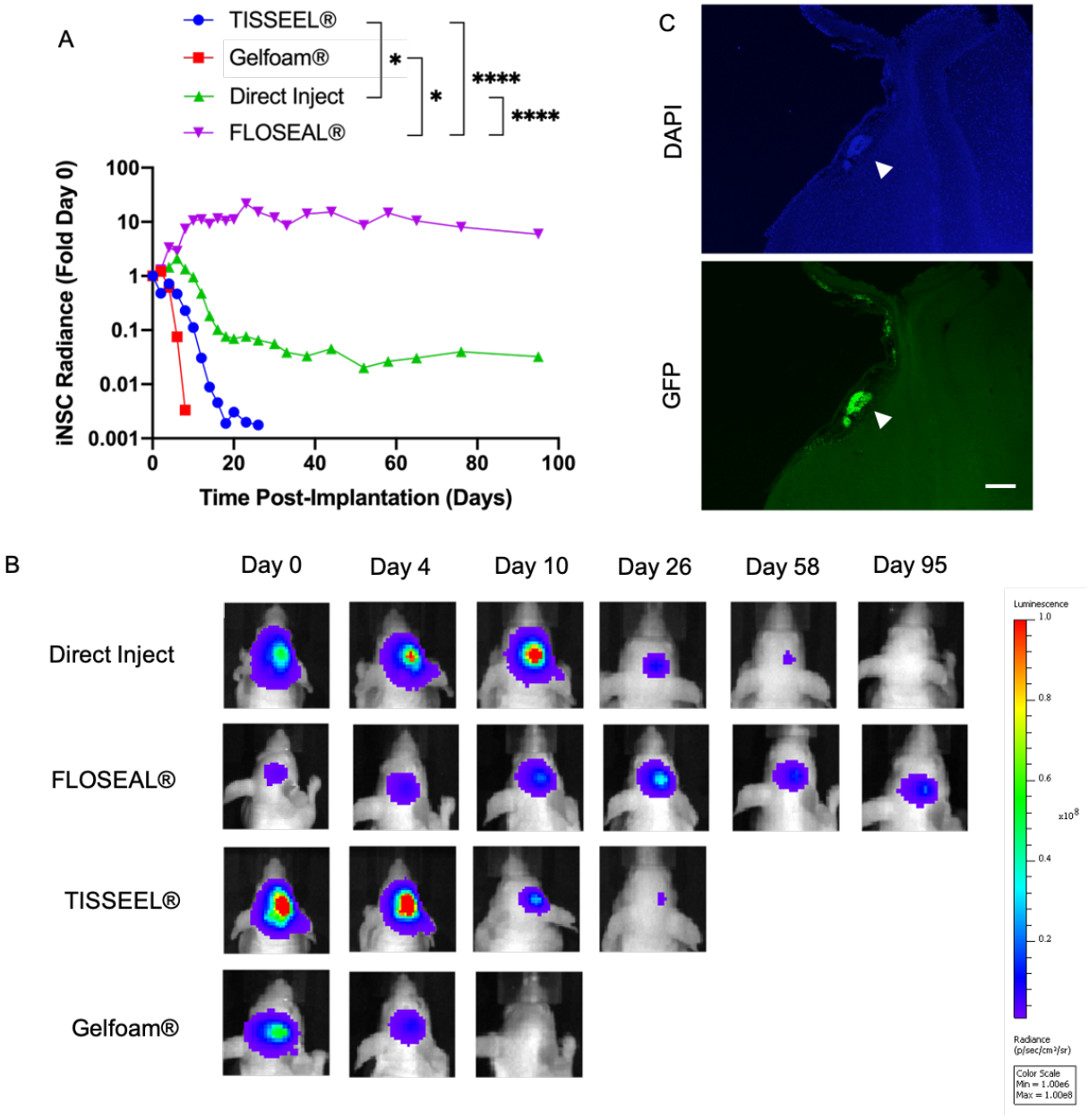

Figure 2.5. In vivo Persistence of Cells Encapsulated in FLOSEAL®. A) Fold change in BLI signal of non-therapeutic iNSCs over time (n=5 per group) (* indicates P<0.05; **** indicates P<0.0001). B) Representative BLI images. C) Fluorescent images of non-therapeutic iNSCs in FLOSEAL® (arrow) 95 days post implantation (Scale bar, 200 µm).

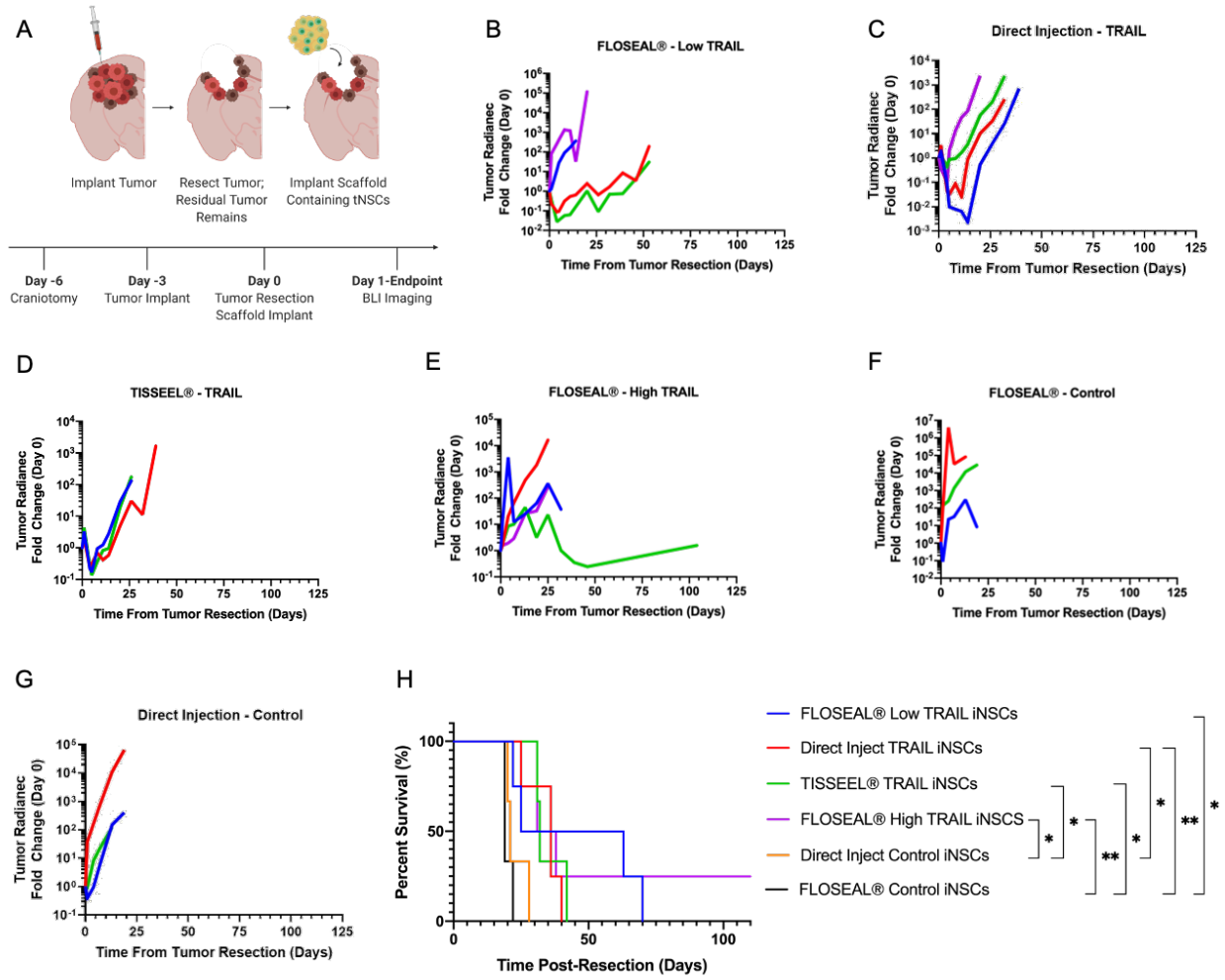

Figure 2.6. In vivo Efficacy of iNSCs Encapsulated in FLOSEAL® Against GBM8 Tumor. A) Schematic of surgical procedure and timeline. B) Fold change in GBM8 tumor radiance of mice treated with low dose of TRAIL iNSCs encapsulated in FLOSEAL® (n=4), C) direct injection of TRAIL iNSCs (n=4), D) TRAIL iNSCs encapsulated in fibrin (n=3), E) high dose of TRAIL iNSCs encapsulated in FLOSEAL® (n=4), F) direct injection of control, non-therapeutic iNSCs (n=3), and G) control, non-therapeutic iNSCs encapsulated in FLOSEAL® (n=3). Each line represents one mouse. H) Kaplan-Meier survival curve of mice implanted with GBM8 tumors (* indicates $P<0.05$; ** indicates $P<0.01$).

We next tested a second GBM tumor model using the U87 cell line to mimic the primary non-migratory tumor mass seen clinically. Seven days after tumor implantation, the tumors were resected, and iNSC therapies were administered into the resection cavity (Fig. 2.7A). Mice were treated with a direct injection of therapeutic iNSCs in suspension, therapeutic iNSCs encapsulated in FLOSEAL®, or control (non-therapeutic) iNSCs encapsulated in FLOSEAL®. Fig. 7B depicts the fluorescence-guided tumor resection and implant of the scaffold. Mice treated with a direct injection of therapeutic cells exhibited exponential tumor growth following treatment; however, one mouse in this group displayed an initial decrease in tumor volume followed by an increase in tumor volume (Fig. 2.7D). Mice administered therapeutic iNSCs in FLOSEAL® showed different responses within the group. While 70% of mice showed progressive tumor growth within the first 25 days and ultimately succumbed to tumor burden, 30% of mice displayed slower tumor growth and survived beyond 100 days (Fig. 2.7 C, F). As anticipated, mice administered non-therapeutic iNSCs encapsulated in FLOSEAL® displayed no tumor suppression (Fig. 2.7E). Despite differences in the tumor progression, no significant differences in survival were observed between any group comparison.

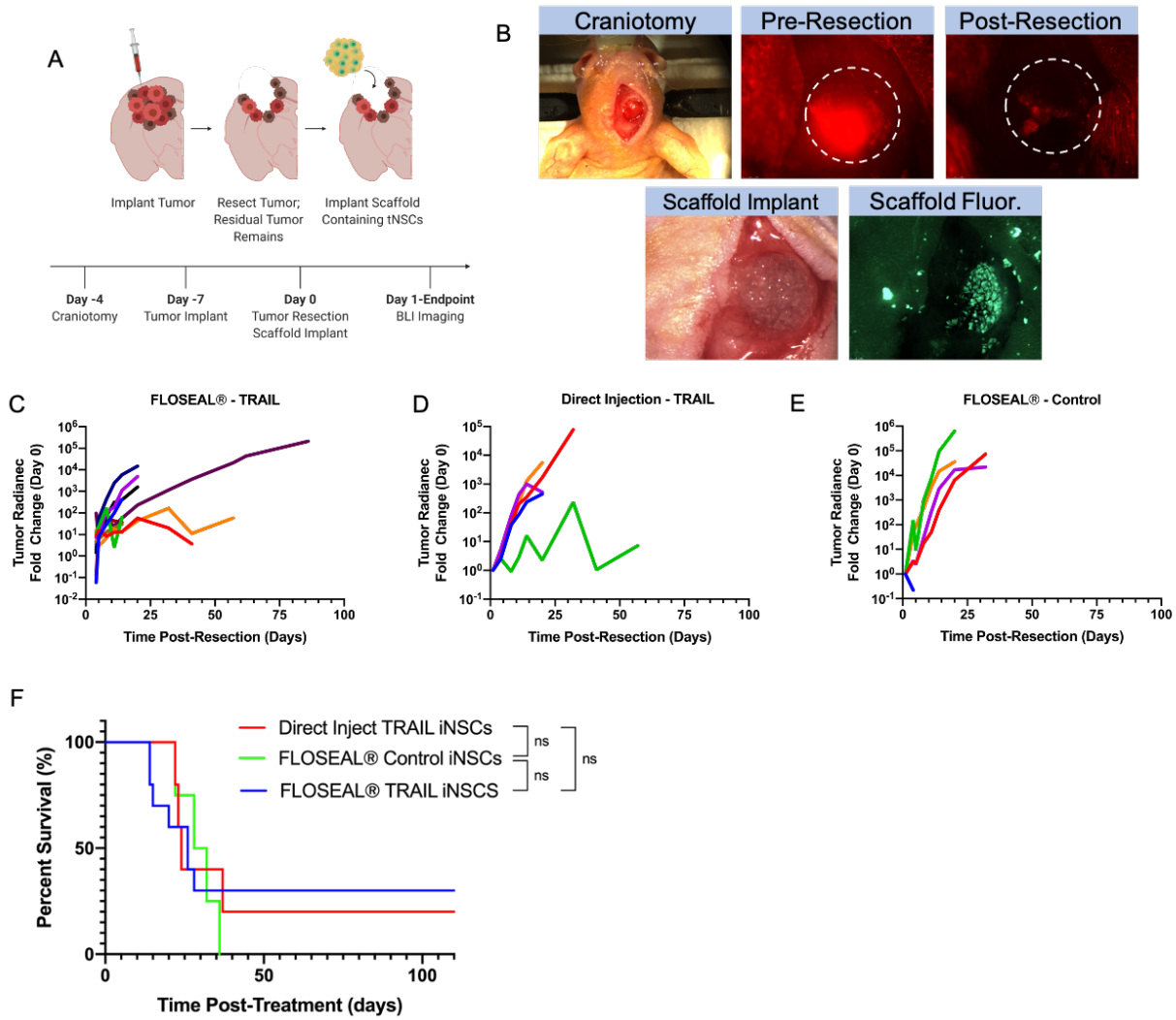

Figure 2.7. In vivo Efficacy of iNSCs Encapsulated in FLOSEAL® Against U87 Tumor. A) Schematic of surgical procedure and timeline. B) *In vivo* surgical images of craniotomy, tumor resection, and FLOSEAL® scaffold implantation. C) Fold change in U87 tumor radiance of mice treated with TRAIL iNSCs encapsulated in FLOSEAL® (n=10), D) direct injection of TRAIL iNSCs (n=5), and E) control, nontherapeutic iNSCs encapsulated in FLOSEAL® (n=5). F) Kaplan-Meier survival curve of mice implanted with U87 tumors (ns indicates not significant).

2.3. DISCUSSION

Previous work by our group has demonstrated the benefit of delivery matrices to increase NSC persistence in the tumor resection cavity.[69,102,119,127] While Gelfoam®, TISEEL®, and HySTEM™ each statistically improved NSC persistence compared to direct inject controls, iNSCs

still failed to persist beyond 28 days.[69,102,119,127] In tumors such as GBM where recurrence is inevitable, there is a strong need to have the iNSCs persist long enough to migrate vast distances across the brain while still constantly producing their therapeutic payload. To achieve this goal, we sought to combine the best features of previous materials, specifically taking into account biocompatibility, cell binding sites, ease of fabrication, and handleability. Based on these criteria, we selected FLOSEAL® as our candidate matrix.

As an FDA-approved hemostatic product, FLOSEAL®'s intrinsic features make it a desirable scaffold material. The two principal components of FLOSEAL®, gelatin and thrombin, are biocompatible – gelatin as denatured collagen, and thrombin as a critical component of the coagulation cascade.[128,129] With gelatin and thrombin as the principal ingredients, FLOSEAL® is completely resorbed in patients within 8 weeks and encapsulated NSCs are unlikely to be obstructed by fibrotic encapsulation.[120,130] For this study, we scaled back the gelatin and thrombin components from the FLOSEAL® kit produce smaller scaffold volumes while keeping the ratio of the components the same as that used clinically. With this formulation, we observed rapid encapsulation of iNSCs in FLOSEAL®. While the gelatin component of FLOSEAL® is rich in RGD sequences, which promotes cell adhesion,[131] the rapid reaction of thrombin with fibrinogen completely wrapped the iNSCs in a fibrin web with insufficient time to adhere to gelatin particles.

Furthermore, we observed consistent iNSC density across scaffolds. Because the total volume of gelatin and thrombin (86 mg and 500 uL, respectively) presented here produces enough material to make six scaffolds, we were initially concerned the gelatin particles would be compressed during ejection from the syringe, such that the thrombin and cell solution would be ejected first, therefore producing scaffolds that were initially more liquid and had a higher cell density than those ejected last. Although the first three scaffolds plated were more liquid in nature,

no statistical differences were observed in the cell densities, thus ensuring consistent dosing between scaffolds.

Given the volume of literature on the impact of material properties on stem cell proliferation, differentiation, and migration, we sought to understand the impact of FLOSEAL® on iNSC gene expression. In accordance with previous studies, downregulation of *NANOG* and upregulation *NESTIN* and *SOX2* were observed compared to fibroblasts.[69] Downregulation of *GFAP*, *TUBB3*, and *VMAC* suggest that FLOSEAL® is not inducing differentiation to glial cells or neurons and the iNSCs have transitioned away from a fibroblast phenotype. Surprisingly, *TRAIL* was found to be downregulated at all time points after seeding in FLOSEAL®. However, iNSCs were engineered to secrete TRAIL under a constitutive promoter; therefore, additional investigation is needed to elucidate these changes. Interestingly, *KI67 and IL-1R* were found to be downregulated. Moreover, downregulation of the anti-apoptosis gene *HSPA5* was also observed. Despite these findings, we observed a noticeable increase in iNSC signal in our persistence study, indicating that additional signaling factors and interaction *in vivo* contribute to the iNSC proliferation. Undeniably, there are limitations to this experimental design. The synthetic transwell culture system lacks many components of the *in vivo* environment that the iNSCs would be exposed to, specifically, cytokines, chemokines, immune cells, and tumor cells.[132,133] Therefore, due to insufficient external stimuli, it is unsurprising that a number of the migration genes probed were downregulated. However, the substantial upregulation of *SOX2*, *P2RX7*, *STC1*, *VCAM-1*, *FLT1*, and *CXCR4* suggests that these genes may serve as quality control markers in iNSC therapy optimization and scale-up. Notably, studies have demonstrated that post-transcriptional, translational, and degradation processes may play an equally important role in protein expression, and findings elucidated from mRNA should be interpreted with caution.[134] Future studies will

explore changes in iNSC gene expression when encapsulated in FLOSEAL® in immune-competent mice to understand the impact of the resection cavity microenvironment.

Despite our initial hypothesis that the principal role of gelatin particles would be for iNSC adhesion, gelatin appears to have played a separate role in iNSC persistence. One of the key features of FLOSEAL® as a hemostatic matrix is its ability to expand as a means of compressing and sealing off sources of active bleeding. Based on our remarkable persistence data, we believe the gelatin particles acted as a physical barrier, protecting the iNSCs from immune clearance. While cells persist in Gelfoam® significantly longer compared to previously tested scaffold materials,[103] we theorize that the lack of persistence of iNSCs in Gelfoam® in the present study is due to poor cell attachment and insufficient penetrance into deeper pores. TISSEEL® also severely underperformed in comparison to FLOSEAL®. Importantly, the BLI signal was confirmed via fluorescence in post-mortem brain tissue sections. Given the lack of tumor, and its associated chemokines to promote iNSC migration, it is not surprising to see the iNSCs clustered in the resection cavity after euthanasia on day 95.

Lastly, we investigated if increased iNSC persistence obtained with FLOSEAL® resulted in enhanced therapeutic durability and improved survival outcomes. For these studies, we selected two distinct GBM tumor models, GBM8 and U87. Although both tumors proliferate rapidly *in vivo*, neither alone fully mimics what is observed clinically; the U87 cell line produces a dense tumor sphere while the GBM8 cell line results in a diffuse tumor that invades both hemispheres. It is also important to note that GBM8 cells are more sensitive to TRAIL therapy than U87 cells.[135,136] These attributes explain, at least in part, the differences observed in therapeutic durability and mouse survival observed in the GBM-8- and U87-bearing mice. Therapeutic iNSCs injected in suspension into the resection cavity provide immediate tumor suppression, but they

lack the persistence to provide a durable response. On the other hand, therapeutic iNSCs encapsulated in FLOSEAL® do not provide immediate tumor suppression, but the FLOSEAL® matrix appears to offer a prolonged therapeutic effect beyond 25 days in select cases. FLOSEAL®'s lack of initial burst release likely explains its inability to significantly reduce tumor volume initially. For all *in vivo* studies, as noted in the materials and methods section, cell densities in FLOSEAL® scaffolds were theoretical calculations made by obtaining a desired cell concentration and assuming equal division amongst the number of scaffolds made. However, the seeding efficiency data shows that only a 43% seeding efficiency is achieved on average. Therefore, the persistence and efficacy studies were conducted using less than desired cell doses, but despite this, promising trends were observed in therapeutic durability and survival. Based on these results, there is a clear need for a delivery matrix that allows for an initial burst release of iNSCs to combat tumor cells in the immediate vicinity of the resection cavity and sustained release of iNSCs to support therapeutic durability. Future studies will explore how a combinatory burst release and sustained release of iNSCs impacts therapeutic durability as well as the impact of the immune system on iNSC persistence and treatment efficacy.

2.4. CONCLUSION

In this study, we show the impact FLOSEAL® has on iNSC gene expression, persistence, and efficacy. While encapsulating iNSCs in FLOSEAL® produced the longest persistence to date, only some mice showed a corresponding increase in survival. Moreover, culturing iNSCs in FLOSEAL® most notably impacted proliferation, anti-apoptosis, and migration gene expression. This data serves as the framework for future scaffold optimization studies as iNSCs advance towards human clinical trials.

2.5. MATERIALS & METHODS

2.5.1. CELL LINES

U87 tumor cells were obtained from the American Type Culture Collection. U87 cells were cultured in Dulbecco's Modified Eagle Medium (Gibco) containing 10% fetal bovine serum and 1% penicillin/streptomycin (henceforth referred to as standard culture media). GBM8 tumor cells were a gift from H. Wakimoto (Massachusetts General Hospital). GBM8 cells were cultured using 500 mL filtered Neurobasal Medium (Gibco) containing 3 mM/L L-glutamine, 10 mL B27 supplement (Gemini), 2.5 mL N2 supplement (Gemini), 2 μg/mL heparin, 2.5×10^4 U/mL penicillin, 2.5×10^4 μg/mL streptomycin, 62.5 μg/mL amphotericin B, 20 ng/mL fibroblast growth factor, 20 ng/mL epidermal growth factor. Normal human fibroblasts (NHF1s) were obtained from W. Kauffman (University of North Carolina School of Medicine) and were hTERT-immortalized.

2.5.2. TRANSDUCTION

Transduction was performed to produce cells expressing optical reporters and therapeutic proteins. Fibroblasts were transduced by incubating the cells with 8 μg/mL polybrene and the lentiviral cocktail for 24 hrs at 37ºC/5% CO_2. The next day, the virus-containing media was aspirated and replaced with fresh standard culture media. 'Non-therapeutic cells' denotes NHF1 cells transduced with lentiviruses encoding *eGFP-Fluc*, *SOX2*, and *rtTA.* The *eGFP-Fluc* plasmid construct contained a puromycin-resistance gene to allow for selection of cells. 'Therapeutic cells' denotes NHF1 cells transduced with *eGFP-TRAIL*, *Fluc*, *SOX2*, and *rtTA* lentiviruses. GBM8 and U87 cells were transduced using lentiviral *mCh* and *Fluc*. All lentiviruses were purchased from the Duke Viral Vector Core.

2.5.3. iNSC PRODUCTION

To manufacture therapeutic and non-therapeutic iNSCs, 2×10^6 transduced NHF1s were plated in a tissue culture-treated T-175 flask using standard culture media. Twenty-four hours later,

the media was changed to STEMdiff Neural Induction Medium (Stem Cell Technologies 05835) supplemented with 2 μg/mL of doxycycline (henceforth referred to as transdifferentiation media). Transdifferentiation media was replaced every other day for five days. On the fifth day, cells were harvested using Accutase (STEMCELL Technologies 07922) and passed through a 100 μm filter. Harvested iNSCs were immediately used or kept on ice for no more than 4 hrs.

2.5.4. ENCAPSULATING iNSCs IN SCAFFOLDS

To encapsulate iNSCs (Baxter ADS201845), the cells were suspended in 500 μL thrombin from the FLOSEAL® kit and loaded into one of the Luer lock syringes. The second Luer lock syringe was loaded with 86 mg of the gelatin powder. The ratio of thrombin to gelatin powder was determined by taking the total volume and weight of the kit components and scaling down to numbers appropriate for murine studies. The two syringes were then connected head-to-head and passaged back-and-forth twenty times to mix the contents. The contents were left in a single syringe and either used immediately or kept on ice, up to 4 hrs. This protocol produces approximately 600 μL of cell-scaffold mixture. For *in vitro* studies, FLOSEAL® scaffolds were polymerized with 30 μL of fibrinogen from TISSEEL® kits (Baxter 1501653SP). To encapsulate iNSCs in TISSEEL®, 8 μL of fibrinogen was plated into each well of a 6-well plate. Next, iNSCs were suspended in 8 μL thrombin and pipetted directly on to the fibrinogen. TISSEEL® scaffolds were allowed to polymerize for approximately 15 min at room temperature and then kept on ice, up to 4 hrs. Lastly, to seed cells onto Gelfoam®, a 3 mm diameter hole punch was used to create uniform scaffold discs. Discs were placed into a 96-well plate and 2.5 μL of the iNSC suspension was pipetted directly onto each side of the disc. iNSCs were allowed to adhere for 1 hr at 37°C/5% CO_2, and were then kept on ice until use, up to 4 hrs.

2.5.5. SCANNING ELECTRON MICROSCOPY (SEM)

A conjectural count of 6×10^6 therapeutic iNSCs were encapsulated in FLOSEAL® as described above. The resulting six scaffolds were polymerized and incubated at 37°C/5% CO_2 for 30 min. Following incubation, scaffolds were submerged in 10% formalin for 30 min. Samples were dehydrated using a graded ethanol series of 50%, 75%, 90%, and 100% ethanol. Next, samples were dried using a critical point drier (Tousimis Autosamdi-931), placed on aluminum stubs, and sputter coated with 6 nm of gold-palladium (Cressington Sputter Coater 108auto). The seeded scaffolds were imaged using a FEI Helios 600 Nanolab Dual Beam System microscope with a 2kV accelerating voltage.

2.5.6. IN VITRO SCAFFOLD SEEDING EFFICIENCY

Non-therapeutic NHF1s were harvested using 0.05% trypsin and counted (ThermoFisher Countess II). Next, cells were resuspended to obtain 5×10^4, 1×10^5, 5×10^5, 1×10^6, 2×10^6, and 3×10^6 cells per tube, and genomic DNA was extracted from each tube per manufacturer's protocol (ThermoFisher K182002). DNA was quantified using a Qubit Fluorometric Quantification system (ThermoFisher). Each cell concentration was quantified in triplicate to create a standard curve. To quantify seeding efficiency, non-therapeutic iNSCs were encapsulated in FLOSEAL® as described above, but not polymerized with fibrinogen. The scaffold mixture was divided into 6 tubes and DNA was isolated. This experiment was done in triplicate to produce a total of 18 samples.

2.5.7. qRT-PCR

Therapeutic iNSCs were produced as described above and encapsulated in FLOSEAL® at a conjectural density of 2×10^6 cells/scaffold. Seeded scaffolds were plated on 0.4 μm hanging cell culture inserts (Millipore MCHT06H48) and polymerized as detailed above. To each well, 2 mL transdifferentiation media was added, and samples were incubated at 37°C/5% CO_2;

transdifferentiation media was replaced every other day. Five or six scaffold samples were collected and pooled on days 3, 7, and 14. Immortalized NHF1s transduced with *SOX2, rtTA, and GFP-TRAIL* and therapeutic iNSCs not encapsulated in FLOSEAL® (day 0) served as controls. Total RNA was extracted per manufacturer's protocol (ThermoFisher 12183020), immediately converted to cDNA (Invitrogen 11754050), and stored at -80°C until use. qRT-PCR was performed using the Applied Biosystems QuantStudio 3 Real-Time PCR System with TaqMan reagents (ThermoFisher A44360) and custom primer-probe pairs targeting 30 genes. The thermal protocol used is as follows: UNG incubation at 50°C for 2 min and 1 cycle, enzyme activation at 95°C for 20 sec and 1 cycle, denaturing at 95°C for 1 second and 40 cycles, and annealing/extension at 60°C for 20 sec and 40 cycles. Relative fold gene expression was calculated using the $\Delta\Delta C_T$ method using D0 iNSCs as the biologic control and 18s rRNA as the endogenous control. Supplemental Table 1 lists genes and corresponding assay IDs.

Table 2.1. qRT-PCR Assay Identification Numbers.

Category	Gene	Assay ID
NSC	PAX6	Hs01088114_m1
	SOX9	Hs00165814_m1
	C-MYC	Hs00153408_m1
	NESTIN	Hs04187831_g1
Pluripotency	NANOG	Hs02387400_g1
	OCT4	Hs04260367_gH
	PODXL2	Hs00210532_m1
Differentiation	GFAP	Hs00909233_m1
	TUBB3	Hs00801390_s1
	VMAC	Hs00418522_m1
Migration	PIK3CD	Hs00192399_m1
	CSPG4	Hs00361541_g1
	CD44	Hs01075864_m1
	GDNF	Hs01931883_s1
	SOX2	Hs01053049_s1
	FGFR2	Hs01552918_m1
	P2RX7	Hs00175721_m1
	SDC1	Hs04966523_m1
	TNC	Hs01115665_m1
	STC1	Hs00174970_m1
	IL-6R	Hs01075664_m1
	HIF-1α	Hs00153153_m1
	VCAM-1	Hs01003372_m1
	PLAUR	Hs00958880_m1
	FLT1	Hs01052961_m1
	CXCR4	Hs00607978_s1
Proliferation	KI67	Hs04260396_g1
	IL-1R	Hs00991010_m1
Other	TRAIL	APH6DPA
	HSPA5	Hs00607129_gH

2.5.8. IN VIVO iNSC PERSISTENCE

All animal studies were approved by the Animal Care and Use Committee at the University of North Carolina at Chapel Hill. 6–8-week-old female, athymic nude mice (Animal Studies Core, University of North Carolina-Chapel Hill) were anesthetized using 2.5% inhaled isoflurane and placed into a stereotaxic frame. The surgical site was prepared using 70% isopropyl alcohol and betadine. An incision was made in the skin on the head of the mouse to expose the skull. Next, using a microdrill, a craniotomy was performed on the parietal skull plate. Cold saline and

Surgicel® was used to control bleeding. Surgicel® was removed prior to incision closure with Vetbond (3M 1469SB). Post-operative pain was managed with 5 mg/kg of subcutaneous meloxicam 24 hrs after surgery. Three days following the craniotomy, the mice were anesthetized and prepared for cell implantation. The previous wound was reopened, and the exposed dura mater was removed using an 18 G needle. Using a vacuum pump, a mock resection cavity was created. Next, after bleeding subsided, a conjectural count of 1×10^6 non-therapeutic iNSCs were implanted, either in 4 μL of a 1X PBS suspension or encapsulated in a FLOSEAL®, TISSEEL®, or Gelfoam® scaffold. Lastly, the wound was closed with Vetbond, and post-operative pain was managed with 5 mg/kg of subcutaneous meloxicam 24 hrs after surgery. iNSC persistence was quantified via serial BLI imaging (IVIS Kinetic, Perkin Elmer) using 150 mg/kg D-luciferin (PerkinElmer 122799) in 1X PBS injected intraperitoneally.

2.5.9. HISTOLOGY

Mice were anesthetized using 5% inhaled isoflurane. Cardiac perfusion was performed by injecting 5 mL 1X PBS followed by 5 mL 10% formalin into the left ventricle of the heart. Following cervical dislocation, brains were harvested and immediately fixed by transferring into a vial containing 10% formalin. Samples were fixed overnight at 4°C and then transferred to a vial containing 30% sucrose in 1X PBS. Samples were kept at 4°C until the tissue sunk. Next, brains were prepared for cryosectioning by placing the tissue in a cryomold (Tissue-Tek Cryomold, Sakura), covering with optimal cutting temperature compound (OCT), and freezing at -80°C. Tissue sections were cut 40 μm thick onto microscope slides. Then, OCT was washed away by incubating the sample in 1X PBS at room temperature for 5 min. To visualize cells, the sample was stained with DAPI (Invitrogen) and mounted on ProLong™ Gold Antifade Mountant (Invitrogen).

2.5.10. IN VIVO iNSC EFFICACY

Mice were anesthetized using 2.5% inhaled isoflurane and placed into a stereotaxic frame. The surgical site was prepared using 70% isopropyl alcohol and betadine. An incision was made in the skin on the head of the mouse to expose the skull. Next, using a microdrill, a craniotomy was performed on the parietal skull plate. Cold saline and Surgicel® were used to control bleeding. Surgicel® was removed, and the wound was closed with Vetbond (3M 1469SB). Three days after the craniotomy, mice were again anesthetized and prepared for surgery. The wound was reopened, and using a stereotaxic auto-injector, 1×10^5 U87-mCh-Fluc cells or 3×10^5 GBM8-mCh-Fluc cells suspended in 1X PBS were infused into the brain parenchyma at a rate of 1 μL/min, avoiding the lateral ventricles. Cells were given 5 min to settle before slowly removing the syringe. The wound was closed with Vetbond. Seven days after implanting the U87 tumors and 3 days after implanting the GBM8 tumors, mice were anesthetized and prepared for surgery. The wound was reopened, and the tumors were resected using fluorescence guidance and a vacuum pump. Once bleeding subsided, therapeutic iNSCs were implanted in a 1X PBS suspension or encapsulated in FLOSEAL®. For the GBM8 efficacy study where two doses of iNSCs were tested, 'FLOSEAL® high' TRAIL denotes mice that received 1.5×10^6 therapeutic iNSCs, and 'FLOSEAL® low TRAIL' denotes mice that received 6×10^5 therapeutic iNSCs conjecturally. All other groups received 1×10^6 therapeutic or non-therapeutic iNSCs, again noting conjecturally for the 'FLOSEAL® Control iNSC' group. In the U87 efficacy study, FLOSEAL® TRAIL denotes mice that received 1.5×10^6 therapeutic iNSCs conjecturally, and all remaining groups received 1×10^6 therapeutic or non-therapeutic iNSCs again noting conjecturally for the 'FLOSEAL® Control iNSC' group. Post-operative pain was managed with 5 mg/kg of subcutaneous meloxicam 24 hrs after surgery. iNSC Tumor volume was monitored over time via BLI (AMI HTX, Spectral

Instruments Imaging). Animals were euthanized when more than 20% of their original body weight was lost or when the animal displayed physical symptoms of pain-based dehydration, hunched position, tremors, and cold body temperature.

2.5.11. STATISTICAL ANALYSIS

Replicate number is defined by n in figure legends. All data presented as mean ± standard deviation unless otherwise stated. Seeding efficiency data analyzed via one-way ANOVA with Šidák's multiple comparisons test. iNSC persistence data analyzed via one-way ANOVA mixed effects analysis with Šidák's multiple comparisons test. Survival curves analyzed via log-rank (Mantel-Cox) test. In all graphs, * indicates $P<0.05$, ** indicates $P<0.01$, *** indicates $P<0.001$, and **** indicates $P<0.0001$. Statistical analyses were conducted using Prism GraphPad.

CHAPTER 3: PERSONALIZED INDUCED NEURAL STEM CELL THERAPY: GENERATION, TRANSPLANT, AND SAFETY IN A LARGE ANIMAL MODEL[1]

3.1. INTRODUCTION

The notoriously hard-to-treat brain tumor glioblastoma (GBM) consists of highly infiltrative cells. Standard treatment for patients with GBM consists of maximal tumor surgical resection followed by chemoradiotherapy. However, obtaining clean tumor margins is difficult, and residual tumor cells invade normal brain tissue, creating distant tumor foci.[137] Curtailing tumor recurrence with systemic therapies has seen limited success as the blood brain barrier (BBB) tightly regulates the passage of molecules from systemic circulation to the brain parenchyma, which prevents many chemotherapies from reaching infiltrative GBM cells.[138] Treatment advances for GBM must combat tumor recurrence by targeting the infiltrative cells that remain after standard therapy.

Induced neural stem cells (iNSCs) generated by the direct transdifferentiation of fibroblasts from a patient's own skin have recently shown promise as drug carriers for GBM due to their innate tumor tropism and low immunogenicity.[69] These tumor-seeking cells are genetically engineered to express cytotoxic proteins as they migrate towards invasive cancer cells. Early testing of iNSC therapy in pre-clinical models have demonstrated the effectiveness of iNSCs generated from human donors against human xenografts of GBM in athymic nude mice.[68,69,104] Although the athymic mouse model recapitulates many aspects of human tumor

[1]This chapter previously appeared as an article in the journal *Bioengineering & Translational Medicine*. The original citation is as follows: Bomba, H.N., *et al*. Personalized Induced Neural Stem Cell Therapy: Generation, Transplant, and Safety in a Large Animal Model. *Bioeng Transl Med*. (2020).

resection surgery, it is understandably limited in its ability to test iNSC doses on par with what would be administered to a human patient as well as its ability to elucidate any potential adaptive immune reactions. Additionally, a small animal model cannot accurately mimic the size of the surgical cavity or fluid volumes that iNSCs may be delivered into during initial human patient testing. A large animal model is needed to bridge the gap between mouse models and a first-in-human Phase I clinical trial.

Canine models can be used to bridge this translational gap, as gliomas occur spontaneously in canines with phenotypes and genetic mutations similar to humans.[47,139] While this study focused on testing the safety and toxicity of iNSCs in healthy, non-tumor-bearing canines, this was an important consideration when selecting an animal model that would be compatible with future efficacy studies. Despite the potential of this large-scale model, the generation of iNSCs from canine skin has not yet been reported. Additionally, the exploration of the delivery, dosing, and safety of autologous or allogeneic tumor-homing cell therapies has primarily focused on the murine model and is extremely limited in large animal models.[63,140,141] As such, we sought to demonstrate the feasibility of manufacturing, as well as the safety and toxicity of autologous therapeutic iNSCs using healthy canine patients. The iNSCs used in this study carry two therapeutic agents. The first therapeutic agent is TNFα-related apoptosis inducing ligand (TRAIL), a constitutively expressed protein that is continuously secreted into the extracellular space. TRAIL diffuses to nearby cells but initiates caspase-mediated apoptosis by engaging death receptors upregulated on cancer cells.[142] Importantly, TRAIL has been well-tolerated and has shown negligible off-target toxicities in normal cells in both pre-clinical and clinical studies.[143–146] The second constitutively expressed protein is the enzyme thymidine kinase (TK). TK remains inactive until administration of its non-therapeutic prodrug substrate valganciclovir (VGCV). VGCV is

first hydrolyzed into ganciclovir (GCV) in the liver and intestine, and subsequently, TK expressed by iNSCs phosphorylates circulating GCV into cytotoxic ganciclovir triphosphate (GCV-TP). Finally, GCV-TP inhibits DNA polymerase, consequently killing both the iNSC and nearby tumor cells via the bystander effect.[147,148] TK-VGCV therapy exhibits limited toxicity on normal brain cells due to their quiescent state.[149–151]

Using our early-stage studies in murine models as a guide, we demonstrate the production, safety and toxicity of autologous therapeutic iNSCs transdifferentiated from canine skin for the first time. Healthy, purpose-bred canines were successfully administered two dose levels of autologous iNSCs using two clinically relevant delivery methods: intracerebroventricular (ICV) infusion and scaffold encapsulation.[152,153] We further demonstrate the safety and minimal toxicity signals in the canine model using MRI, blood, urine, cerebrospinal fluid (CSF), neurological assessment, and histopathology. These promising results pave the way for future efficacy studies in a spontaneous canine glioma model as well as human clinical trials.

3.2. RESULTS

3.2.1. GENERATION OF CANINE iNSCs: ISOLATION, EXPANSION, & CONVERSION

Previously, we have shown the ability to convert mouse and human fibroblasts into tumor-homing iNSCs.[69] Using these studies as a guide, we first explored the feasibility of generating personalized canine iNSCs (Fig. 3.1A). First, full thickness (epidermis and dermis) skin biopsies were collected from donor canines. Once the animals were anesthetized, a skin biopsy was isolated from the base of the neck and placed into a tube containing collection media (Fig. 3.1B-C). To isolate the fibroblasts, skin biopsies were manually diced into approximately 6 mm pieces (Fig. 3.1D) and placed in digestion media containing a low concentration of collagenase, thus enabling long dissociation conditions without negative impacts on cell viability.[154,155] Following

dissociation, the tissue pieces were seeded in culture plates containing growth media, and fibroblasts were allowed to grow for 72 hrs. Once fibroblasts had expanded, the cells were trypsinized, filtered to removed unwanted solid tissue, and the remaining fibroblasts were allowed to proliferate rapidly. As shown in Fig. 3.1E, we observed robust outgrowth of fibroblasts from all biopsies. While fibroblasts initially proliferated reproducibly after each passage, cell senescence was observed as early as passage 12 for some fibroblast lines (data not shown). This timeline dictated the fibroblast transduction and transdifferentiation processes. As we have shown previously, we used the SOX2 transcription factor to and transdifferentiation media to convert fibroblasts into tumor-homing iNSCs.[69] To explore the potential of converting canine fibroblasts into canine iNSCs, we transduced the canine cells with lentiviral vectors encoding reverse tetracycline-controlled transactivator (rtTA) and SOX2, as well as the therapeutic and optical reporters mCherry-thymidine kinase (mCh-TK), and enhanced green fluorescent protein (eGFP) fused to TRAIL. Following transduction and five days of transdifferentiation with culture in the presence of doxycycline, >85% of cells expressed TRAIL and >95% of cells expressed TK as demonstrated by eGFP and mCh fluorescence, respectively (Fig. 3.1F). Additionally, immunofluorescence staining showed nearly all cells expressed transgenic SOX2, suggesting efficient transduction and conversion to the iNSC phenotype (Fig. 3.1G). In total, three fibroblast cell lines (biological replicates) were established and labeled iNSC-1, -2, and -3, respectively.

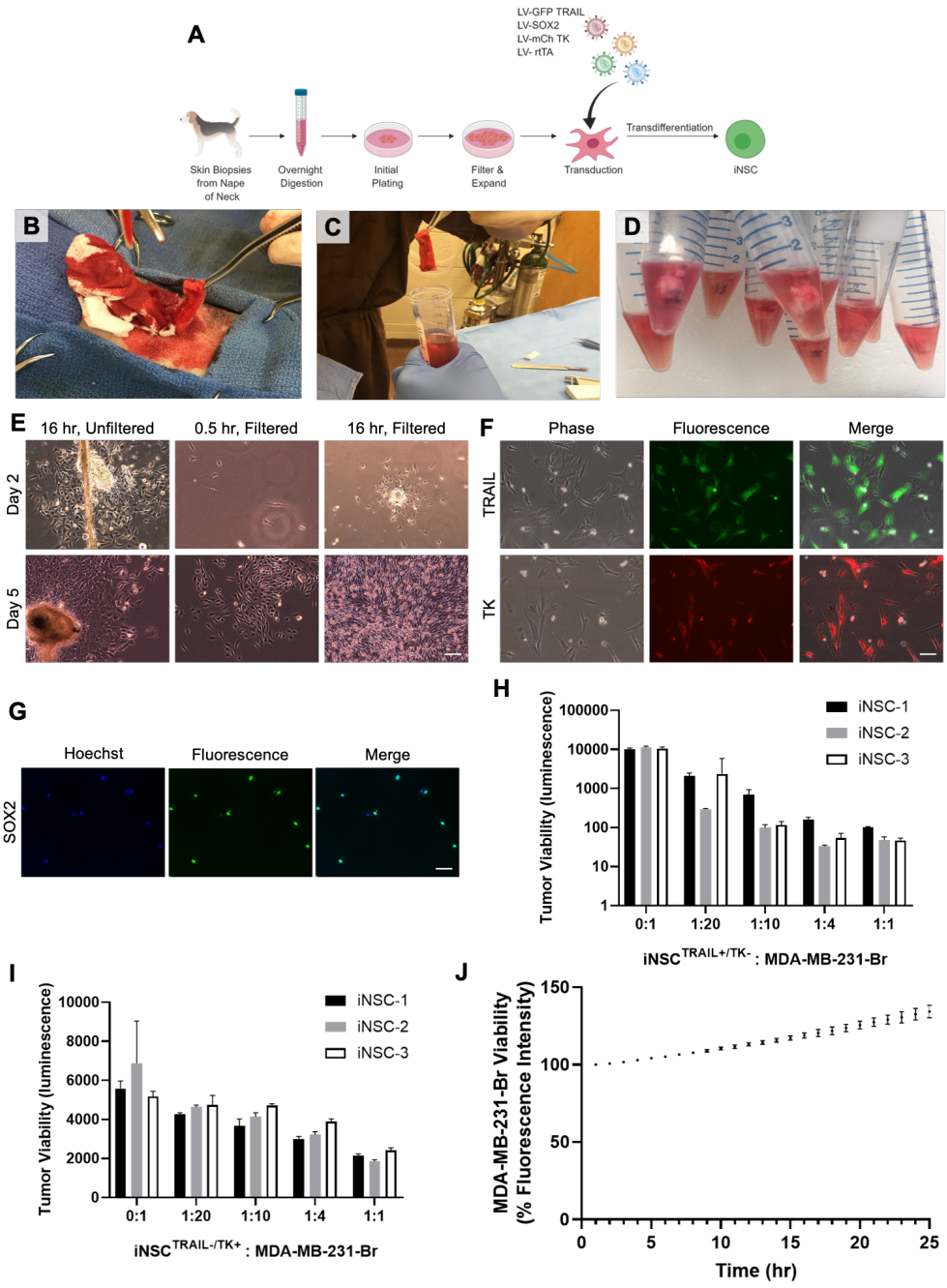

Figure 3.1. Murine Proof-of-Concept Studies. A) Schematic depicting fibroblast isolation, transduction, and transdifferentiation procedures. B) Skin biopsy harvest from cadaver canine. C-D) Skin samples in digestion media. E) Cultures of primary canine fibroblasts 16 hrs after plating and prior to filtering, 30 min after filtering, and 16 hrs after filtering. Scale bar 100 µm. F) Fluorescence imaging confirming TRAIL expression in fibroblasts. Scale bar 100 µm. G) Immunofluorescence imaging of transdifferentiated fibroblasts to confirm SOX2 expression. Scale bar 50 µm. H) Quantification of iNSCTRAIL+/TK- and MDA-MB-231-Br 42 hr coculture assay. I) Quantification of iNSCTRAIL-/TK+ and MDA-MB-231-Br 72 hr coculture assay. J) Quantification of iNSCTRAIL-/TK- and MDA-MB-231-Br 25 hr coculture assay. All data presented as mean ± standard deviation.

3.2.2. INVESTIGATING TUMORITROPIC MIGRATION & TUMOR KILLING OF CANINE iNSCs

After confirming transduction and transdifferentiation of canine fibroblasts to iNSCs, in vitro functional assays were conducted to test the migratory and tumor-killing capability of the new therapeutic cells. The metastatic breast cancer cell line, MDA-MB-231-Br (231-Br), which was isolated from brain metastases, was selected as the model tumor for in vitro assays because of its ease of growth and sensitivity to TRAIL. Tumor-homing migration is one of the most critical aspects of stem cell therapy for cancer. To investigate canine iNSC migration, we used real-time motion analysis and co-culture assay systems. Using a two-well migration insert, the directional migration of iNSCs$^{TRAIL-/TK-}$ towards 231-Br tumor cells was clearly observed while non-transdifferentiated fibroblasts moved in a Brownian manner in the 500 μm gap, which similar to our previously published data for mouse and human iNSCs (supp. movies 1-3). Next, a co-culture assay was used to evaluate the killing capacity of the canine iNSCs lines against 231-Br cells. The cytotoxicity of iNSC$^{TRAIL+/TK-}$ and iNSC$^{TRAIL-/TK+}$ were tested individually. To explore the efficacy of TRAIL monotherapy, we found that total tumor luminescence decreased as the ratio of iNSCs$^{TRAIL+/TK-}$ to 231-Br cells increased. A 1:20 ratio of iNSCs$^{TRAIL+/TK-}$ to 231-Br cells was sufficient to produce a 5-fold reduction in tumor viability compared to the 0:1 tumor-only controls. Promisingly, a 100-fold reduction in tumor viability was observed when iNSCs were cultured in a 1:1 ratio with 231-Br cells compared to 0:1 tumor-only controls following 42 hrs of co-culture (Fig. 3.1H). Moreover, time-lapse imaging showed 50% of the 231-Br cells were dead in less than 10 hrs, and nearly 100% of 231-Br cells are dead in less than 24 hrs (supp. movie 4). Next, exploring the efficacy of TK mono-therapy using iNSC$^{TRAIL-/TK+}$ cells, we found a nearly 2-fold reduction in tumor viability at 72 hrs in the 1:20 iNSC:tumor group compared to the 0:1 tumor-only control group for all samples (Fig. 3.1I). In the absence of TRAIL and VGCV, we showed

the iNSCs did not induce apoptosis and allowed the 231-Br cells to expand (Fig. 3.1J). Overall, these data suggest that canine iNSCs have the ability to seek out tumor cells and induce tumor apoptosis. Importantly, these results also showed similar migratory and killing potencies in all three canine iNSC lines, thus demonstrating the reproducibility of this technology.

3.2.3. DEVELOPING METHODS FOR MRI TRACKING OF CELLS

Tracking iNSCs in patients is highly beneficial, allowing insights into persistence and distribution. Although fluorescent- and bioluminescent-tracking is valuable in pre-clinical models, the use of these modalities in human patients is limited by light penetration and other challenges. To generate a method for tracking iNSCs that is compatible with canines and eventual human patients, we opted to label fibroblasts with superparamagnetic iron oxide nanoparticles (ferumoxytol) for MRI. Fibroblasts were used in lieu of iNSCs to expedite this experiment. Ferumoxytol is an FDA-approved iron replacement therapy and has recently been explored for its use as a cell-labeling agent.[156–158] Importantly, ferumoxytol has been shown to have no impact on cell viability or stemness, and the iron particles are not readily exocytosed, making it an ideal labeling agent for long-term tracking of iNSCs.[156,159] To investigate the potential of labeling fibroblasts for MRI tracking with this agent, the canine cells were transfected with ferumoxytol and assessed for particle uptake in vitro. As shown in Fig. 3.2A, Prussian blue staining of cultured fibroblasts showed homogeneous uptake of iron oxide particles in the fibroblasts. After confirming labeling in vitro, we next assessed imaging and tracking of the labeled cells in vivo. Unlabeled fibroblasts, ferumoxytol-labeled fibroblasts, and free ferumoxytol were injected into the brain parenchyma of mice. Changes in volumes were then tracked using MRI over three days (Fig. 3.2B). Analysis of images showed the cells and free ferumoxytol injection sites are clearly visible in all samples on the day of implant. The unlabeled and iron-labeled fibroblasts appear confined to a single location in the brain, whereas free ferumoxytol spreads from the injection site. By the

third day post-infusion, unlabeled and iron-labeled fibroblasts remain constrained at their initial injection site, but the free ferumoxytol particles continue to spread medially, caudally, and invade the contralateral hemisphere. To confirm imaging results, mice were sacrificed following MR imaging on day three, brains were harvested, and tissue sections were probed for the presence of iNSCs (Fig. 3.2C). Strong eGFP fluorescence was observed at the site of injection, and Prussian blue staining confirmed the colocalization of iNSCs with iron oxide particles. We believe these studies suggest that we have the ability to isolate and transduce primary canine fibroblasts, transdifferentiate fibroblasts to iNSCs, kill tumor cells using both TRAIL and TK/VGCV, and track iNSCs in mice using MRI. Taken together, these *in vitro* and murine *in vivo* studies laid the foundation for the canine scale-up model. Building on this knowledge, we designed a canine study to evaluate the safety and toxicity of autologous canine iNSCs at low and high doses using two delivery mechanisms anticipated to be used clinically.

3.2.4. STUDY DESIGN TO TEST DELIVERY & DOSING

In the clinical setting, patient skin biopsies will be collected and converted into iNSCs, which will then be delivered back into patients following surgical resection as part of clinical standard of care for GBM patients. Using our expertise in canine neurosurgery, we created a surgical resection cavity and explored the delivery of iNSCs into the brain using two methods: 1) intra-cavity seeding within a bio-compatible matrix, and 2) infusion into the CSF through a reservoir implanted in the lateral ventricle. Four healthy, male canines were randomized into one of two study arms: ICV injection or scaffold implantation. One canine in each cohort was to receive 1×10^6 autologous iNSCs/kg per dose, and the other canine was to receive 3×10^6 autologous iNSCs/kg per dose. Canines in the ICV cohort, referred to from here on as canine patient 01 and 02 (CP01 and CP02), received a total of three iNSC injections every four weeks, while canines in

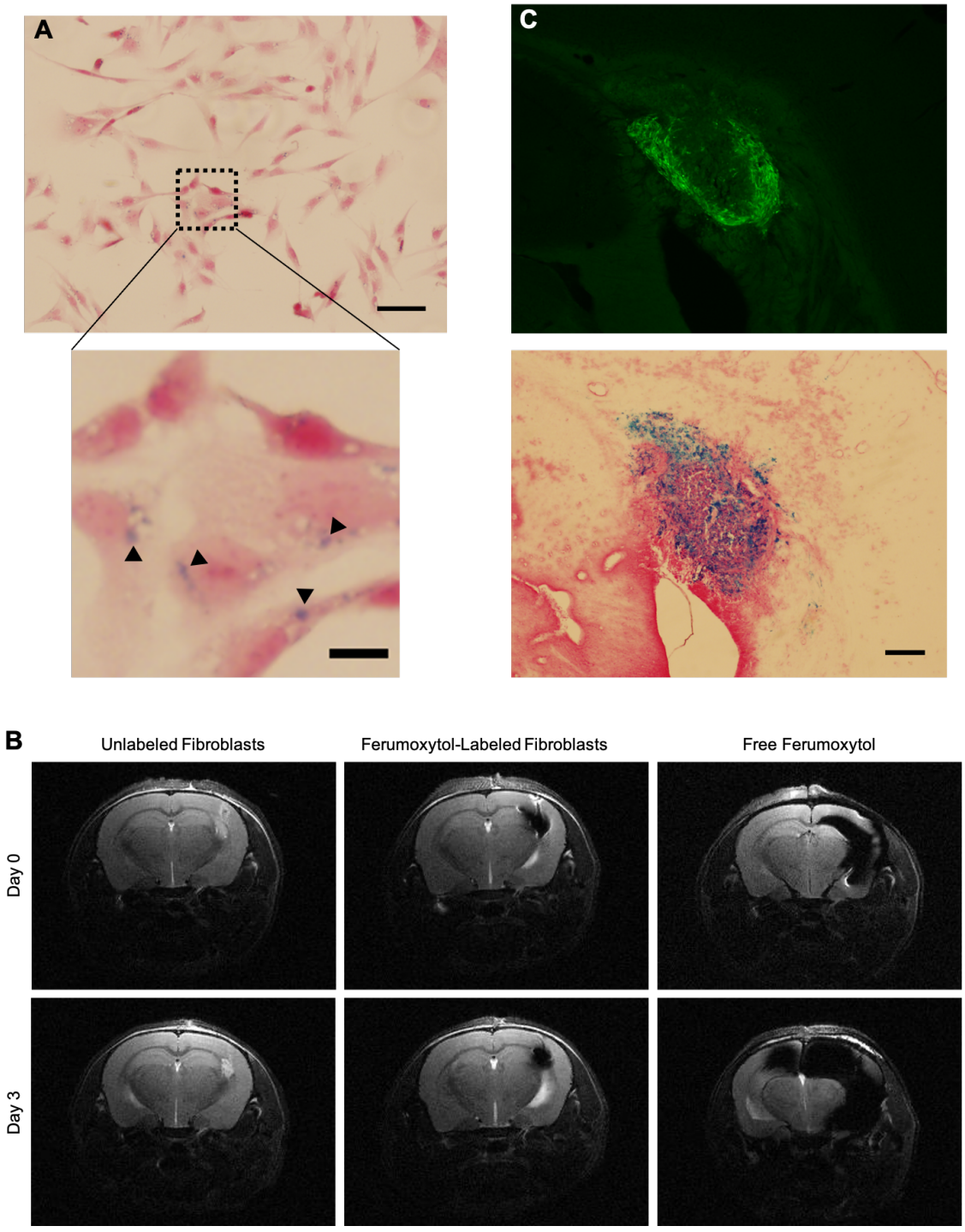

Figure 3.2. Detection of Fibroblasts via Magnetic Resonance Imaging. A) Prussian blue staining of ferumoxytol-labeled fibroblasts. Scale bar 50 μm. Magnified image scale bar, 10 μm. B) Comparison of MR images using unlabeled fibroblasts, ferumoxytol -labeled fibroblasts, and injection of ferumoxytol suspension over 3 days. C) Histological sections of mouse brain injected with ferumoxytol-labeled fibroblasts. Fluorescence (top) depicts fibroblasts, and Prussian blue stain (bottom) depicts ferumoxytol particles. Scale bar 200 μm.

the scaffold cohort, referred to from here on as canine patient 03 and 04 (CP03 and CP04), received a single scaffold implantation (Fig. 3.3A). Animal health and iNSC detection was monitored via routine physical and neurological examinations; blood, urine, and CSF screenings; and MRI. At specified time points, canines were assessed for toxicity. If no toxicity or adverse safety signals were observed, the animal was to continue with the study; however, if a toxicity or safety signal was observed, the second canine in the cohort was redirected to the other study arm (Fig. 3.3B-C).

3.2.5. MANUFACTURING & SCALE-UP OF CANINE iNSCs

We next worked on expanding the canine iNSCs manufacturing process. Upon delivery, canines underwent a physical examination to ensure suitability for the study. CP01, CP02, and CP04 weighed 15-20 kg at the time of biopsy. CP03 weighed slightly less at 12 kg. After confirming animal health, full-thickness skin biopsies were surgically excised and autologous iNSCs were manufactured for each patient. One of the biggest challenges in this study was scaling-up manufacturing procedures for a canine from a mouse model. As expected, interpatient variability was seen in fibroblast proliferation and transduction efficiency. This made it challenging to predict the iNSC yield after transduction and transdifferentiation. For CP01, we successfully generated the full 1×10^6 iNSCs/kg dose. CP01 received 15×10^6, 14×10^6, and 15×10^6 iNSCs at each dose, respectively. CP02 did not receive the target dose of 3×10^6 iNSCs/kg any of its three doses; CP02 was administered 20×10^6, 17×10^6, and 12×10^6 cells for the first, second, and third doses, respectively. The goal of 1×10^6 iNSC/kg was reached for CP03 and the canine was implanted with a scaffold containing 12×10^6 iNSCs total. CP04 did not reach the dose goal of 3×10^6 iNSCs/kg but was implanted with a scaffold containing 25×10^6 iNSCs total. Further optimization of these processes and incorporation of large-scale cell culture platforms (e.g. bioreactors) in the future would ameliorate manufacturing scale-up challenges.

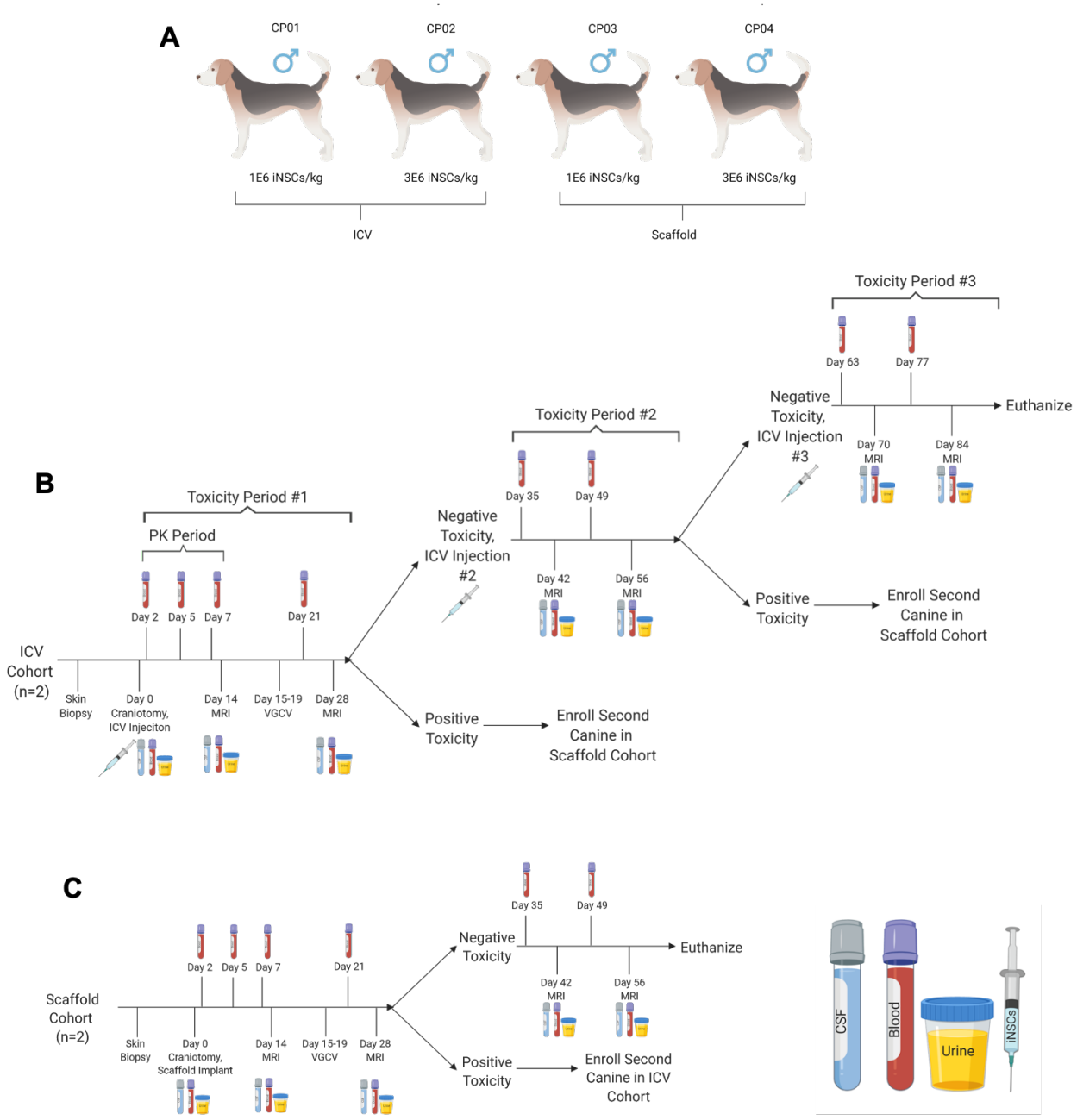

Figure 3.3. Canine Safety and Toxicity Study Design. A) ICV and scaffold treatment arm dosing. B) ICV study arm timeline. C) Scaffold treatment arm timeline.

3.2.6. AUTOLOGOUS TRANSPLANT OF CANINE iNSCs INTO THE BRAIN

Brain surgeries are notoriously complex procedures. We sought to closely mirror the surgery and subsequent cell implant in human patients in our canine model. As a first step, we used digital navigation to guide surgery. Canines were anesthetized and custom bite plates with fiducial markers were re-affixed to the canine's maxillary dental arcade (Fig. 3.4A). Due to the conformation of the canine teeth, it was challenging to fit the bite plates in the canines. This risked the accuracy of the surgical navigation. Next, the stereotaxic frame was placed around the head of the animal (Fig. 3.4B) and an incision was made to expose the skull (Fig. 3.4C). Using a high-speed drill, a craniotomy was performed to expose the cerebrum (fig. 4D). The BrainSight system was utilized for neuronavigation using previously obtained MRI scans (Fig. 3.4E-F). Under the guidance of this system, we confirmed key anatomic locations and aspiration was used to remove brain tissue to create a mock resection cavity (Fig. 3.4G). For canines in the scaffold cohort, the iNSC$^{TRAIL+/TK-}$ cells were encapsulated in a FLOSEAL® matrix and seeded into the resection cavity (Fig. 3.4H). For the ICV cohort, a separate burr hole was created and an ICV catheter was placed into the ipsilateral (right) lateral ventricle, leaving the reservoir within the skull burr hole below the temporalis muscle and skin (Fig. 3.4I). iNSC$^{TRAIL+/TK-}$ cells were then injected into the reservoir (Fig. 3.4J). Although the lateral ventricle was accessed and CSF obtained in both canines in the ICV cohort, the ICV catheter tip was not precisely placed within the ventricle in either canine due to bite plate inaccuracies and the small size of canine lateral ventricles. Following iNSC$^{TRAIL+/TK-}$ therapy administration, the incisions were closed with sutures and staples (Fig. 3.4K). Canines in the ICV cohort received two subsequent cell doses, given every four weeks. For additional doses, the canines were anesthetized, the skin was sterilized, and ultrasound was used to locate the ICV reservoir (Fig. 3.4L-M). The iNSC$^{TRAIL+/TK-}$ cells were administered using a syringe and needle through the skin and muscle without the need to re-open the surgical incision

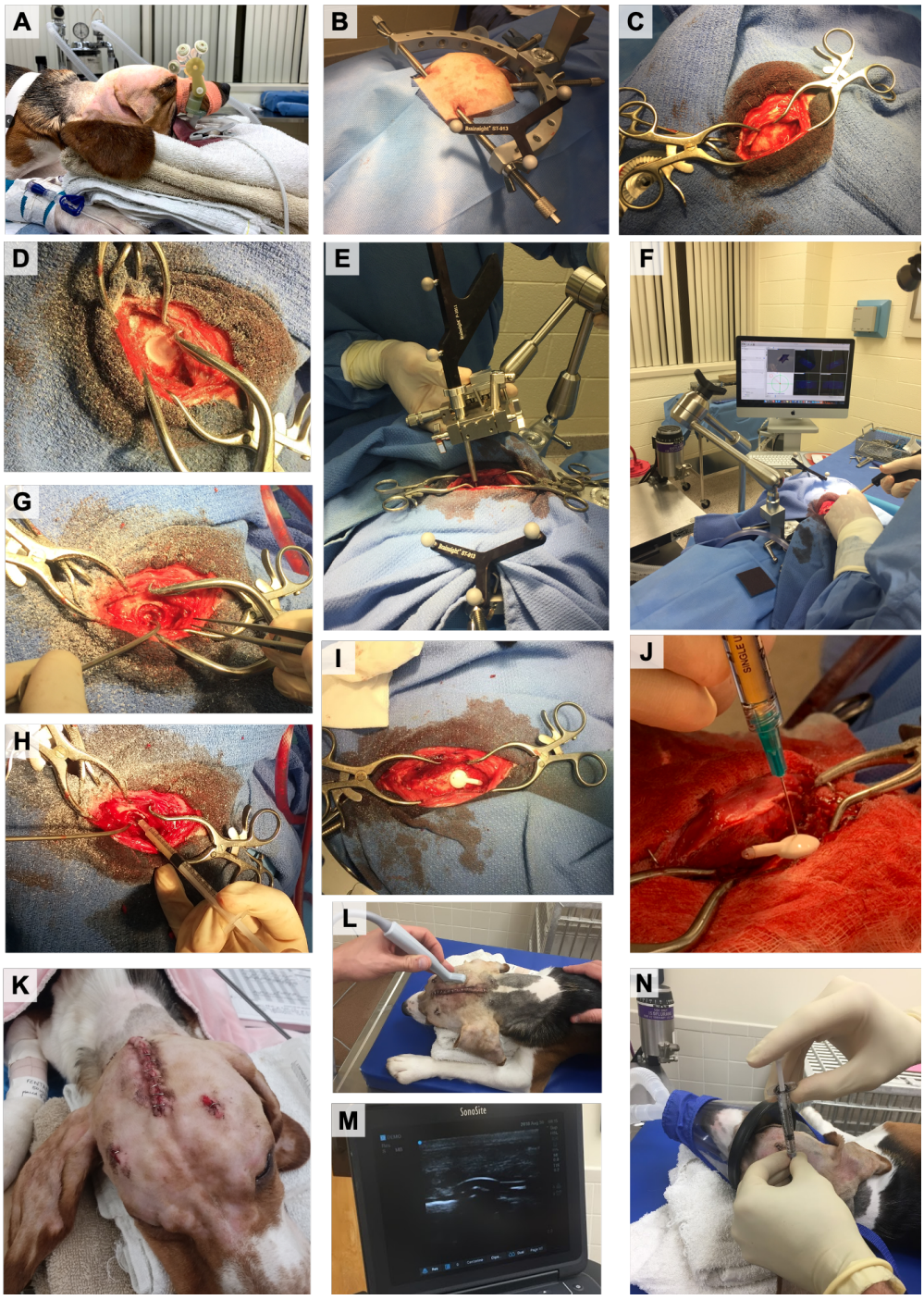

Figure 3.4. Canine Intra-operative Procedure. A) Application of bite plate and attached fiducial markers onto upper dental arcade. B) Fixation of skull in stereotaxic frame and attachment of BrainSight navigation system. C) Exposing the skull. D) Craniotomy. E-F) Using the BrainSight system to locate lateral ventricles. G) Resection cavity. H) Injection of iNSC$^{TRAIL+/TK-}$ cells suspended in FLOSEAL®. I) Implantation of ICV reservoir. J) Close-up of injection of iNSC$^{TRAIL+/TK-}$ cells into ICV reservoir. K) Wound closure. L) Use of ultrasound to locate ICV reservoir. M) Sonogram depicting curvature of ICV reservoir. N) Injection of iNSC$^{TRAIL+/TK-}$ cells into ICV reservoir.

(Fig. 3.4N). Throughout the surgical procedures, special considerations had to be made to maintain sterility while handing off the syringe containing the iNSC$^{TRAIL+/TK-}$ cells. Importantly, no acute injection site reactions were observed in any of the canines following iNSC$^{TRAIL+/TK-}$ administration. VGCV was administered orally to each canine patient 14 days after receiving an iNSC dose for a total of 5 days.

3.2.7. ASSESSMENT OF COGNITIVE FUNCTION

All animals underwent neurological examination after recovering from the intracranial surgery. Neurological deficits were limited to visual defects in the eye contralateral to the surgical site in CP01, CP03, and CP04 and transient postural reaction deficits in the contralateral limbs of all canines. These post-operative changes were consistent with the cerebral resection and were not considered a safety signal of the iNSCs.

3.2.8. TRACKING PERSISTENCE OF AUTOLOGOUS iNSCs

We anticipated the autologous nature of iNSCs would allow the cells to avoid immune rejection, where the longer persistence could offer advantages in efficacy. However, the persistence of personalized iNSC carriers in autologous, immune competent models is unknown. Similar to the proof-of-concept murine studies, MRI was used to track iNSC persistence and assess ICV reservoir placement. We first focused on analysis of canines in the ICV group. Interestingly, MRI images from this group suggested that the ICV catheter tip extended beyond the lateral ventricle in the case of CP01 and is positioned slightly dorsomedially to the lateral ventricle in the case of CP02. Despite the partially missed placement, analysis of the MRI images (Fig. 3.5A) showed a hypointense region that remained present through 84 days with no marked reduction in the hypointense signal over time, suggesting iNSCs may persist for several months post-infusion. We next turned our focus to iNSCs delivered via intracavity scaffolds. As shown in Fig. 3.5B, the

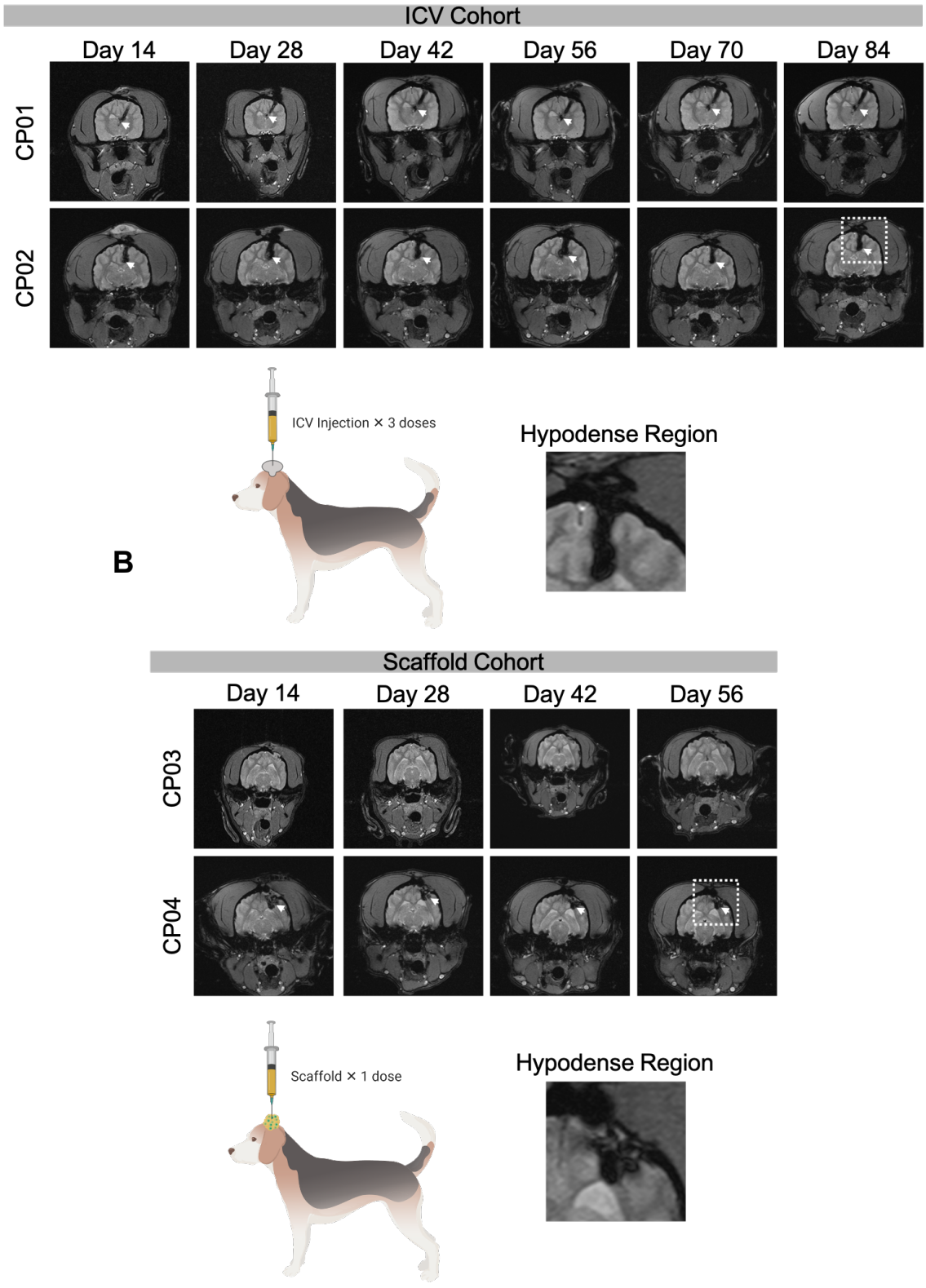

Figure 3.5. Canine MR Imaging. Transverse T2* MRI of canine patients in the A) ICV cohort and B) scaffold cohort. Hypodense regions (white arrows) indicate presence of blood and/or ferumoxytol. Close up of hypodense region outline by white box.

hypointense regions were less evident for CP03 compared to CP04, likely due to the depth of the resection cavity and/or iNSC dose. However, a hypointense region was clearly visible for CP04 within 14 days post-implant that remained stable and detectable through 56 days post-transplant. While T2* MRI was used to track the presence of iNSCs, it also denotes the presence of blood as it detects the presence of iron in hemoglobin. However, it is expected that blood and its degradation products would resorb over time and a reduction in the hypointense signal would be observed.[160] As the hypointense region persisted nearly 60 days post-transplant, and without dramatic changes in volume, we believe this suggesting that the hypointense signal is indicative of iNSCs rather than hemoglobin.

3.2.9. ASSESSING THE SAFETY OF PERSONALIZED iNSC THERAPY

Demonstrating iNSCs are safe is one of the most important parameters to test as iNSCs move towards human patients. Although human iNSCs have previously been shown to be safe, these studies were limited as they were performed in immune-depleted mice. The autologous transplant into fully immune-competent canines offers the potential to more accurately assess iNSC safety in a model mirroring personalized human iNSC therapy. To investigate the safety of iNSCs, canine health was assessed using complete blood count, blood chemistry, urine, and CSF (Fig. 3.6). As anticipated, elevations in white blood cells (WBCs), segmented neutrophils, aspartate aminotransferase (AST), and alanine aminotransferase (ALT) were noted immediately following surgery. These elevated levels were attributed to the post-surgical immune response and muscle manipulation during surgery. Interestingly, all canines experienced cyclic neutropenia throughout the study. The observation was first noted in CP01 and CP03 and correlated to MRI days. To ensure the effects were not caused by medications and anesthesia (including IV fluid therapy), peripheral blood was drawn and analyzed in three ways for CP03 on day 70: (1) prior to any medications or handling, (2) during IV catheter placement after premedication with

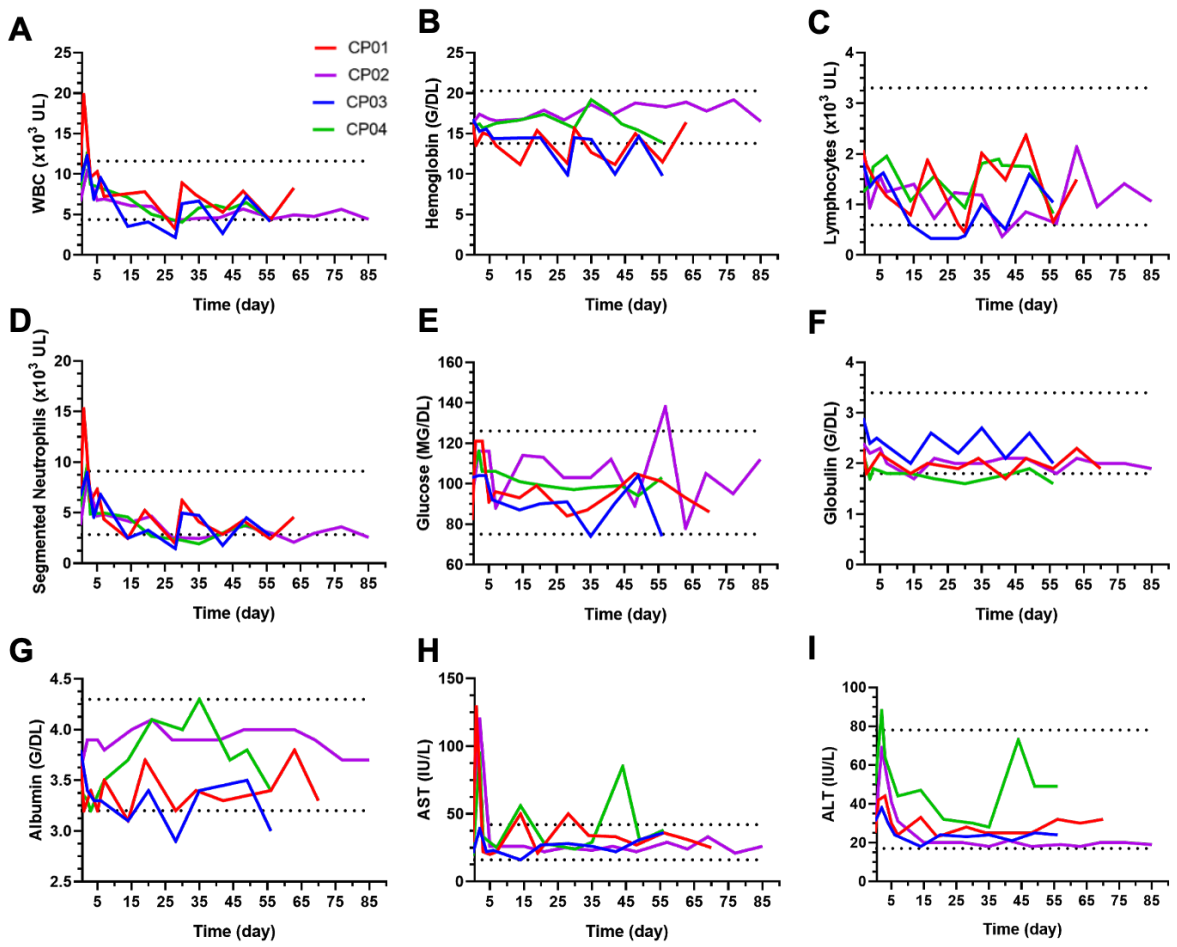

Figure 3.6. Canine Fluid Analysis. Select complete blood count and blood chemistry findings, including: A) White blood cell, B) hemoglobin, C) lymphocyte, D) segmented neutrophil, E) glucose, F) globulin, G) albumin, H) AST, and I) ALT findings. Dotted lines denote normal reference ranges for canines.

hydromorphone and midazolam but before anesthesia with propofol and isoflurane, and (3) after receiving all anesthetics and medications and after MRI. All blood draws indicated neutropenia in CP03. For CP02 and CP04, blood was drawn after administration of hydromorphone and midazolam but prior to propofol, isoflurane, and MRI. There was some evidence of a dilutional effects of the fluid therapy on blood cell counts. However, surprisingly neutropenia was observed on both MRI and non-MRI days, unlike in CP01 and CP03. There was also some evidence to suggest that VGCV can cause neutropenia. However, we cannot rule-out iNSC-induced

neutropenia.[161] Importantly, urine and CSF findings were unremarkable (data not shown). We also assessed all major organs for any signs of abnormal pathology following necropsy (Fig. 3.7). As anticipated, there were some notable findings near the ICV reservoir implantation site and the scaffold implantation site. These findings included: mild to moderate chronic inflammation, mild fibrosis, gliosis, and axon degeneration. Fibrous thickening and chronic inflammation were observed in the meninges in the region of the resection cavities of CP01 and CP02.

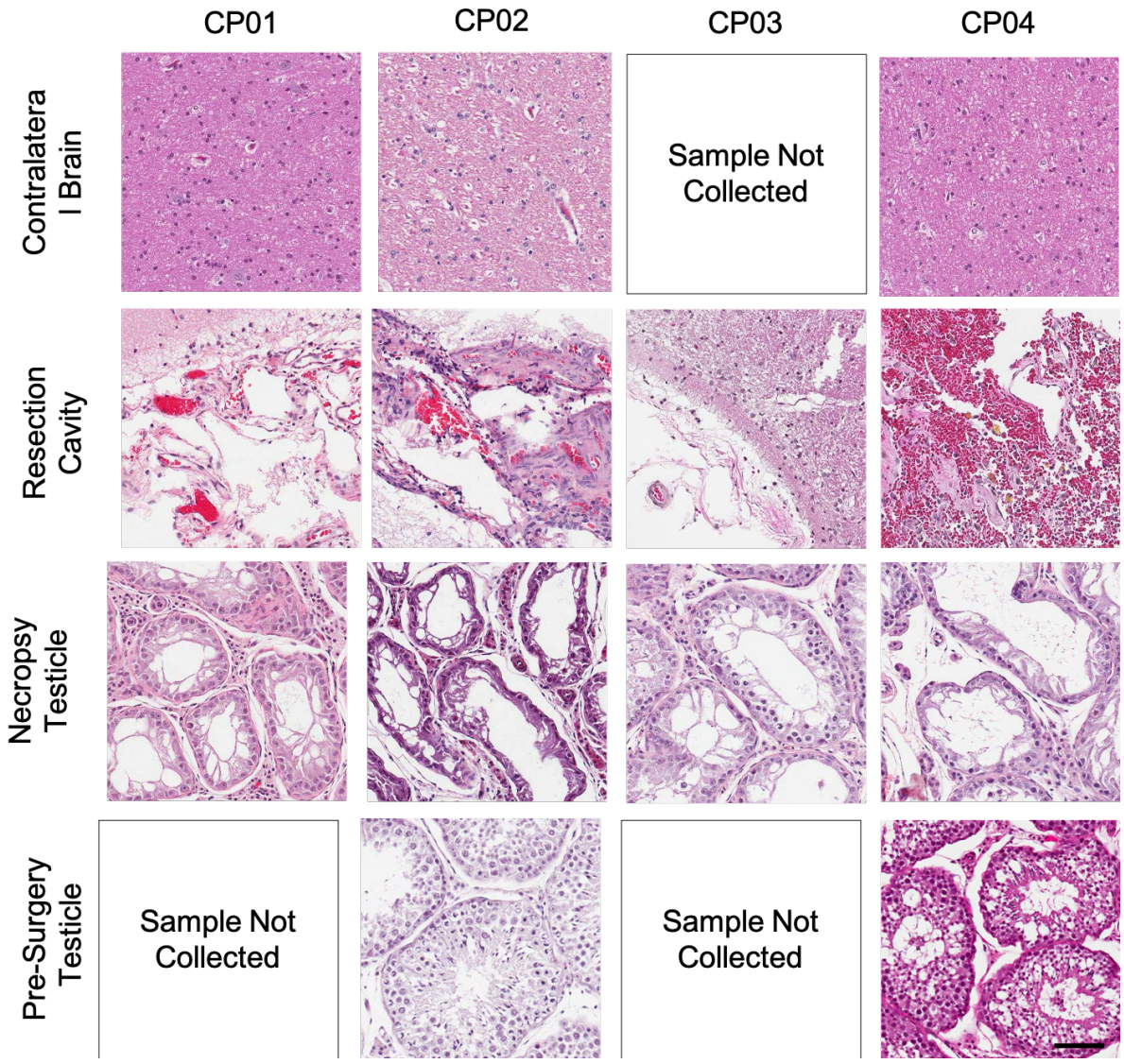

Figure 3.7. Canine Histology. Hematoxylin and eosin staining contralateral brain, resection cavity, testicular tissue at necropsy, and testicular tissue collected pre-surgery. Scale bar, 100 µm.

No abnormalities were identified in the contralateral brain in all canines. However, histologic changes in the brain and meninges near the resection cavities in the current study were attributed to post-surgical wound healing. Additionally, histology showed acute spinal cord hemorrhage in all canines, which was attributed to perimortem CSF collection. Observed bone marrow hyperplasia in CP01 was interpreted as a response to the neutropenia detailed above. Spleen, lungs, adrenal glands, liver, and lymph nodes were unremarkable in all canines. However, pathology did note moderate testicular degeneration and aspermia in CP01 and CP03 that was not anticipated. To further investigate this finding, unilateral castrations of canines CP02 and CP04 were performed to determine if testicular findings were age-, iNSC-, or drug-related. No other unanticipated abnormal pathological findings were observed (Fig. 3.8). To further investigate the testicular abnormalities, unilateral castration was performed on CP04's right testis on the day of craniotomy and the left testis was harvested at necropsy. For CP02, unilateral castration of the right testis was performed 15 days after craniotomy; the left testis was harvested at necropsy. The testis of CP02 harvested at necropsy showed marked tissue degeneration. Aspermia in addition to no active spermatogenesis were observed in the testicle harvested at necropsy in CP04. Due to the extent of degeneration observed in the testes of CP01 and CP03 at necropsy, age-related causes were ruled out. Given the normal histopathology of the pre-surgery testis in CP02, we attributed the abnormal pathological findings in the testes to the VGCV. GCV and acyclovir have both shown extensive reproductive toxicity in animal models, and the FDA has issued a boxed warning for the reproductive toxicity of VGCV.[162–164] These findings strongly suggest that the abnormal testicular pathology seen in the canines is the result of VGCV and not a direct toxicity of the iNSCs. While this cannot be ascertained for certain without additional control canines, we opted to limit our study to four animals for humane reasons.

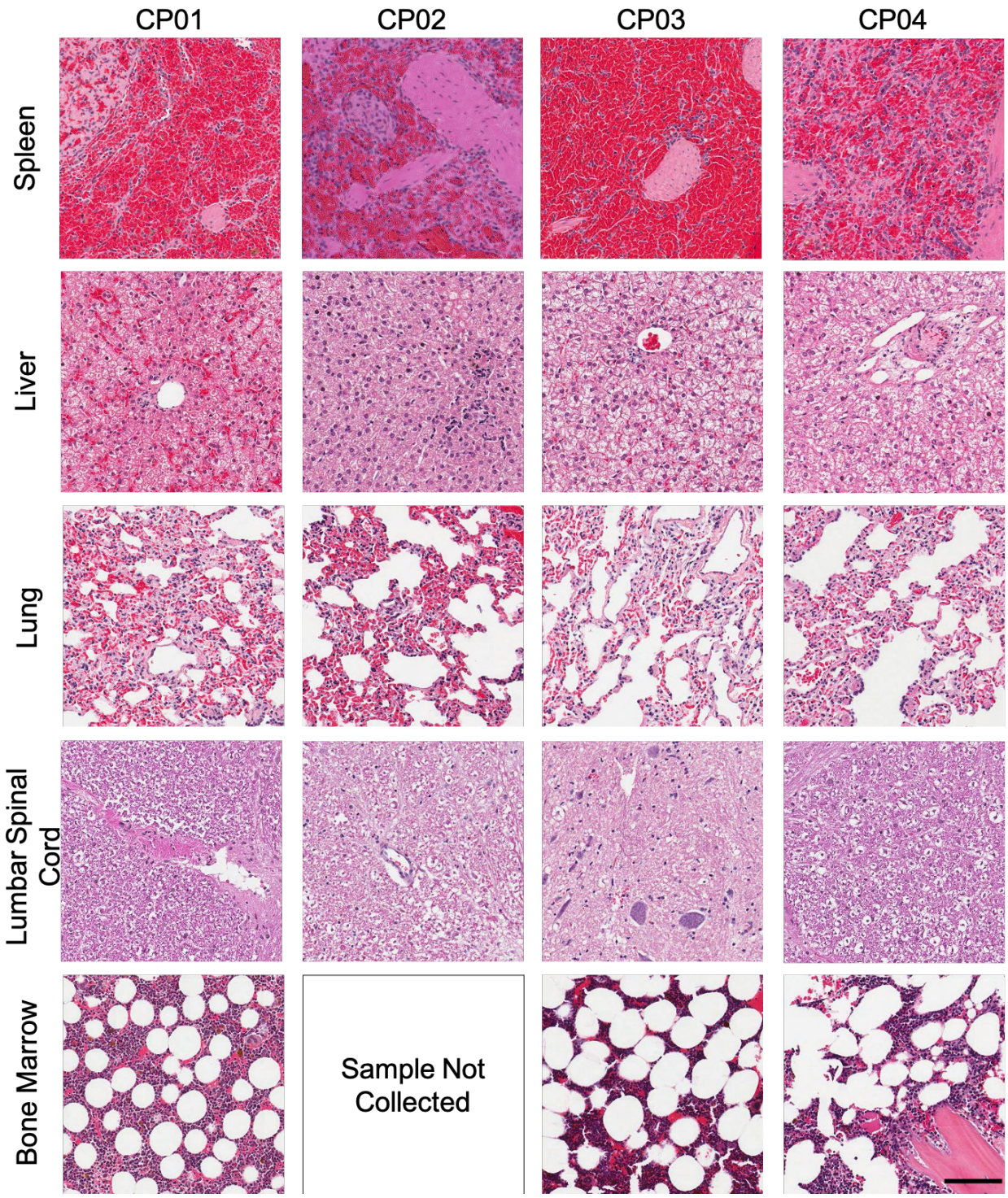

Figure 3.8. Canine Histology. Hematoxylin and eosin staining of canine spleen, liver, lung, bone marrow, and lumbar spinal cord. Scale bar, 200 µm.

3.3. DISCUSSION

NSCs are an emerging new platform for cancer treatment. Their ability to home to distant tumor foci as well as their ability to carry cytotoxic payloads makes them an attractive therapy for GBM. Pre-clinical studies have demonstrated the efficacy of allogeneic human NSCs and human iNSCs in murine models.[63,68,69,148] Promisingly, allogeneic NSCs have entered human clinical trials.[165] However, until now, little data has been published on autologous iNSCs using an animal model that more closely mimics the human condition. To our knowledge, this is the first study to explore the safety, toxicity, and persistence of autologous iNSCs in a large animal model and serves as foundational work for future human clinical trials.

We selected a canine model for several key reasons. First, we required an immune-competent animal. Previous studies using NSCs have been mostly limited to immuno-compromised mice, and therefore lack the ability to identify any adverse reactions or potential safety signals of iNSCs.[63,68,69] Second, it is well established that murine models are not fully indicative of human conditions. The canine anatomy more closely mimics the spatial scale of humans. Furthermore, unlike murine models, which are often inbred, our canine model allowed us to explore interpatient variability. As anticipated, we observed varying proliferation rates and transduction efficiencies in our canine patient fibroblast lines, and these results mimic what is observed in human patients. Third, we desired an animal model that developed GBM tumors similar to that of humans. While xenograft models of GBM in mice, zebrafish, and drosophila have been studied, canines spontaneously develop glioma lesions with characteristics similar to those of human tumors.[166–168] Again, while this study used non-tumor-bearing canines, this was an important consideration for future research. Combining all of this information, we felt a canine model would be best suited to evaluate the safety of iNSCs and served as the ideal model for

forthcoming efficacy studies.

By employing the canine model, we have demonstrated the ability to reproducibly manufacture therapeutic, autologous iNSCs. Using small, full-thickness skin biopsies, we produced large pools of fibroblasts that could easily be cryostored for future use or immediately transduced and transdifferentiated to become therapeutic iNSCs. Clinically, we envision the process of obtaining skin biopsies to be incorporated into patient standard of care. Overall, while we successfully established personalized canine iNSCs lines, there is room for improvement in cell manufacturing scale-up. One of the most challenging aspects of this study was culturing millions of cells for each dose. During the cell collection process, we observed entrapment of cells in extracellular matrix nets, and despite trituration and enzymatic digestion, total iNSC yield increased only marginally. Future studies will explore the use of bioreactors to increase culture efficiency and iNSC yield.

Moreover, we also explored two delivery mechanisms to implant iNSCs in the brains of canines. We first investigated intrathecal delivery using a Rickham® reservoir. ICV reservoirs are used in patients with GBM to deliver chemotherapeutics into the lateral ventricle. Here, chemotherapy follows the flow of CSF to cover the brain and spinal cord and reaches tumor foci via diffusion. While this system is FDA approved and bypasses the blood brain barrier, passive diffusion will prevent the chemotherapy from reaching deep tumor foci.[169,170] Therefore, we believed that combining the ICV reservoir with our migratory iNSCs would overcome several challenges of current treatment strategies and provide a pathway for future clinical translation. In parallel to ICV reservoirs, we also explored a novel delivery strategy using the FDA approved hemostatic matrix FLOSEAL®. FLOSEAL®'s natural components and hydrogel structure made it a promising, biocompatible choice for delivering iNSCs. We hypothesized that encapsulating

iNSCs in FLOSEAL® would increase cell persistence, and in future studies, would correlate to increased survival. Our MRI data suggests that FLOSEAL® aids in iNSC persistence. Histology further shows no unanticipated brain lesions, demonstrating FLOSEAL®'s safety. Overall, we found utility in both delivery mechanisms and believe either device could be used to dispense large iNSC doses into human GBM patients.

With the canine model, we were also able to establish the safety of iNSCs by conducting neurological assessments, screening fluids, and analyzing histology. Postural, gait, and vision abnormalities observed in canines mimicked possible adverse reactions during human brain surgery. Additionally, iNSCs did not elicit any concerning safety signals, regardless of ICV reservoir or FLOSEAL® scaffold delivery, as determined by blood, urine, or CSF. The transient neutropenia and reproductive toxicity findings were unanticipated, but these could due to administration of the prodrug VGCV rather than the iNSCs.

3.4. CONCLUSION

In conclusion, this research demonstrates the feasibility of manufacturing autologous iNSCs as well as their limited toxicity profile. We further show two clinically translatable methods for delivery. Together, this data supports the need for additional large animal efficacy studies and paves the way for future human clinical trials.

3.5. MATERIALS & METHODS

3.5.1. TISSUE HARVEST & DIGESTION

Skin samples were harvested from canines at North Carolina State University; animals were euthanized for reasons unrelated to this study. Immediately following euthanasia, hair was removed using an electric trimmer. The harvest site was sterilized with betadine followed by 70% ethanol, repeated three times. Full thickness skin samples were acquired using a 6 mm diameter biopsy punch. Biopsies were placed in a 15 mL conical tube containing 10 mL 1X PBS and 2X

antibiotic-antimycotic and transported on ice to the University of North Carolina at Chapel Hill. Skin biopsies were individually transferred into new 15 mL conical tubes each containing 1 mL digestion media (DMEM containing 20% FBS, 1% penicillin-streptomycin, 0.25% Collagenase type I, and 0.05% DNase) and incubated at 37°C/5% CO_2 overnight. The next day, the conical tubes were vortexed for 20 seconds to disrupt the skin and disintegrate the dermis. Approximately 7 mL fresh DMEM containing 20% FBS and 1% penicillin-streptomycin was added to the 15 mL tube, and the contents were mixed and transferred to a 10 cm Petri dish. The dishes were returned to the 37°C/5% CO_2 incubator and left undisturbed for 72 hrs.[155]

3.5.2. FIBROBLAST EXPANSION & CELL CULTURE

After 72 hrs, media was exchanged for fresh DMEM (henceforth containing 10% FBS and 1% penicillin-streptomycin). Fibroblasts were cultured in this state until the plate reached >70% confluency. Cells were then expanded and subcultured by lifting in 0.05% trypsin-EDTA for 5 mins, adding DMEM to neutralize trypsin, centrifuging at 1000 rpm for 5 min, aspirating supernatant, re-suspending in fresh DMEM, and re-plating in new 15-cm Petri dishes. Cell strainers (100 μm) were used to separate single cells from residual tissue pieces.

3.5.3. LENTIVIRAL TRANSDUCTION & TRANSDIFFERENTIATION

Fibroblasts were co-transduced with lentiviral reverse tetracycline-controlled transactivator (*rtTA*), *SOX2*, *TK-mCh*, and *TRAIL-eGFP* (Iowa University and Duke University Viral Vector Cores). To transduce fibroblasts, cells were incubated with virus and 1 g/mL polybrene overnight at 37°C/5% CO_2. The following day, the mediate containing virus was aspirated and replaced with fresh DMEM. Cells were monitored for fluorescent signal. Next, to transdifferentiate cells to iNSCs, transduced fibroblasts were plated at a density of $2x10^6$ cells per 15 cm Petri dish in DMEM and incubated overnight at 37°C/5% CO_2. The following day, DMEM was replaced with STEMdiff Neural Induction Medium (STEMCELL Technologies 05835)

containing 2 μg/mL doxycycline (NIM+doxy). NIM+doxy media was replaced every other day for a total of 5 days.

3.5.4. IMMUNOHISTOCHEMISTRY

To confirm lentiviral transduction of mCh-TK and eGFP-TRAIL vectors into fibroblasts, fluorescence microscopy was conducted prior to transdifferentiation of the cell lines. Cells were monitored daily until maximum fluorescence intensity was observed. Percent fluorescence expression was quantified in ImageJ. To determine extent of transdifferentiation, cells were fixed in 10% formalin for 15 min and washed three times in 1X PBS. Next, cells were incubated in blocking buffer (0.5% bovine serum albumin and 0.25% Triton X-100 in 1X PBS) for 30 minutes at room temperature. Primary rabbit anti-SOX2 (Abcam ab97959) antibody was diluted 1:200 in blocking buffer and incubated for 1 hr at room temperature on a shaker. After three 1X PBS rinses, goat anti-rabbit Alexa Fluor 488 secondary antibodies (Invitrogen A27034) were diluted 1:600 in blocking buffer and incubated for 1 hr at room temperature on a shaker, protected from light. After three PBS rinses, Hoechst was added to the samples and incubated for 5 minutes on a shaker, protected from light. Samples were then washed in 1X PBS and imaged. Transduction was deemed successful if >70% of the cells expressed mCh and eGFP, and cells were considered transdifferentiated if >70% of the cells were positive for SOX2.

3.5.5. IRON OXIDE LABELING

On the fifth day of transdifferentiation, iNSCs were labeled with ferumoxytol (AMAG Pharmaceuticals) for MRI imaging. Briefly, 0.0125 mg/mL Lipofectamine 2000 (Invitrogen 11668027) and 0.15 mg/mL ferumoxytol were added to OptiMEM (Gibco), and incubated at room temperature for 1 hr. Next, NIM+doxy media was aspirated from each dish and replaced with 8 mL of the ferumoxytol media. iNSCs were incubated for 4 hrs with the ferumoxytol media at 37°C/5% CO_2. At the completion of 4 hrs, media was aspirated, cells were rinsed with 1X PBS,

and NIM not containing doxy was added back into the dish. Cells were incubated overnight at 37°C/5% CO_2.

3.5.6. CELL COLLECTION

Following transduction and transdifferentiation, iNSCs were harvested for dosing. First, NIM was aspirated from the dishes. Next, cells were incubated with 4 mL of Accutase (STEMCELL Technologies 07922) at room temperature for 5 min. Dishes were then washed with 4 mL of 1X PBS and passed through 100 μm Falcon Cell Strainers (Fisher Scientific 08-771-19). Cells were then pelleted at 1000 rpm for 5 min. The supernatant was then aspirated, and the cells were resuspended in 1X PBS for counting. To count the cells, a 1:1 dilution was made in Trypan Blue (Invitrogen T10282), and the cells were quantified by a Countess II Automated Cell Counter (Invitrogen). For canine studies, cells were transported on ice to North Carolina State University, and at the time of craniotomy, cells that were to be injected ICV were resuspended in 600 μL of artificial CSF (TOCRIS 3525).

3.5.7. *IN VITRO* CELL MIGRATION

Two-well inserts (Ibidi 80209) were placed in dry tissue-culture treated 6-well plates. 8×10^4 MDA-MB-231Br-mCh-Fluc cells (gift from Dr. Toshiyuki Yoneda, University of Texas Health Science Center at San Antonio) were seeded in DMEM in one well of the insert and $4x10^4$ canine iNSCs or control canine fibroblasts were seeded in DMEM in the second well of the insert. Cells were incubated overnight at 37°C/5% CO_2. The following day, DMEM was aspirated and the two-well insert was removed. The cells were then incubated in NIM and serial fluorescence imaging (EVOS FL Auto) was performed over 66 hrs to assess migration.

3.5.8. SCAFFOLD PREPARATION & CELL SEEDING

iNSCs were prepared as described above. FLOSEAL® kits (Baxter 1503350) and components were prepared according to manufacturer's instructions. Briefly, lyophilized thrombin

was reconstituted in 200 mM $CaCl_2$. The prepared thrombin solution was used to resuspend the iNSC cell pellet, and the cell/thrombin solution was loaded into the provided female Luer connector syringe. Next, the Gelatin Matrix was loaded into the Luer Lock syringe; the syringe was sterilized via UV light. Following sterilization, the syringes were connected head-to-head and passaged 20 times to thoroughly mix. The iNSC-containing FLOSEAL® matrix was kept on ice until use.

3.5.9. MURINE *IN VIVO* SURGICAL PROCEDURES

All murine procedures were approved by the Animal Care and Use Committee at the University of North Carolina at Chapel Hill. 6-8-week-old female nude athymic nude mice (Animal Studies Core, University of North Carolina-Chapel Hill) were anesthetized using 2.5% inhaled isoflurane and stabilized in the prone position in a stereotaxic frame. The surgical site was sterilized using 70% isopropyl alcohol and betadine. Next, a midline incision was made on the mouse's head to expose the skull, and the underlying fascia was removed using a cotton swab. Then a burr hole was created with a microdrill. Using a Hamilton syringe, $1x10^6$ unlabeled canine fibroblasts or ferumoxytol-labeled fibroblasts were injected into the brain parenchyma at 1 µL/min. 9 µL of ferumoxytol was used as a positive control. Following injection, the syringe was left untouched for 5 min to prevent reflux. The syringe was then removed slowly, and the incision was closed with Vetbond tissue adhesive (3M 1469SB). Post-operative pain was managed with 5 mg/kg meloxicam.

3.5.10. MURINE MAGNETIC RESONANCE IMAGING

T2 rapid acquisition with relaxation enhancement (RARE) MR images were taken using a Bruker 9.4 T BioSpec scanner. A 72 mm quad-volume coil (Bruker Biospin) was used for radiofrequency transmission. Images were acquired using a repetition time of 10000 ms, echo time

of 8 ms, 15 averages, 51.05 Hz bandwidth, 0.75 mm slices, and 0.1x0.1x0.75 mm resolution. Mice were anesthetized with 3% inhaled isoflurane.

3.5.11. MURINE ORGAN HARVEST & TISSUE PROCESSING

Mice were anesthetized with 5% isoflurane. Cardiac perfusion was done using 5 mL 1X PBS followed by 5 mL 10% formalin into the left ventricle of the heart. Extracted brains were incubated in 10% formalin overnight. The next day, brains were incubated in 30% sucrose in 1X PBS at 4°C until the tissue sank. Brains were then mounted using OCT compound, cut into 40 µm sections, and analyzed as floating sections. To detect the presence of ferumoxytol-labeled iNSCs, tissues were stained with Prussian blue following manufacturer's instructions (Eng Scientific Inc. 3160).

3.5.12. CANINES

Four 1-2-year-old, purpose-bred male beagles were obtained from a United States Department of Agriculture Class A vendor (Oak Hill Genetics). The weights of CP01-CP04 were 14.5, 17.0, 9.9, and 14.8 kg, respectively, prior to surgery. Canines were co-housed in groups of 2, fed a commercial diet twice daily, and provided water *ad libitum*. Physical and neurological examinations, a complete blood count, serum biochemistry and urinalysis were performed at admission to confirm clinically healthy status. All canine procedures were approved by the Institutional Animal Care and Use Committee at North Carolina State University.

3.5.13. CANINE ANESTHETIC & SAMPLING PROCEDURES

Canines were anesthetized for MRI, CSF collection and surgical procedures. Canines were premedicated with hydromorphone (0.1 mg/kg intramuscularly [IM]) and midazolam (0.25 mg/kg IM) and anesthesia was induced with propofol (4 mg/kg intravenously [IV] to effect) and maintained with isoflurane in oxygen (1-3% to effect). Cerebrospinal fluid samples were collected from the cerebellomedullary cistern. Urine samples were collected by urethral catheterization.

Blood, urine, and CSF samples were collected periodically from the canines before and after iNSC implantation.

3.5.14. CANINE iNSC PRODUCTION

The skin of the dorsal cervical region was prepared as described above and 1 x 3 cm full thickness, rectangular skin biopsies were obtained and placed into transport media on ice. iNSCs were manufactured as described above. For post-operative analgesia, canines were given carprofen (4.4 mg/kg SQ followed by 4.4mg/kg PO q 24 hrs for 3 days).

3.5.15. CANINE MAGNETIC RESONANCE IMAGING

Magnetic resonance imaging (MRI) was conducted using 3 different systems as the study overlapped with the decommissioning of an older MRI unit (Siemens 1.5 Tesla Symphony), installation of an upgraded system (Siemens 3.0 Tesla Skyra), and use of a "bridge" unit (Siemens 1.5 Tesla Symphony equipped with older software). Sequences obtained included T1-weighted fast spin echo (FSE), T2-weighted FSE, T1- and T2-weighted fluid attenuated inversion recovery (FLAIR), gradient echo (T2*) and susceptibility-weighted imaging (SWI). T1-weighted images were also obtained after administration of Gadoversetamide (0.1 mmol/kg, Optimark, Mallinckrodt Inc., St. Louis, MO). For the initial MRI studies, a T1-weighted, 3D volumetric sequence was also obtained (MP-RAGE) for use with a veterinary neuronavigation system (BrainSight, Rogue Research, Montreal, Canada). Bite plates affixed with MRI-compatible fiducial markers were also utilized in this initial MRI study as a prelude to neuronavigation and were created using Hydroplastic impression material (Tak Systems, Wareham, MA).

3.5.16. CANINE CRANIECTOMY & iNSC IMPLANTATION

In preparation for craniectomy, canines were anesthetized as described above except that a continuous infusion of propofol (200 ug/kg/min) was utilized to decrease isoflurane requirements. Canines were mechanically ventilated, the head was shaved and surgically prepared and placed in

a head frame for neuronavigation (BrainSight, Rogue Research). The bite plate made prior to the first MRI was replaced and used to register the canine for neuronavigation. The iNSC were delivered in a FLOSEAL® scaffold in two canines and through an intraventricular catheter in the other two canines. To simulate a resection cavity remaining after tumor removal, a craniectomy was created using a high-speed drill followed by durotomy. A 2x2 cm region of cerebral cortex and underlying white matter was removed, centered on the marginal gyrus near the junction of the parietal and occipital lobes. In CP03 and CP04, the iNSC-FLOSEAL® scaffold was injected into the resection cavity; in the canines with intraventricular catheters, the resection cavity was left unfilled. The dura was then manually apposed and covered with an artificial dural product (DuraGen Plus, Integra LifeSciences, Plainsboro, NJ). Neither the dura nor the craniectomy defect were primarily closed. In CP01 and CP02, an intraventricular catheter was placed into the right lateral ventricle after creation of a 6-mm burr hole. The catheter was attached to a Rickham® reservoir that was seated into the burr hole to create a ventriculostomy system (Codman Holter Rickham® reservoir, Integra LifeSciences). The temporalis muscle, subcutaneous tissues, and skin were closed using suture and the skin was closed using staples. A fentanyl patch (50-75 μg/hr) was placed immediately following surgery, and hydromorphone (0.1 mg/kg IV q 6 hours) was administered until the patch took effect approximately 12 hours after placement. For CP01 and CP02, ultrasound navigation was used to inject the second and third iNSC doses into the Rickham® reservoir.

3.5.17. CANINE CASTRATION

In order to further investigate potential reproductive toxicity, CP02 and CP04 underwent unilateral castration for histopathological analysis and sperm evaluation. These procedures were performed using standard techniques and the contralateral testis was similarly evaluated at the time of autopsy.

3.5.18. CANINE POST-OP PROCEDURES & MONITORING

Following intracranial surgery, all canines underwent a neurological exam to assess gait, motor function, postural reactions, segmental spinal reflexes, and cranial nerve function. Blood samples were collected from the ICV cohort at baseline prior to surgery, every other post-operative day through day 7, and then once per week through week 12. The scaffold cohort had blood drawn at baseline, every other post-operative day through day 7, and then once per week through week 8. Urine and CSF were collected from the ICV cohort at baseline and every 2 weeks through day 84. The scaffold cohort had urine and CSF collected at baseline and every 2 weeks through day 56. All animals were routinely monitored for adverse events, pain, and signs of infection. The fentanyl patch, which was applied immediately following during surgery, was removed after 5 days. VGCV was administered 2 weeks following scaffold implantation and 2 weeks after each ICV dose at 450 mg PO qd 5 days.

3.5.19. CANINE EUTHANASIA & NECROPSY

At the study endpoint, all canines were euthanized via an intentional sodium pentobarbital overdose at 85 mg/kg. Necropsy was performed immediately after euthanasia. Tissue samples were fixed in 10% formalin overnight in preparation for histological analysis.

3.5.20. CANINE HISTOLOGY

Hematoxylin and eosin staining was performed on 5 μm sections of formalin-fixed, paraffin-embedded tissue samples. Histopathologic analysis was performed by board-certified veterinary pathologists (L.B.B., D.A.T.).

3.5.21. STATISTICAL ANALYSIS

Data are expressed as mean ± standard deviation.

CHAPTER 4: DEVELOPING BIO-INSPIRED 3D MODELS OF BRAIN CANCER TO EVALUATE TUMOR-HOMING INDUCED NEURAL STEM CELL THERAPY[1]

4.1. INTRODUCTION

Primary malignant brain tumors are responsible for the most years of life lost of any cancer.[171] Of these, glioblastoma (GBM) is the most common and aggressive. Surgery, followed by chemoradiotherapy remains the standard of care, but unfortunately results in a median survival of under 2 years and a 5-year survival rate of <5%.[172] A major reason GBM remains difficult to treat is the highly invasive nature of the disease, where migratory tumor cells invade healthy brain tissue, making recurrence and associated patient mortality nearly inevitable.[104,173,174] Additionally, there is a lack of noninvasive methods of local delivery. Systemic delivery, on the other hand, is hindered by both the blood/ brain barrier and vascular dysfunction in the tumor, which is exacerbated by the fact that many current drugs have short half-lives and therefore do not accumulate to therapeutic concentrations in the brain.[104,175,176] Moreover, brain metastases outnumber primary brain tumors significantly in frequency and result in an even lower median survival: <1 year.[174] New treatments are desperately needed to improve outcomes in all types of brain cancers.

In efforts to develop therapies that are more effective against brain cancer, neural stem cells (NSCs) have been increasingly explored as drug delivery vehicles. Their inherent tropism to

[1]This chapter previously appeared as an article in the journal *Tissue Engineering Part A*. The original citation is as follows: Carey-Ewend, A. *et al*. Developing Bioinspired Three-Dimensional Models of Brain Cancer to Valuate Tumor-Homing Neural Stem Cell Therapy. *Tissue Eng. Part A*. (2020). Reproduced with permission from Mary Ann Liebert, Inc and Tissue Engineering Part A.

tumoricidal agents, to which they confer increased persistence along with active targeting.[176–179] Based on the strength of promising preclinical data in mice, NSC therapy recently entered human clinical trials. Despite the promising advancements, numerous questions around NSC therapy remain due to gaps in relevant models that bridge the size and scale of NSC brain therapy from murine models to human patients.

Tumor-selective homing is one of the most critical and unique aspects of NSC therapy, yet little is known about tumor homing at distances unachievable in size-constrained mouse models. Studies using large animal models are costly to perform in vivo and cannot be recapitulated at scale in commonly used, less-expensive rodent cancer models. As such, in vitro cell migration-based assays remain the mainstay of NSC homing. These include: (1) measurement of cell movement across a scratch or gap, (2) detection of cells having moved through a membrane from one chamber to another, or (3) measurement of cell movement in microfluidic devices capable of three-dimensional (3D) culture.[180–183] Each strategy is limited in terms of the number of cells that can be investigated, and these techniques do not recapitulate migration at the longer distances necessary in a human brain.[184]

Moreover, two-dimensional (2D) culture especially fails to incorporate the physical and chemical cues that regulate NSC migration in vivo and restricts cell–cell interactions.[182] In fact, cells grown in 2D cultures differ significantly in phenotype and genotype from cells grown in vivo or in 3D bioinspired hydrogels.[185] To overcome these limitations we developed a custom, scalable 3D hydrogel system referred to as bioinspired brain matrix (BBM). The model is composed of an agarose base and has poly-l-lactic acid (PLA) 6100 fibers embedded throughout to simulate neural pathways for cell migration.[186] The PLA fibers are distributed homogenously throughout the BBM to create a consistent density of fibers. The use of agarose as opposed to other hydrogels, such as

gelatin, was influenced by material autofluorescence and availability. Our studies suggest that this new BBM offers a cost-effective, clinically relevant platform for investigation of the spatial and temporal kinetics as well as the efficacy of tumor-homing NSCs used to treat brain cancers. We believe our results suggest BBM is a useful surrogate for investigating key questions that are beyond the reach of traditional animal or cell cultures as new cell therapies are advanced toward human patients.

4.2. RESULTS

4.2.1. BBM FABRICATION AND BIOREACTOR DESIGN

To develop cost-effective models that will allow investigation of NSC therapy on a larger scale, two versions of the 3D hydrogel model were produced. The first was a life-sized BBM that measured ~1.5×10^3 cm^3 in volume, and the second was a mini-BBM that was ~$7.5cm^3$, which is comparable to small rodent in vivo models. Figure 1A depicts schematically the development and use of BBMs to study cell growth and migration. Briefly, PLA was sterilized through UV light for 30min in a tissue culture hood and incubated overnight in 3D cell culture medium (DMEM, 1% FBS, 1% antibiotic–antimycotic). Next, 0.6% agarose (w/v) was dissolved in 1:1 PBS:3D cell culture medium and poured over PLA in the plastic mold. Gelation occurred as the agarose cooled at room temperature. Importantly, the resulting BBM was optically transparent to enable noninvasive tracking of cell populations within the matrix.

The mini-BBM (Fig. 4.1B) could be cultured in 6-well polystyrene plates (Fig. 4.1C). However, it was necessary to design a bioreactor in which to culture the human-size BBM (Fig. 4.1D). To this end, a 6-L round polycarbonate container was used as a central housing. An acrylic lid was laser cut to the container's dimensions. The lid was rationally designed with filter inserts to allow for proper gas exchange while remaining sterile. The bioreactor was designed to be

compatible with serial noninvasive optical imaging, thus the walls and lid comprised material that was optically transparent, whereas the base and fittings were designed with black material to minimize the reflection of light during imaging. A custom impeller was 3D printed to circulate nutrients throughout the bioreactor without creating a circular flow pattern that could shear parts of the BBM contained within, a common issue with standard stir bar-based bioreactors.[187]

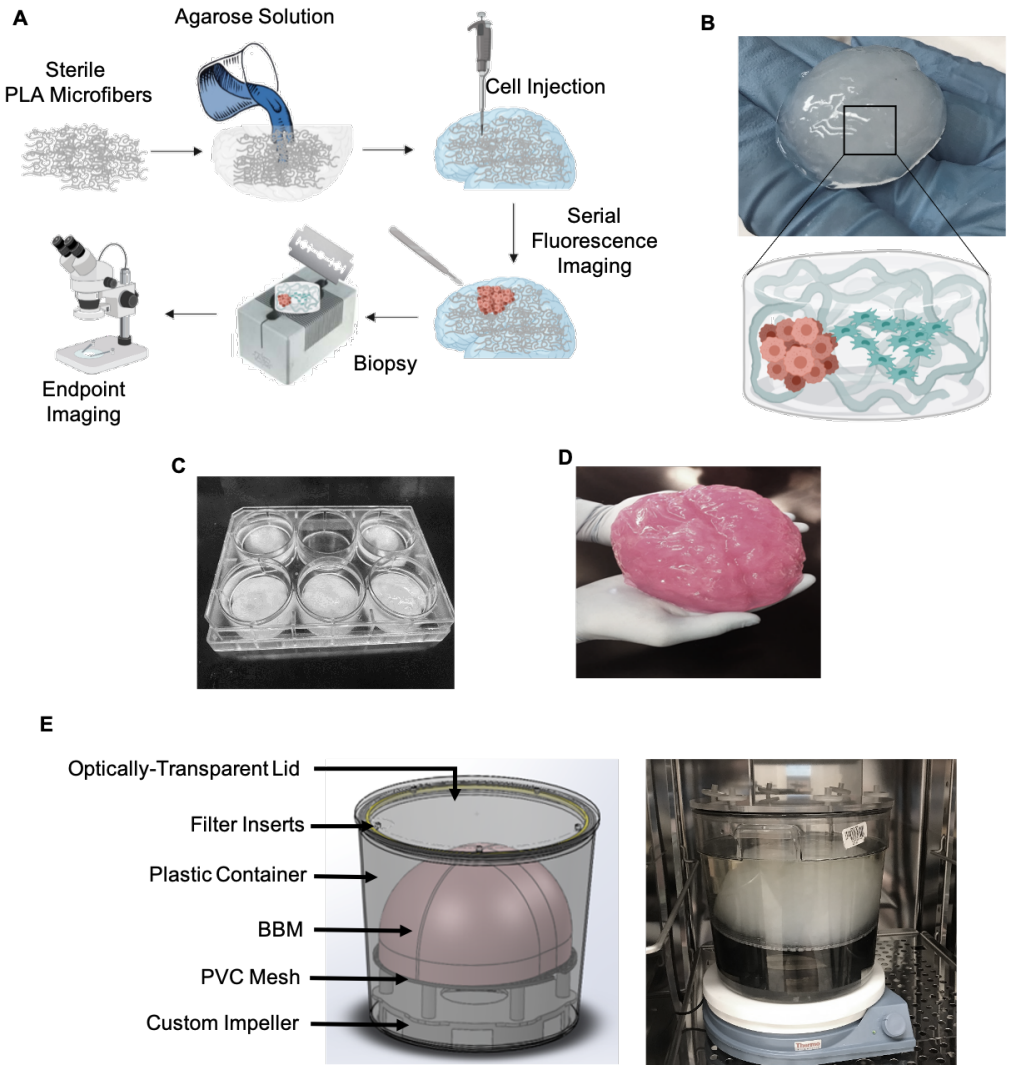

Figure 4.1. BBM and Bioreactor Design. A) Schematic of workflow for BBM fabrication and use in cell growth assay. (B) Representative image of mini-BBM with schematic representation of example set up for tumor-homing assay. (C) Small BBMs can be cultured in polystyrene tissue culture plates. (D) Representative image of large BBM (with added pink dye for contrast). (E) Custom bioreactor for life-size BBM. BBM, bioinspired brain matrix.

4.2.2. CELL–BBM INTERACTIONS

To next investigate the interaction between the PLA fibers and agarose, as well as cell distribution and attachment to the matrix, we utilized scanning electron microscopy (SEM). The SEM images showed that while the PLA fibers were primarily dispersed evenly throughout the matrix, more condensed groups of fibers were present in certain locations (Fig. 4.2A, B). The average PLA fiber diameter was determined to be 15.83-1.99 mm through ImageJ analysis (n = 10) (Fig. 4.2C). With increasing magnification of the BBM agar component, the continuous morphology of the material was interspersed with cracks, which were likely an artifact of the critical point drying procedure (Fig. 4.2D). Following injection of tumor cells, cell clustering and attachment to the agar matrix was observed, directly adjacent to the PLA fibers (Fig. 4.2E, F).

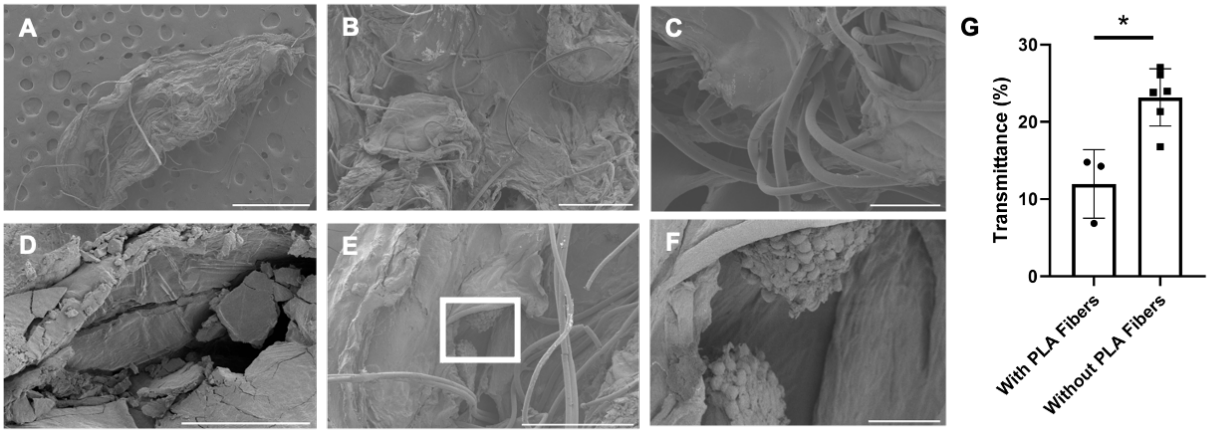

Figure 4.2. BBM Characterization. Interaction between PLA and agar is visualized in (A–C). Cells attached to agarose adjacent to PLA is pictured at low magnification in (E) and high magnification of white square in (F). Scale bars are as follows: (A) 1 mm, (B) 500 mm, (C) 100 mm, (D) 40 mm, (E) 300 mm, and (F) 50 mm. (G) Percent light transmittance of BBMs with and without PLA fibers; n = 3 for samples with PLA fibers; n = 6 for samples without PLA fibers; *p < 0.05. PLA, poly-l-lactic acid.

4.2.3. IMPLANTING GBM TUMORS AND TRACKING GROWTH WITHIN BBMS

Initial experiments sought to characterize growth rates of two different types of brain cancer in both the small and large BBM systems. The tumor cell lines, U87 and MDA-MB-231-

BR (231-BR), were selected due to their sensitivity to TRAIL.[136,188] To first investigate GBM, the human glioma line U87 was engineered to express the optical reporter mCh, and tumor cells were injected 2 mm deep into mini-BBMs at the same cell density used in traditional animal models: 5×10^5 cells in 3 mL (Fig. 4.3A).[104,189] Thirty minutes after implantation, BBMs were immersed in 3D cell culture medium and moved to an incubator for long-term culture. A similar method was used in the life-size BBM model, where 3.0×10^7 mCh cells were implanted ~40 mm deep into the hydrogel, which was then transferred to the bioreactor (Fig. 4.3B). Tumor volume changes were then serially tracked using IVIS imaging. We found that 1 week after implantation, U87 tumor volumes increased 48-fold in the life-size BBM and greater than 52-fold in the mini-BBM (Fig. 4.3C). These growth rates are comparable to experimentally determine in vivo growth rates when these tumors are established in nude mice.[68] Thus, remaining experiments were all conducted using the same tumor cell density as described here.

The testing was then expanded to explore metastatic brain cancer, specifically breast-to-brain metastases. Human 231- BR cells, a brain-seeking variant of the common metastatic breast cancer line MDA-MB-231, was tested because it preferentially metastasizes to brain tissue.[190] In the clinic, brain metastases often present as a multifocal disease. To model this growth pattern, multiple 231-BR tumor foci were established through implants of 2.5 and 5.0×10^5 cells contralateral to each other in both mini- and life-size BBMs (Fig. 4.3D, E). One week following implantation, serial kinetic imaging showed that tumor volume increased ap- proximately fourfold in both the mini- and life-size BBMs after 1 week (Fig. 4.3F), which also closely mimics the growth pattern that has previously been reported in nude mice.[191] Altogether, these data provide evidence that tumor growth in BBMs closely mimic in vivo tumor growth kinetics, an important factor when designing redosing studies and tracking tumor invasion.

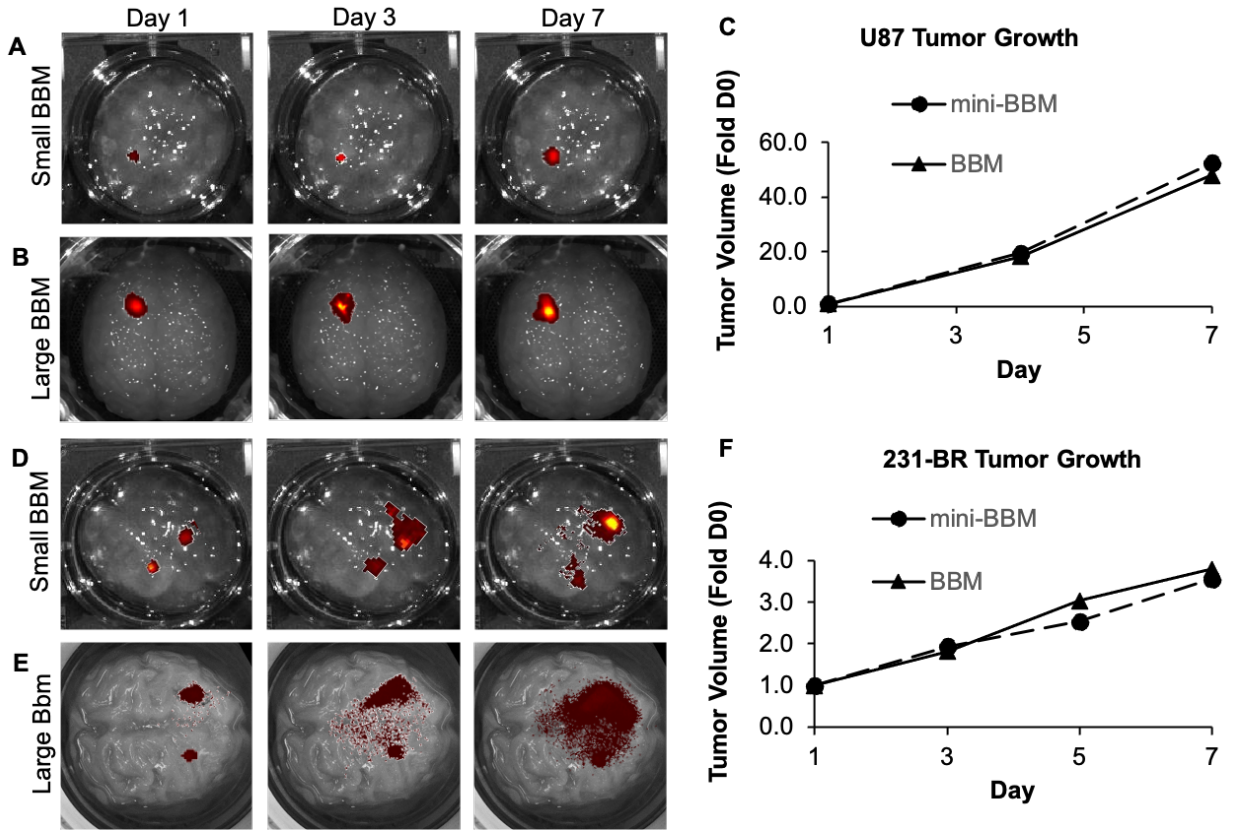

Figure 4.3. Brain Tumor Growth in BBMs. Representative images of GBM fluorescence over 1 week of (A) small and (B) large BBMs. (C) Summary of tumor volumes fold day 0; n=2 for BBM and n=6 for mini-BBM. Additionally, representative images of metastatic breast cancer fluorescence over 1 week in (D) small and (E) large BBMs. (F) Summary data of tumor volumes fold day 0; n=2 for BBM and n=6 for mini-BBM. GBM, glioblastoma.

4.2.4. NSC HOMING TO ESTABLISHED TUMOR IN BBM

The ability of NSCs to migrate through the brain and actively seek out solid and invasive tumor foci is one of the most beneficial aspects of NSC-based therapy for brain cancer. The tumor-homing capacity of NSCs has been extensively studied in mouse models of brain cancer, yet little is known about NSC migration distance capabilities in a human patient. The impact of NSC distance from the tumor and the resulting efficacy is unknown beyond the scale of a mouse. To assess NSC migration in the BBMs, mini-BBMs were first implanted with U87-mCh to establish cancer foci (referred to as ‘‘tumor’’) or with unlabeled fibroblasts to model nontumor foci (referred to as ‘‘nontumor’’). Three days post-tumor implantation, NSCs engineered through transduction

with LVs to express GFP (NSC-GFP) were implanted ~2mm lateral to the tumor or fibroblast focus (Fig. 4.4A). On days 1 and 7 post-implantation, a mini-BBM was fixed, and biopsies containing both cell types were collected and sectioned into ~1 mm slices using a rat brain slicer matrix. Fluorescent micrographs of the slices were captured using a stereomicroscope and fluorescent signal was quantified in ImageJ. Analysis showed that NSCs mi- grated more than 100-fold further in the presence of tumor- containing BBM compared with nontumor-containing BBM, traversing 1.3-0.05 mm of the 2 mm gap between the sites of NSC and GBM implant over the 7-day period (Fig. 4.4B). Quantification of GFP signal in different regions near the injection site or GBM focus further confirmed this migration, as analysis of the fluorescent intensity showed 78%-2.0% of NSC's migrating region of the BBM when implanted near glioma cells for 1 week. When co- cultured with fibroblasts instead, NSCs exhibited no directional migration, with only 25%-0.9% of GFP signal found in the migrating region in the nontumor BBM ImageJ (Fig. 4.4B).

In the clinic, metastatic brain cancer often presents as multifocal disease. To investigate NSC migration to multi- focal tumors, we next implanted mCh-labeled 231-BR cells on contralateral hemispheres of the mini-BBMs ~5 mm apart. Three days later, NSCs were implanted ~1 mm medially to the right tumor (RT), as shown in Figure 4C. After 1 week of coculture, mini-BBMs were processed and fluorescent micrographs were captured and analyzed in ImageJ as before. Analysis showed that NSCs migrated 61-fold further in the presence of tumor compared with nontumor BBM, traversing 2.2-0.1 mm of the 4 mm gap between the NSC injection site and left tumor (LT) implant site over the 7-day period (Fig. 4.4D). Quantification of NSCs at the injection site or near the tumor foci further confirmed this migration, as analysis of the GFP intensity showed that 54%-1.8% of NSCs homed directionally toward the LT, which was, interestingly, further from the initial injection site compared with the RT. Around 29.2%-2.4% of

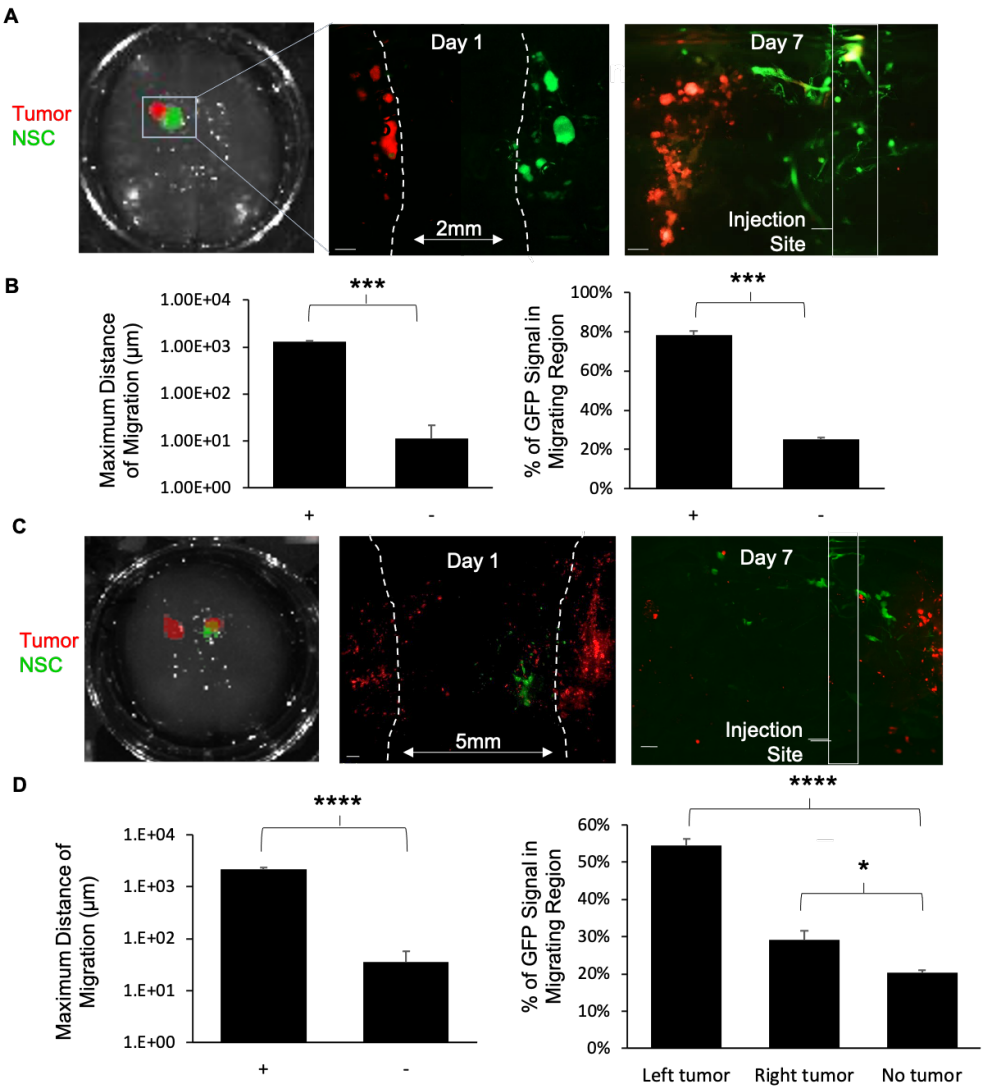

Figure 4.4. NSC Tumor Homing in BBMs. (A) Representative image of mini-BBM fluorescence measured in IVIS and stereo micrographs of fixed samples at days 1 and 7 after initiation of GBM and NSC coculture. (B) Summary data indicating maximum distance of NSC tumor homing and percentage of NSCs found in the migrating region to the left of the injection site as determined by GFP signal quantified in ImageJ. (+) Denotes coculture with tumor and (-) denotes coculture with no tumor. (C) Representative image of mini-BBM fluorescence measured in IVIS and stereomicrographs of fixed samples at days 1 and 7 after initiation of metastatic breast cancer and NSC coculture. (D) Summary data indicating maximum distance of NSC tumor homing and percentage of NSCs found in the migrating regions to the left and right of the injection site as determined by GFP signal quantified in ImageJ. (+) Denotes coculture with tumor and (-) or (no tumor) denotes coculture with no tumor. For all panels n = 3 fields from each two samples per time point, *$p < 0.05$; ***$p < 0.001$, ****$p < 0.0001$. GFP, green fluorescent protein; IVIS, in vivo imaging system; NSC, neural stem cell.

NSCs homed directionally toward the RT. Both enabled significantly more NSC migration than nontumor BBMs, where only 20%-2.0% of GFP signal could be found outside the injection site region (Fig. 4.4D). These results validate the tumor-homing property of NSCs and the usefulness of mini-BBMs for interrogating this key aspect of NSC therapy.

4.2.5. INVESTIGATING THE IMPACT OF DISTANCE ON NSC-INDUCED TUMOR KILL

In human patients, brain cancer foci are likely to present at varying distances from the site of NSC implant or infusion. However, the impact of tumor distance on NSC therapy is not easily investigated in vivo as the small size of the murine model makes implanting multiple tumor foci challenging and limits the distances that can be investigated. To use the BBM system to explore the impact of tumor distance on NSC therapy, U87-mCh were implanted in the mini- BBMs and NSCs engineered to express the antitumor agent TRAIL or control GFP were implanted at 0, 2.0, 5.0, or 10 mm laterally from the tumor (Fig. 4.5A, B). Tumor progression was tracked with weekly kinetic imaging of U87- mCh fluorescence for 1 month. As shown in the summary graph (Fig. 4.5C), NSCs delivered directly into the U87 tumor foci rapidly attenuated tumor progression, reducing tumor volumes to sub-detection levels by day 10 posttreatment and sustaining suppression through 28 days. NSCs implanted 2 mm from the tumor also significantly attenuate tumor growth by day 14, with decrease to sub-detection levels achieved by day 21. Attenuation of tumor growth from NSCs implanted 5 and 10 mm was also found to begin at day 14, however, reduction to sub-detection levels was not achieved until day 28 posttreatment (Fig. 4.5C). On day 14, no statistical significance was observed when comparing the sham group to the 2-, 5-, and 10-mm groups. Statistical significance was observed on day 21; compared with the sham control, the p-values for the 2-, 5-, and 10-mm groups were calculated to be 0.00084, 0.001809, and 0.004413, respectively. On day 28, the p-values for the 2-, 5-, and 10- mm groups were calculated to be

0.00059, 0.000667, and 0.000973, respectively, when compared with the sham control.

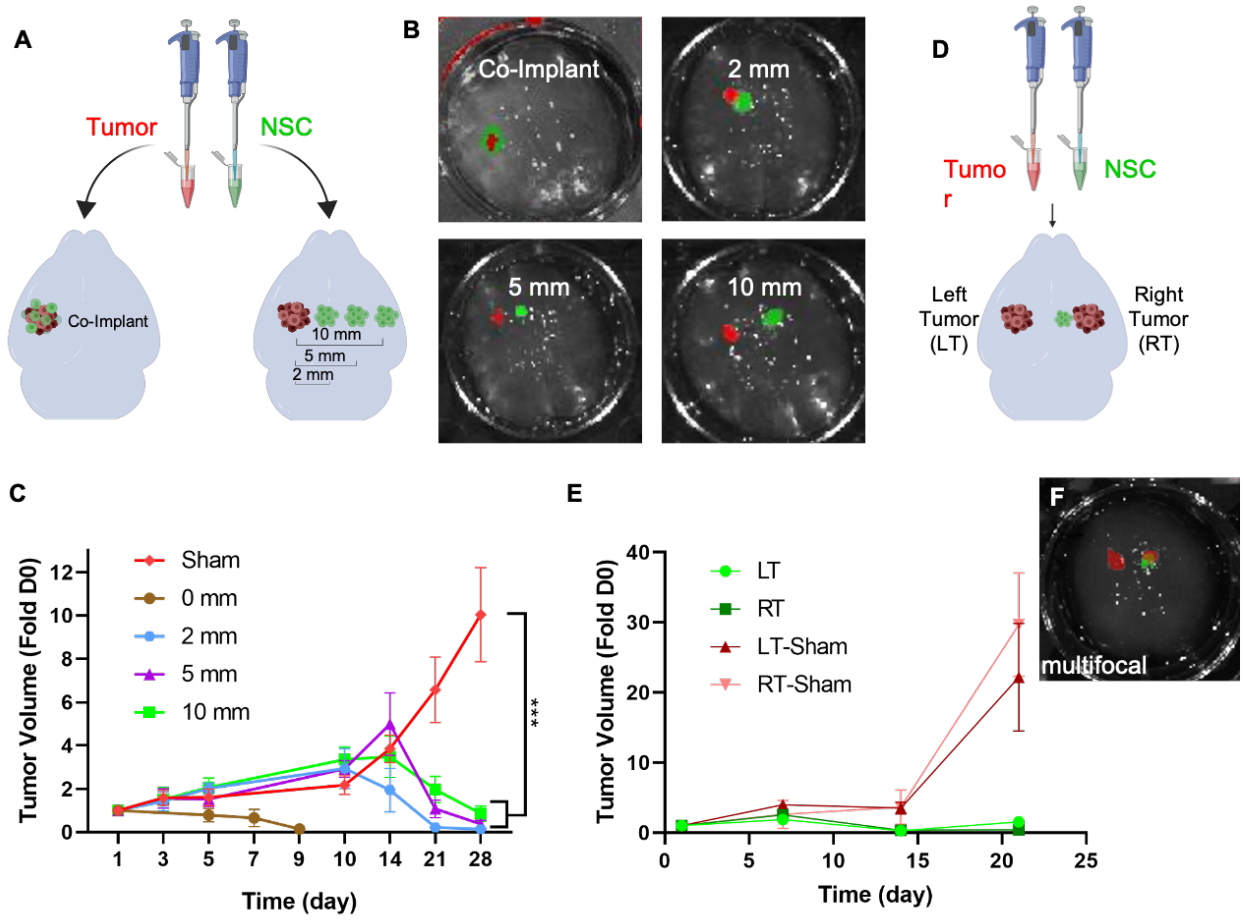

Figure 4.5. Efficacy of NSC-TRAIL as a Treatment Modality Determined Using Different Disease Models in Small BBMs. (A) Schematic of glioma and NSC-TRAIL implant method. (B) Representative images of fluorescent signal in BBMs at day 0 post-seeding. Green represents NSC-TRAIL and red represents U87-mCh. (C) Summary data of tumor volume fold change as determined by serial fluorescent imaging. (D) Schematic of breast cancer brain metastasis and NSC-TRAIL establishment; n≥3. (E) Summary data of tumor volume fold change as determined by serial fluorescent imaging. In all experiments, ‘‘sham’’ is used to represent treatment with NSC-GFP instead of NSC-TRAIL; n=3. (F) Representative image of fluorescent signal in BBMs at day 0 post-seeding. Green represents NSC-TRAIL and red represents 231-BR-mCh. mCh, mCherry; TRAIL, TNFα-related apoptosis-inducing ligand.

Lastly, we explored the potential efficacy of NSC therapy for multiple tumor foci. NSC migration is dependent on chemotaxis, thus it is possible that multifocal tumors may split the dose

of therapeutic NSCs across multiple foci, resulting in altered killing. To investigate this relationship, 231-BR-mCh cells were implanted in each hemisphere of the mini-BBM, ~5 mm apart. NSC-TRAIL or NSC-GFP were implanted directly adjacent to the tumor in the right hemisphere (RT), and tumor volumes were measured serially for 3 weeks (Fig. 4.5E). As shown in the summary data, serial kinetic imaging showed that NSC-TRAIL treatment reduced both tumor foci by greater than 70% 14 days posttreatment despite the closer proximity to the GBM in the right hemisphere (Fig. 4.5E). Interestingly, imaging results showed the tumor in the left hemisphere (LT) began to trend toward regrowth at day 21, and the change in signal was statistically significant compared with the GBM in the right hemisphere (Fig. 4.5E). In contrast, tumors in both hemispheres expanded rapidly in BBMs implanted with control NSC-GFP.

4.2.6. BBM FABRICATION AND BIOREACTOR DESIGN

Transmittance was calculated using light absorbance values of the mini-BBMs. Percent transmittance was determined to be 11.96 – 4.43 and 23.17 – 3.71 in mini-BBMs with and without PLA fibers, respectively (Fig. 4.2G).

4.3. DISCUSSION

Engineered NSC therapy is a promising new approach to cancer therapy. Multiple aspects of NSC migration and killing are impacted by the microenvironment, making the ideal potency assay for NSC-based therapeutics for brain cancer models that recapitulate the physical properties of brain tissue. With this in mind, BBMs were made to physically resemble the brain perivascular niche through embedding of microfiber PLA.[192–196] PLA was chosen due to its biocompatibility as it has been used in several cell migration assays and tissue regeneration studies.[102,196] Agarose as a base also presents a number of advantages. First, low concentration agarose gels (0.2–0.6%) have been shown to mimic the poroelasticity and backflow of the brain.[197,198] Second, its deformability makes it easily injectable, and collective cell migration, which is more relevant to cell behavior in

vivo, can be studied.[199,200] Third, it is considerably less expensive than other hydrogels designed to mimic the tissue microenvironment, such as collagen[181,184,201] or Matrigel.[180,202] Fourth, the Young's modulus of soft agarose closely mimics that of healthy brain tissue; this is critical, because several studies have reported that the viscoelastic properties of a substrate can impact cells' proliferation, differentiation, and migration characteristics.[126,203–205] While agarose shows promise in this study, future optimization of BBMs will include exploration of other transparent matrices, such as alginate. Lastly, the transparent nature of the BBM allows for accessible serial imaging using in vivo fluorescent imaging systems (IVIS). IVIS imaging is efficient at locating the general presence of cells in a 2D space. To better understand the 3D spacing of cells, we performed initial experiments that explored the use of light-sheet microscopy (LSM) and confocal microscopy. For LSM, the BBM samples were prepared using the iDISCO+ protocol and stained with validated antibodies.[206] However, NSCs were not visualized; this was likely caused by the inability of the antibodies to diffuse through the dense BBM. Confocal imaging was also nonideal due to the size of the sample and the spread of the cells in the x-y plane. Future studies combining BBMs with different imaging modalities would further optimize the BBM system and also provide unique insights into cellular and molecular events that occur during both the progression of brain cancers and following response to therapies.

As a result, rationally designed BBMs were able to model both tumor growth and NSC tumor homing that occurs in vivo in nude mouse xenograft models of brain cancer.[68,191,207] From there, experiments using BBMs revealed the impact of distance between NSC and tumor foci on therapeutic efficacy. Clinically, GBM tumor regrowth occurs within 2 cm of the tumor resection cavity.[208] Therefore, the distances of 2, 5, and 10mm were selected to mimic these clinical findings. When implanting therapeutic NSCs and GBM, onset and extent of tumor suppression varied

inversely with initial NSC distance from the established tumor focus. While therapeutic NSCs implanted into 231- BR models did not impact the timing of the onset of tumor suppression, the tumor contralateral to the NSC initial injection site began to recur <2 weeks later. More investigation into the mechanism for recurrence is needed, but it could be due to metastatic invasion and therefore escape from the region of effect created by diffusion of TRAIL secreted by therapeutic NSCs.[174,181,197,209,210] Additionally, while SDF-1, CXCR4, VEGF, and EGF are believed to play roles in NSC migration, the exact mechanism has yet to be elucidated.[186] To maximize efficacy of NSC-based therapies, optimization of dosing strategies is needed; more research into the effects of cell density, total cell dose, frequency of dosing, and potential for cell conditioning, among others, on cell migration, and therefore potency, must be conducted.

In the case of autologous NSC-based therapies, a method for high-throughput screening of migration kinetics between cells derived from different patients is needed to determine reduction to practice. We present this multiscale 3D biomimetic model of brain cancer to fulfill this need. It is our hope that ongoing studies of efficacy using NSC-based therapies against GBM in life-size BBMs can accurately reflect what can be expected as this therapeutic approach is adapted for clinical use. Using this method to examine the effect of dosing strategy on therapeutic cells at a human-size scale should provide more reliable data than current commonly used approaches, as cells prefer to migrate through a soft matrix rather than through a membrane or across a rigid surface.[182]

4.4. MATERIALS & METHODS

4.4.1. CELL LINES

U87 glioma cells were purchased from the American Type Culture Collection and cultured according to manufacturer's specifications. Human fibroblasts (NHF1) were provided by W.

Kauffman (University of North Carolina School of Medicine). 231-BR cells were provided by Carey Anders (University of North Carolina Lineberger Cancer Center). C17 mouse NSCs were used in all NSC experiments and were acquired from Sigma-Aldrich. Each cell line was cultured at 37°C, 5% CO_2 in Dulbecco's modified Eagle's medium (DMEM, 10% fetal bovine serum [FBS], 1% penicillin– streptomycin; Gibco). Cells were engineered to express green fluorescent protein (GFP), mCherry (mCh) fluorescent protein, and/or TNFα-related apoptosis-inducing ligand (TRAIL) through a 24-h transduction with lentivirus (LV) in the presence of polybrene (8 mg/mL; Sigma). All LV constructs were packaged as LV vectors in 293T cells using a helper virus-free packaging system as described previously.[68,69]

4.4.2. BBM FABRICATION

The BBMs were fabricated by mixing 3D cell culture medium (DMEM [1% antibiotic–antimycotic, 1% gluta- mine, 2% FBS, no phenol red]; Gibco) with a 1.2% w/v agarose (Gene Mate LE Agarose; BioExpress) dissolved in phosphate-buffered saline (PBS) at a 1:1 ratio. This solution was poured into a plastic mold with 2.2 mg/mL meltblown PLA 6100 scaffold microfibers, which were obtained from the Non-Wovens Institute at North Carolina State University. Before being added to the mold, the PLA fibers were sterilized using ultraviolet (UV) light and hydrated in the 3D medium overnight. Next, the fibers were manipulated using forceps to distribute the fibers homogenously throughout the BBM solution as it cooled. The BBMs were incubated at room temperature to allow gelation before transferring from the mold to the appropriate cell culture incubator. BBMs were kept hydrated using 3D medium and incubated at 37°C/5% CO_2. Medium was changed every 3–4 days.

4.4.3. BBM CELL SEEDING

To inoculate the BBM with NSCs and tumor cells, the cells were suspended at the desired concentration in DMEM. To allow for injection without backflow, the pipette was inserted 10 mm into the BBM, then withdrawn ~5 mm to create a cavity in which to inject the cells. Cells were injected at a concentration of 5.0×10^4 cells in 3 mL for the mini-BBMs or 3.0×10^7 in 100 mL for the life-size BBMs. The seeded BBM was incubated at room temperature for 30 min to allow the cells to adhere before being immersed in 3D media and incubated at 37°C, 5% CO_2.

4.4.4. SCANNING ELECTRON MICROSCOPY

BBM samples were prepared, seeded, and cultured as described above. Fourteen days post-seeding, BBMs were fixed using 10% formalin then transferred to 1 · PBS. Using an 8 mm biopsy punch and scalpel, samples were trimmed to the region surrounding the injection site, where cells would be most likely to persist. The samples were then dehydrated sequentially in 50%, 75%, 90%, and 100% ethanol. Next, samples were dried using a critical point dryer (Tousimis Autosamdi-931), mounted on aluminum stubs, and sputter coated with 8nm of gold–palladium (Cressington Sputter Coater 108auto). The samples were imaged on a FEI Helios 600 Nanolab Dual Beam System microscope using a 2 kV accelerating voltage.

4.4.5. BBM SERIAL IMAGING

The BBMs were imaged on an in vivo imaging system (IVIS Kinetic; Caliper LifeSciences) for fluorescence. Media were aspirated from the samples before imaging. Cells expressing GFP were probed for using an excitation and emission wavelength spectrum of 465–500 nm, and the mCh-expressing cells were observed using a spectrum of 570–620 nm. An exposure time of 5 s was used for all im- aging sessions. Tumor signal was quantified using Living Image software. Following imaging, the BBMs were resuspended in 3D media and returned to the incubator.

4.4.6. EVALUATING BBM OPTICAL TRANSPARENCY

Mini-BBMs were fabricated as previously described and kept in a six-well plate with 3D media. Absorbance was read at 426 nm using a Molecular Devices SpectraMax M2 plate reader. Percent transmittance was calculated using the following formula, $\%T = 10^{(2-A)}$, where A is absorbance and T is transmittance. Data were analyzed using Student's t-test with Welch's correction.

4.4.7. STATISTICS

Data were analyzed by the Student's t-test, one-way analysis of variance/Bonferroni, or log-rank test when ap- propriate. Data were expressed as mean ± standard deviation. Significance between groups was denoted by *p < 0.05; **p < 0.01; ***p < 0.001. Replicate number is defined by n in figures.

CHAPTER 5: NEXT GENERATION CELL DELIVERY SYSTEMS

5.1. FUTURE DIRECTIONS AND CONSIDERATIONS

Though considerable progress has been made towards the development of scaffolds for the delivery of iNSCs, the optimal system has yet to be found. As discussed in Chapter 1, TISSEEL®, Gelfoam®, HySTEM™ , Ace-DEX, and PLA demonstrated how scaffolds could improve stem cell persistence and survival outcomes. Despite the benefits observed with FLOSEAL® outline in Chapter 2, significant and consistent improvements in survival outcomes were not observed. In order to achieve these goals, the next generation of cell delivery systems need to address the pitfalls of previous formulations through rational design.

Cell binding, material biocompatibility, handleability, degradation, and size are key considerations when designing scaffold systems. However, these properties can only be tuned to a certain degree, if at all, when using an off-the-shelf product like TISSEEL® or FLOSEAL®. The level of tunability necessary to produce the optimal scaffold requires more sophisticated fabrication methods and materials. To develop the next generation of cell delivery materials, continuous liquid interface production (CLIP) and peptide nanofibers are two of the most promising technologies.

5.1. CONTINUOUS LIQUID INTERFACE PRODUCTION

CLIP is a new additive manufacturing technology, with the first patent filed in 2014 and data published in 2015.[211,212] In brief, CLIP uses a bottom-up printing strategy wherein a pool of liquid resin sits above an oxygen-permeable window, and below the window sits a ultraviolet light source. With this set-up, a “dead zone” is created, which allows for a thin region of uncured resin

and oxygen flow. The invention of CLIP drastically decreased the time taken to print an object by controlling oxygen in the resin pool. Additionally, CLIP has the added ability to produce objects with a feature resolution of less than 100 μm, a vast improvement over traditional 3D printers.[211,213] Since its inception, CLIP has since demonstrated its versatility in creating a host of products, including dentures, medical swabs, and surgical tools that are already in commercial production.[211,214]

More recently, researchers have begun to explore how CLIP can be used with a variety of synthetic polymers to create implantable medical devices. Polycaprolactone and poly(ethylene glycol), nano-hydroxyapatite and poly(ethylene glycol)diacrylate, and methacrylated poly(dodecamethylene citrate) have been studied for their use in small molecule drug delivery, tissue engineered bone constructs, and bioresorbable cardiovascular stents, respectively.[213,215–217] Given the preliminary success of these devices, there is evidence to support the testing of CLIP for iNSC delivery scaffolds.

5.2. PEPTIDE NANOFIBERS

While CLIP offers a new way to produce intricate scaffold architectures, peptide scaffolds are an innovative materials-based strategy, and their flexibility makes them an attractive choice. As discussed in Chapter 2, the mechanical properties and interactions between a cell and material can impact gene expression. With peptide scaffolds, the mechanical properties can be easily tuned by controlling the salt concentration of the gelling solution.[218] Additionally, the abundance of functional groups allows for conjugation of a variety of cells, growth factors, and other therapeutics.[218–220] In the case of iNSC therapy, peptide scaffolds would allow for combination therapies, i.e. cells and an additional therapy, to be delivered simultaneously, potentially resulting in a new, synergistic treatment. The scaffolds could also be engineered with growth factors or

proteins to support iNSC growth. Lastly, peptide scaffolds also offer the benefit of being injectable and bioresorbable.[218,220] Overall, peptide scaffolds offer a promising solution to the drawbacks of current popular polymers.

CHAPTER 6: SUMMARY AND PROSPECTUS

Biomaterial matrices for the delivery of therapeutic iNSCs have proven vital to their persistence and therapeutic longevity. The data presented in this dissertation: (a) demonstrates the profound impact FLOSEAL® has on iNSC persistence *in vivo*, (b) establishes the safety of iNSCs delivered with and without FLOSEAL® in a large animal model, (c) presents novel GBM models to screen and validate cell therapies, and (d) looks into the next generation of cell delivery systems.

Chapter 2 discussed the importance of delivery matrices, specifically the gelatin-thrombin mixture, FLOSEAL®. Through rigorous investigation, FLOSEAL® proved to be a desirable material that supported iNSC proliferation and persistence in murine models. Although persistence did not correlate to increased survival outcomes in all treated animals, these studies highlighted the need for delivery matrices that could provide an initial burst release of therapeutics followed by a sustained release. Furthermore, the gene expression profiles of iNSCs cultured in FLOSEAL® *in vitro* produced interesting results. In line with previous studies, differentiation, proliferation, pluripotency, and some NSC markers were downregulated. qRT-PCR also provided insight on potential iNSC migration markers. Overall, FLOSEAL® remains a promising candidate for iNSC delivery.

In the following chapter, the first safety and toxicity study of autologous iNSCs was presented. This chapter assessed the process and challenges of large-scale cell manufacturing as well as the delivery of iNSCs using a clinically-relevant ICV infusion device and FLOSEAL®. Through serial blood, urine, and CSF analysis, MRI, and post-mortem histology, iNSCs were

found to exhibit limited toxicity in canines. The positive outcomes from this study will ultimately inform future efficacy studies in large animal models.

Chapter 4 introduced an innovative 3D culture system to screen and optimize stem cell therapy. The BBMs were able to support the growth of implanted tumors and therapeutic stem cells, and importantly, the BBMs allowed for serial optical imaging. Not only did the culture system prove practical, but it also provides an alternative to animal research. BBMs are cheaper, more high-throughput, and can be cultured in an easily 3D-printed bioreactor. The development of culture systems like BBMs will help expedite cell therapy research.

Lastly, Chapter 5 discussed cell delivery systems that are under development. The CLIP and peptide scaffolds seek to address the pitfalls of previous researched scaffolds through rational design and enhanced tunability. Although both scaffolds are in the preliminary stages of development, they have shown promise in promoting stem cell seeding efficiency, persistence, and migration. However, continued research and optimization will be necessary to select a formulation that promotes cell persistence and migration while simultaneously providing optimal therapeutic profiles.

Taken together, this data presented in this dissertation provides the foundation for future cell delivery matrix optimization. As research and technology continue to advance, improvements in bioreactors, material formulations, and tumor models will be vital to push autologous therapeutic stem cells through clinical trials and ultimately to the clinic.

REFERENCES

1. Tamimi, A. F. & Juweid, M. *Epidemiology and Outcome of Glioblastoma*. *Glioblastoma* (Codon Publications, 2017). doi:10.15586/CODON.GLIOBLASTOMA.2017.CH8

2. Parsons, D. W. *et al*. An Integrated Genomic Analysis of Human Glioblastoma Multiforme. *Science (80-.).* **321**, 1807–1812 (2008).

3. Kfoury, N. *et al*. Cooperative p16 and p21 action protects female astrocytes from transformation. *Acta Neuropathol. Commun.* **6**, 12 (2018).

4. Ho Lee, J. *et al*. Human glioblastoma arises from subventricular zone cells with low-level driver mutations. *Nature* (2018). doi:10.1038/s41586-018-0389-3

5. Zhao, Z., Nelson, A. R., Betsholtz, C. & Zlokovic, B. V. Establishment and Dysfunction of the Blood-Brain Barrier. *Cell* **163**, 1064–1078 (2015).

6. Rascher, G. *et al*. Extracellular matrix and the blood-brain barrier in glioblastoma multiforme: spatial segregation of tenascin and agrin. *Acta Neuropathol* **104**, 85–91 (2002).

7. Rodriguez, A., Tatter, S. B. & Debinski, W. Neurosurgical techniques for disruption of the blood–brain barrier for glioblastoma treatment. *Pharmaceutics* **7**, 175–187 (2015).

8. Armento, A., Ehlers, J., Schotterl, S. & Naumann, U. Molecular Mechanisms of Glioma Cell Motility. in *Glioblastoma* 73–93 (Codon Publications, 2017). doi:10.15586/codon.glioblastoma.2017.ch5

9. Davis, M. E. Glioblastoma: Overview of disease and treatment. *Clin. J. Oncol. Nurs.* **20**, (2016).

10. Holland, E. C. Glioblastoma multiforme: The terminator. *PNAS* **97**, 6242–6244 (2000).

11. Jain, K. K. A critical overview of targeted therapies for glioblastoma. *Frontiers in Oncology* **8**, (2018).

12. Schumacher, T. N. & Schreiber, R. D. *Neoantigens in cancer immunotherapy*.

13. Lawrence, M. S. *et al*. Mutational heterogeneity in cancer and the search for new cancer-associated genes. *Nature* **499**, 214–218 (2013).

14. Reardon, D. A., Wucherpfennig, K. & Chiocca, E. A. Immunotherapy for Glioblastoma: On the Sidelines or in the Game? *Discov. Med.* (2017).

15. Zong, H., Gw Verhaak, R. & Canoll, P. The cellular origin for malignant glioma and prospects for clinical advancements. (2012). doi:10.1586/erm.12.30

16. Von Bartheld, C. S., Bahney, J. & Herculano-Houzel, S. The Search for True Numbers of

Neurons and Glial Cells in the Human Brain: A Review of 150 Years of Cell Counting HHS Public Access. *J Comp Neurol* **524**, 3865–3895 (2016).

17. Gilbertson, R. J. & Rich, J. N. Making a tumor's bed: Glioblastoma stem cells and the vascular niche. *Nat. Rev. Cancer* **7**, 733–736 (2007).

18. Wen, P. Y. & Kesari, S. *Medical Progress Malignant Gliomas in Adults. N Engl J Med* **359**, (2008).

19. Stupp, R. *et al*. Effects of radiotherapy with concomitant and adjuvant temozolomide versus radiotherapy alone on survival in glioblastoma in a randomised phase III study: 5-year analysis of the EORTC-NCIC trial. *Lancet Oncol* **10**, 459–466 (2009).

20. Gallego, O. Nonsurgical treatment of recurrent glioblastoma. *Curr. Oncol.* **22**, (2015).

21. Temozolomide: Drug information. *UpToDate* Available at: https://www-uptodate-com.libproxy.lib.unc.edu/contents/temozolomide-drug-information?search=temozolomide drug information&source=panel_search_result&selectedTitle=1~87&usage_type=panel&kp_tab=drug_general&display_rank=1. (Accessed: 30th May 2020)

22. Boiardi, A. *et al*. Treatment of recurrent glioblastoma: Can local delivery of mitoxantrone improve survival? *J. Neurooncol.* **88**, 105–113 (2008).

23. Report, A. P. INFUSIONS (" LYMPHOCYTES ") IN THE TREATMENT OF.

24. Murphy, J., Bowers, M. E. & Barron, L. Optune®: Practical nursing applications. *Clin. J. Oncol. Nurs.* **20**, 14–19 (2016).

25. Fabian, D. *et al*. Treatment of glioblastoma (GBM) with the addition of tumor-treating fields (TTF): A review. *Cancers* **11**, (2019).

26. Stockhammer, F. *et al*. Continuous low-dose temozolomide and celecoxib in recurrent glioblastoma. *J. Neurooncol.* **100**, 407–415 (2010).

27. Brain Tumor Cell Lines. *ATCC* (2020). Available at: https://www.atcc.org/~/media/PDFs/Marketing Material/Cell Biology/Brain Tumor Cell Lines.ashx. (Accessed: 15th February 2021)

28. A-172 [A172] ATCC ® CRL-1620™ Homo sapiens brain glioblastom. Available at: https://www.atcc.org/products/all/CRL-1620.aspx#characteristics. (Accessed: 16th February 2021)

29. Diserens, A. C. *et al*. Characterization of an established human malignant glioma cell line: LN-18. *Acta Neuropathol.* **53**, 21–28 (1981).

30. LN-18 ATCC ® CRL-2610™ Homo sapiens brain/cerebrum; right t. Available at: https://www.atcc.org/products/all/CRL-2610.aspx#characteristics. (Accessed: 16th

February 2021)

31. Duhart, J. M., Brocardo, L., Caldart, C. S., Marpegan, L. & Golombek, D. A. Circadian Alterations in a Murine Model of Hypothalamic Glioma. *Front. Physiol.* **8**, 864 (2017).

32. Lenting, K., Verhaak, R., Mark Ter Laan, ·, Wesseling, P. & Leenders, W. Glioma: experimental models and reality. *Acta Neuropathol* **3**, 263–282 (2017).

33. Watanabe, T. *et al*. Methylation of the p73 gene in gliomas. *Acta Neuropathol.* **104**, 357–362 (2002).

34. T98G [T98-G] ATCC ® CRL-1690™ Homo sapiens brain glioblastom. Available at: https://www.atcc.org/products/all/CRL-1690.aspx#characteristics. (Accessed: 16th February 2021)

35. Eisemann, T. *et al*. An advanced glioma cell invasion assay based on organotypic brain slice cultures. *BMC Cancer* **18**, 103 (2018).

36. Torsvik, A. *et al*. U-251 revisited: Genetic drift and phenotypic consequences of long-term cultures of glioblastoma cells. *Cancer Med.* **3**, 812–824 (2014).

37. Hickman, J. A. *et al*. Three-dimensional models of cancer for pharmacology and cancer cell biology: Capturing tumor complexity in vitro/ex vivo. *Biotechnol. J.* **9**, 1115–1128 (2014).

38. van Steden, R., van der Wal, Z. & Lasthuizen, K. Hydroxyurea sensitizes glioblastoma to temozolomide. in *Treatment sensitizers for high-grade brain tumors* **47**, 220–243 (2015).

39. Barth, R. F. & Kaur, B. Rat brain tumor models in experimental neuro-oncology: the C6, 9L, T9, RG2, F98, BT4C, RT-2 and CNS-1 gliomas. *J Neurooncol* **94**, 299–312 (2009).

40. F98 ATCC ® CRL-2397™ Rattus norvegicus brain undifferentiat. Available at: https://www.atcc.org/products/all/CRL-2397.aspx#characteristics. (Accessed: 15th February 2021)

41. Kijima, N. & Kanemura, Y. Mouse Models of Glioblastoma. in *Glioblastoma* 131–139 (Codon Publications, 2017). doi:10.15586/codon.glioblastoma.2017.ch7

42. Oh, T. *et al*. Immunocompetent murine models for the study of glioblastoma immunotherapy. *Journal of Translational Medicine* **12**, 107 (2014).

43. Riva, M. *et al*. CT-2A neurospheres-derived high-grade glioma in mice: a new model to address tumor stem cells and immunosuppression. (2019). doi:10.1242/bio.044552

44. A.V., T., Dinda, A. K. & Koul, V. Evaluation of nano hydrogel composite based on gelatin/HA/CS suffused with Asiatic acid/ZnO and CuO nanoparticles for second degree burns. *Mater. Sci. Eng. C* **89**, 378–386 (2018).

45. Oh, T. *et al*. *Immunocompetent murine models for the study of glioblastoma immunotherapy*. (2014). doi:10.1186/1479-5876-12-107

46. Cohen, J. 'Any idiot can do it.' Genome editor CRISPR could put mutant mice in everyone's reach. *Science (80-.)*. (2016). doi:10.1126/science.aal0334

47. Dickinson, P. J. *et al*. Canine spontaneous glioma: A translational model system for convection-enhanced delivery. *Neuro. Oncol*. **12**, 928–940 (2010).

48. Satterlee, A. B., Dunn, D. E., Lo, D. C., Khagi, S. & Hingtgen, S. Tumoricidal stem cell therapy enables killing in novel hybrid models of heterogeneous glioblastoma. *Neuro. Oncol*. **21**, 1552–1564 (2019).

49. Kondru, N. *et al*. An Ex Vivo Brain Slice Culture Model of Chronic Wasting Disease: Implications for Disease Pathogenesis and Therapeutic Development. *Sci. Rep*. **10**, 1–12 (2020).

50. Linkous, A. *et al*. Modeling Patient-Derived Glioblastoma with Cerebral Organoids. *Cell Rep*. **26**, 3203-3211.e5 (2019).

51. Ogawa, J., Pao, G. M., Shokhirev, M. N. & Verma, I. M. Glioblastoma Model Using Human Cerebral Organoids. *Cell Rep*. **23**, 1220–1229 (2018).

52. Tavazoie, M. *et al*. A Specialized Vascular Niche for Adult Neural Stem Cells. *Cell Stem Cell* **3**, 279–288 (2008).

53. Obernier, K. & Alvarez-Buylla, A. Neural stem cells: origin, heterogeneity and regulation in the adult mammalian brain. (2019). doi:10.1242/dev.156059

54. Wechsler-Reya, R. J. & Scott, M. P. Control of neuronal precursor proliferation in the cerebellum by sonic hedgehog. *Neuron* **22**, 103–114 (1999).

55. Lee, A. *et al*. Isolation of neural stem cells from the postnatal cerebellum. *Nat. Neurosci*. **8**, 723–729 (2005).

56. Aboody, K., Capela, A., Niazi, N., Stern, J. H. & Temple, S. Perspective Translating Stem Cell Studies to the Clinic for CNS Repair: Current State of the Art and the Need for a Rosetta Stone. (2011). doi:10.1016/j.neuron.2011.05.007

57. Kim, S. U. *et al*. Production and characterization of immortal human neural stem cell line with multipotent differentiation property. *Methods Mol. Biol*. **438**, 103–121 (2008).

58. Chu, K., Kim, M., Jeong, S. W., Kim, S. U. & Yoon, B. W. Human neural stem cells can migrate, differentiate, and integrate after intravenous transplantation in adult rats with transient forebrain ischemia. *Neurosci. Lett*. **343**, 129–133 (2003).

59. McKay, R. Stem cells in the central nervous system. *Science (80-.)*. **276**, 66–71 (1997).

60. Flax, J. D. *et al*. Engraftable human neural stem cells respond to developmental cues, replace neurons, and express foreign genes. *Nat. Biotechnol.* **16**, 1033–1039 (1998).

61. Aboody, K. S., Najbauer, J. & Danks, M. K. Stem and progenitor cell-mediated tumor selective gene therapy. *Gene Ther.* **15**, 739–752 (2008).

62. Barish, M. E. *et al*. Human Neural Stem Cell Biodistribution and Predicted Tumor Coverage by a Diffusible Therapeutic in a Mouse Glioma Model. *Stem Cells Transl. Med.* **6**, 1522–1532 (2017).

63. Aboody, K. S. *et al*. Neural stem cell-mediated enzyme/prodrug therapy for glioma: Preclinical studies. *Sci. Transl. Med.* **5**, 184ra59-184ra59 (2013).

64. ClinicalTrials.gov. Available at: https://clinicaltrials.gov/ct2/home. (Accessed: 28th May 2020)

65. A Pilot Feasibility Study of Oral 5-Fluorocytosine and Genetically-Modified Neural Stem Cells Expressing E.Coli Cytosine Deaminase for Treatment of Recurrent High Grade Gliomas - Tabular View - ClinicalTrials.gov. Available at: https://clinicaltrials.gov/ct2/show/record/NCT01172964. (Accessed: 30th May 2020)

66. Portnow, J. *et al*. Clinical Neural Stem Cell-Based Anticancer Gene Therapy: A First-in-Human Study in Recurrent High-Grade Glioma Patients. (2017). doi:10.1158/1078-0432.CCR-16-1518

67. Åkesson, E., Wolmer-Solberg, N., Cederarv, M., Falci, S. & Odeberg, J. Human neural stem cells and astrocytes, but not neurons, suppress an allogeneic lymphocyte response. *Stem Cell Res.* **2**, 56–67 (2009).

68. Bagó, J. R. *et al*. Therapeutically engineered induced neural stem cells are tumour-homing and inhibit progression of glioblastoma. *Nat. Commun.* **7**, 10593 (2016).

69. Bagó, J. R. *et al*. Tumor-homing cytotoxic human induced neural stem cells for cancer therapy. *Sci. Transl. Med.* **9**, eaah6510 (2017).

70. Ma, W. *et al*. Cell-extracellular matrix interactions regulate neural differentiation of human embryonic stem cells. *BMC Dev. Biol.* **8**, 1–13 (2008).

71. Pevny, L. H. & Nicolis, S. K. Sox2 roles in neural stem cells. *International Journal of Biochemistry and Cell Biology* **42**, 421–424 (2010).

72. Jane, E. P., Premkumar, D. R. & Pollack, I. F. Bortezomib sensitizes malignant human glioma cells to TRAIL, mediated by inhibition of the NF-κB signaling pathway. *Mol. Cancer Ther.* **10**, 198–208 (2011).

73. Johnstone, R. W., Frew, A. J. & Smyth, M. J. The TRAIL apoptotic pathway in cancer onset, progression and therapy. *Nature Reviews Cancer* **8**, 782–798 (2008).

74. Thiel, G. How Sox2 maintains neural stem cell identity. *Biochemical Journal* **450**, e1–e2 (2013).

75. Yu, J. *et al*. Induced pluripotent stem cell lines derived from human somatic cells. *Science (80-.)*. **318**, 1917–1920 (2007).

76. Eguchi, G. & Kodama, R. Transdifferentiation. *Curr. Opin. Cell Biol.* **5**, 1023–1028 (1993).

77. Nelakanti, R. V., Kooreman, N. G. & Wu, J. C. Teratoma Formation: A Tool for Monitoring Pluripotency in Stem Cell Research. *Curr. Protoc. Stem Cell Biol.* **32**, 4a.8.1-4a.8.17 (2015).

78. Buckely, A. *et al*. Generation and profiling of tumor-homing induced neural stem cells from the skin of cancer patients . *Mol. Ther.* **28**, (2020).

79. Patel, M. & Fisher, J. P. Biomaterial scaffolds in pediatric tissue engineering. *Pediatric Research* **63**, 497–501 (2008).

80. Zhang, X., Reagan, M. R. & Kaplan, D. L. Electrospun silk biomaterial scaffolds for regenerative medicine. *Advanced Drug Delivery Reviews* **61**, 988–1006 (2009).

81. Willerth, S. M. & Sakiyama-Elbert, S. E. Combining Stem Cells and Biomaterial Scaffolds for Constructing Tissues and Cell Delivery. *StemJournal* **1**, 1–25 (2019).

82. Nikolova, M. P. & Chavali, M. S. Recent advances in biomaterials for 3D scaffolds: A review. *Bioact. Mater.* **4**, 271–292 (2019).

83. Qu, H., Fu, H., Han, Z. & Sun, Y. Biomaterials for bone tissue engineering scaffolds: A review. *RSC Advances* **9**, 26252–26262 (2019).

84. Matson, J. B. & Stupp, S. I. Self-assembling peptide scaffolds for regenerative medicine. *Chem. Commun.* **48**, 26–33 (2012).

85. De Witte, T.-M., Fratila-Apachitei, L. E., Zadpoor, A. A. & Peppas, N. A. Bone tissue engineering via growth factor delivery: from scaffolds to complex matrices. *Regen. Biomater.* **5**, 197–211 (2018).

86. Ji, W. *et al*. Fibrous scaffolds loaded with protein prepared by blend or coaxial electrospinning. *Acta Biomater.* **6**, 4199–4207 (2010).

87. Calori, I. R., Braga, G., de Jesus, P. da C. C., Bi, H. & Tedesco, A. C. Polymer scaffolds as drug delivery systems. *Eur. Polym. J.* **129**, 109621 (2020).

88. Shan Wong, Y., Yong Tay, C., Wen, F., S. Venkatraman, S. & Poh Tan, L. Engineered Polymeric Biomaterials for Tissue Engineering. *Curr. Tissue Eng.* **1**, 41–53 (2012).

89. Jian, Z. *et al*. 3D bioprinting of a biomimetic meniscal scaffold for application in tissue

engineering. *Bioact. Mater.* **6**, 1711–1726 (2021).

90. Qu, W. *et al.* Polymer-Based Scaffold Strategies for Spinal Cord Repair and Regeneration. *Front. Bioeng. Biotechnol.* **8**, (2020).

91. Kourgiantaki, A. *et al.* Neural stem cell delivery via porous collagen scaffolds promotes neuronal differentiation and locomotion recovery in spinal cord injury. *NPJ Regen. Med.* **5**, 12 (2020).

92. Bozkurt, M. *et al.* Bilayer Matrix Autologous Chondrocyte Implantation without Bone Graft for Knee Osteochondral Lesion Less than 8 mm Deep. *J. Knee Surg.* **31**, 851–857 (2018).

93. FDA approves first autologous cellularized scaffold for the repair of cartilage defects of the knee | FDA. Available at: https://www.fda.gov/news-events/press-announcements/fda-approves-first-autologous-cellularized-scaffold-repair-cartilage-defects-knee. (Accessed: 17th February 2021)

94. GINTUIT (Allogeneic Cultured Keratinocytes and Fibroblasts in Bovine Collagen) | FDA. Available at: https://www.fda.gov/vaccines-blood-biologics/cellular-gene-therapy-products/gintuit-allogeneic-cultured-keratinocytes-and-fibroblasts-bovine-collagen. (Accessed: 17th February 2021)

95. Autologous Transplantation of Induced Pluripotent Stem Cell-Derived Retinal Pigment Epithelium for Geographic Atrophy Associated With Age-Related Macular Degeneration - Full Text View - ClinicalTrials.gov. Available at: https://www.clinicaltrials.gov/ct2/show/NCT04339764?term=scaffold&recrs=abdf&cntry=US&phase=04&draw=2&rank=7. (Accessed: 17th February 2021)

96. Bioengineered Penile Tissue Constructs for Irreversibly Damaged Penile Corpora - Full Text View - ClinicalTrials.gov. Available at: https://www.clinicaltrials.gov/ct2/show/NCT03463239?term=scaffold&recrs=abdf&cntry=US&phase=04&draw=2&rank=5. (Accessed: 17th February 2021)

97. Safety and Feasibility Study of Autologous Engineered Urethral Constructs for the Treatment of Strictures - Full Text View - ClinicalTrials.gov. Available at: https://www.clinicaltrials.gov/ct2/show/NCT03258658?term=scaffold&recrs=abdf&cntry=US&phase=04&draw=2&rank=3. (Accessed: 17th February 2021)

98. Natural Vascular Scaffold (NVS) Therapy for Treatment of Atherosclerotic Lesions - Full Text View - ClinicalTrials.gov. Available at: https://www.clinicaltrials.gov/ct2/show/NCT04188262?term=scaffold&recrs=abdf&cntry=US&phase=04&draw=2&rank=2. (Accessed: 17th February 2021)

99. Michel, J., Clavreul, A. & Menei, P. Intratumoral heterogeneity in glioblastoma: Don't forget the peritumoral brain zone. *Neuro. Oncol.* **17**, 1322–1332 (2015).

100. Zheng, L. *et al.* Scalp block for glioblastoma surgery is associated with lower

inflammatory scores and improved survival. *Minerva Anestesiol*. **83**, 1137–1145 (2017).

101. Moore, K. M. *et al*. Impact of composite scaffold degradation rate on neural stem cell persistence in the glioblastoma surgical resection cavity. *Mater. Sci. Eng. C* **111**, 110846 (2020).

102. Bagó, J. R. *et al*. Fibrin matrices enhance the transplant and efficacy of cytotoxic stem cell therapy for post-surgical cancer. *Biomaterials* **84**, 42–53 (2016).

103. Sheets, K. T. *et al*. Developing Implantable Scaffolds to Enhance Neural Stem Cell Therapy for Post-Operative Glioblastoma. *Mol. Ther*. **28**, 1056–1067 (2020).

104. Kauer, T. M., Figueiredo, J.-L., Hingtgen, S. & Shah, K. Encapsulated therapeutic stem cells implanted in the tumor resection cavity induce cell death in gliomas. *Nat. Neurosci*. **15**, 197–204 (2011).

105. Efficacy for Newly Diagnosed Glioblastoma (GBM) |Optune®. Available at: https://www.optune.com/hcp/newly-diagnosed-glioblastoma/efficacy. (Accessed: 17th February 2021)

106. Pisapia, D. J. The Updated World Health Organization Glioma Classification Cellular and Molecular Origins of Adult Infiltrating Gliomas. *Arch Pathol Lab Med* **141**, 1633–1645 (2017).

107. Davis, M. E. Glioblastoma: Overview of Disease and Treatment. *Clin. J. Oncol. Nurs*. **20**, S2-8 (2016).

108. Alifieris, C. & Trafalis, D. T. Glioblastoma multiforme: Pathogenesis and treatment. *Pharmacology and Therapeutics* **152**, 63–82 (2015).

109. Mittal, S. *et al*. Alternating electric tumor treating fields for treatment of glioblastoma: Rationale, preclinical, and clinical studies. *J. Neurosurg*. **128**, 414–421 (2018).

110. Aboody, K. S. *et al*. Neural stem cells display extensive tropism for pathology in adult brain: Evidence from intracranial gliomas. *PNAS* **97**, 12846–128551 (2000).

111. Kim, S. K. *et al*. Human neural stem cells target experimental intracranial medulloblastoma and deliver a therapeutic gene leading to tumor regression. *Clin. Cancer Res*. **12**, 5550–5556 (2006).

112. ClinicalTrials.gov [Internet]. Bethesda Identifier NCT02015819, (US). Genetically Modified Neural Stem Cells, Flucytosine, and Leucovorin for Treating Patients With Recurrent High-Grade Gliomas. (2013). Available at: https://clinicaltrials.gov/ct2/show/NCT02015819?id=NCT02015819&draw=2&rank=1. (Accessed: 12th February 2020)

113. (US)., C. go. [Internet]. B. (MD): N. L. of M. & Identifier NCT02192359, (US). Carboxylesterase-Expressing Allogeneic Neural Stem Cells and Irinotecan Hydrochloride

in Treating Patients With Recurrent High-Grade Gliomas. (2014). Available at: https://clinicaltrials.gov/ct2/show/NCT02192359?id=NCT02192359&draw=2&rank=1. (Accessed: 12th February 2020)

114. ClinicalTrials.gov [Internet]. Bethesda (MD): National Library of Medicine Identifier NCT02055196, (US). Genetically Modified Stem Cells and Irinotecan Hydrochloride in Treating Patients With Recurrent High-Grade Gliomas. (2014). Available at: https://clinicaltrials.gov/ct2/show/NCT02055196?id=NCT02055196&draw=2&rank=1. (Accessed: 12th February 2020)

115. (US)., C. go. [Internet]. B. (MD): N. L. of M. & Identifier NCT01172964, (US). A Pilot Feasibility Study of Oral 5-Fluorocytosine and Genetically-Modified Neural Stem Cells Expressing E.Coli Cytosine Deaminase for Treatment of Recurrent High Grade Gliomas. (2010). Available at: https://clinicaltrials.gov/ct2/show/NCT01172964?id=NCT01172964&draw=2&rank=1. (Accessed: 12th February 2020)

116. (US)., C. go. [Internet]. B. (MD): N. L. of M. & Identifier NCT03072134, (US). Neural Stem Cell Based Virotherapy of Newly Diagnosed Malignant Glioma. (2017). Available at: https://clinicaltrials.gov/ct2/show/NCT03072134?id=NCT03072134&draw=2&rank=1. (Accessed: 12th February 2020)

117. Aleynik, A. *et al*. Stem cell delivery of therapies for brain disorders. *Clin. Transl. Med.* **3**, 24 (2014).

118. Bovenberg, M. S. S., Degeling, M. H. & Tannous, B. A. Advances in stem cell therapy against gliomas. *Trends Mol. Med.* **19**, 281–291 (2013).

119. Bagó, J. R. *et al*. Electrospun nanofibrous scaffolds increase the efficacy of stem cell-mediated therapy of surgically resected glioblastoma. *Biomaterials* **90**, 116–125 (2016).

120. European Medicines Agency. Medical device: Floseal hemostatic matrix (VH S/D). *Consultation procedure public assessment report (CPAR)* (2012). Available at: https://www.ema.europa.eu/en/documents/other/consultation-ancillary-medicinal-substance-incorporated-medical-device-floseal-haemostatic-matrix/d_en.pdf. (Accessed: 27th January 2021)

121. FLOSEAL Hemostatic Matrix, 5 mL Instructions for Use. Available at: https://advancedsurgery.baxter.com/sites/g/files/ebysai1521/files/2019-02/Floseal FSP IFU - 5ml.pdf. (Accessed: 12th February 2020)

122. Davie, E. W., Fujikawa, K. & Kisiel, W. Perspectives in Biochemistry The Coagulation Cascade: Initiation, Maintenance, and Regulation. *Biochemistry* **30**, 10363–10370 (1991).

123. Menon, N. V. *et al*. Microfluidic Assay To Study the Combinatorial Impact of Substrate Properties on Mesenchymal Stem Cell Migration. *ACS Appl. Mater. Interfaces* **7**, 17095–17103 (2015).

124. Pathak, A. & Kumar, S. Independent regulation of tumor cell migration by matrix stiffness and confinement. *Proc. Natl. Acad. Sci. U. S. A.* **109**, 10334–10339 (2012).

125. Charrier, E. E., Pogoda, K., Wells, R. G. & Janmey, P. A. Control of cell morphology and differentiation by substrates with independently tunable elasticity and viscous dissipation. *Nat. Commun.* **9**, 1–13 (2018).

126. Saha, K. *et al.* Substrate Modulus Directs Neural Stem Cell Behavior. *Biophys. J.* **95**, 4426–4438 (2008).

127. Shi, D. *et al.* Photo-Cross-Linked Scaffold with Kartogenin-Encapsulated Nanoparticles for Cartilage Regeneration. *ACS Nano* **10**, 1292–1299 (2016).

128. Wolberg, A. S. Thrombin generation and fibrin clot structure. *Blood Rev.* **21**, 131–142 (2007).

129. Bozec, L. & Odlyha, M. Thermal denaturation studies of collagen by microthermal analysis and atomic force microscopy. *Biophys. J.* **101**, 228–236 (2011).

130. Wong, M. L., Wong, J. L., Vapniarsky, N. & Griffiths, L. G. In vivo xenogeneic scaffold fate is determined by residual antigenicity and extracellular matrix preservation. *Biomaterials* **92**, (2016).

131. Puckert, C. *et al.* Molecular interactions and forces of adhesion between single human neural stem cells and gelatin methacrylate hydrogels of varying stiffness. *Acta Biomater.* **106**, 156–169 (2020).

132. Li, L. *et al.* Effects of cytokines and chemokines on migration of mesenchymal stem cells following spinal cord injury. *Neural Regen. Res.* **7**, 1106–1112 (2012).

133. Xu, F. *et al.* Chemokines mediate mesenchymal stem cell migration toward gliomas in vitro. *Oncol. Rep.* **31**, 1265–1270 (2010).

134. Vogel, C. & Marcotte, E. M. Insights into the regulation of protein abundance from proteomic and transcriptomic analyses. *Nat. Rev. Genet.* **13**, 227–232 (2012).

135. Crommentuijn, M. H. W. *et al.* Intracranial AAV-sTRAIL combined with lanatoside C prolongs survival in an orthotopic xenograft mouse model of invasive glioblastoma. *Mol. Oncol.* **10**, 625–634 (2016).

136. Wang, S. shan *et al.* miR-133a Promotes TRAIL Resistance in Glioblastoma via Suppressing Death Receptor 5 and Activating NF-κB Signaling. *Mol. Ther. - Nucleic Acids* **8**, 482–492 (2017).

137. Fernandes, C. *et al.* Current Standards of Care in Glioblastoma Therapy. in *Glioblastoma* (ed. De Vleeschouwer, S.) 197–241 (Codon Publications, 2017). doi:10.15586/codon.glioblastoma.2017.ch11

138. Deeken, J. F. & Lo« Scher, W. The Blood-Brain Barrier and Cancer: Transporters,Treatment, and Trojan Horses. *Clin. Cancer Res.* **13**, 1663–1674 (2007).

139. Lipsitz, D. *et al.* Glioblastoma multiforme: clinical findings, magnetic resonance imaging, and pathology in five dogs. *Vet. Pathol.* **40**, 659–69 (2003).

140. Nakamizo, A. *et al. Human Bone Marrow-Derived Mesenchymal Stem Cells in the Treatment of Gliomas*. (2005).

141. Reagan, M. R. & Kaplan, D. L. Concise Review: Mesenchymal Stem Cell Tumor-Homing: Detection Methods in Disease Model Systems. *Stem Cells* **29**, 920–927 (2011).

142. James, B. R. & Griffith, T. S. Tumor necrosis factor-related apoptosis-inducing ligand-induced apoptotic pathways in cancer immunosurveillance: molecular mechanisms and prospects for therapy. *Res. Reports Biochem.* **5**, (2015).

143. Kelley, S. K. *et al.* Preclinical Studies to Predict the Disposition of Apo2L/Tumor Necrosis Factor-Related Apoptosis-Inducing Ligand in Humans: Characterization of in Vivo Efficacy, Pharmacokinetics, and Safety. *J. Pharmacol. Exp. Ther.* **299**, 31–38 (2001).

144. Ashkenazi, A. *et al.* Safety and antitumor activity of recombinant soluble Apo2 ligand. *J. Clin. Invest.* **104**, 155–162 (1999).

145. Fulda, S., Wick, W., Weller, M. & Debatin, K. M. Smac agonists sensitize for Apo2L/TRAIL-or anticancer drug-induced apoptosis and induce regression of malignant glioma in vivo. *Nat. Med.* **8**, 808–815 (2002).

146. Holoch, P. A. & Griffith, T. S. TNF-related apoptosis-inducing ligand (TRAIL): A new path to anti-cancer therapies. (2009). doi:10.1016/j.ejphar.2009.06.066

147. Cvetkovic, R. S. & Wellington, K. Valganciclovir A Review of its Use in the Management of CMV Infection and Disease in Immunocompromised Patients. *Drugs* **65**, 859–878 (2005).

148. Kim, Y. G., Bi, W., Feliciano, E. S., Drake, R. R. & Stambrook, P. J. Ganciclovir-mediated cell killing and bystander effect is enhanced in cells with two copies of the herpes simplex virus thymidine kinase gene. *Cancer Gene Ther.* **7**, 240–246 (2000).

149. Kauffman, M. G., Rose, P. A. & Kelly, T. J. Mutations in the Thymidine Kinase Gene That Allow Expression of the Enzyme in Quiescent (G0) Cells - PubMed. *Oncogene* **6**, 1427–1435 (1991).

150. Hossain, J. A. *et al.* Long-term treatment with valganciclovir improves lentiviral suicide gene therapy of glioblastoma. *Neuro. Oncol.* **21**, 890–900 (2019).

151. Hossain, J. A. *et al.* Lentiviral HSV-Tk.007-mediated suicide gene therapy is not toxic for normal brain cells. *J. Gene Med.* **18**, 234–243 (2016).

152. Cohen-Pfeffer, J. L. *et al*. Intracerebroventricular Delivery as a Safe, Long-Term Route of Drug Administration. *Pediatr. Neurol.* **67**, 23–35 (2017).

153. Oz, M. C., Rondinone, J. F. & Shargill, N. S. Floseal Matrix:. New Generation Topical Hemostatic Sealant. *J. Card. Surg.* **18**, 486–493 (2003).

154. Feng, X. *et al*. Effect of optimized collagenase digestion on isolated and cultured nucleus pulposus cells in degenerated intervertebral discs. *Med. (United States)* **97**, (2018).

155. Kotton, D. N., Mostoslavsky, G. & Murphy, G. J. SOP for Human Dermal Fibroblast Isolation. *Ce* (2010). Available at: https://www.bu.edu/dbin/stemcells/files/Human dermal fibroblast isolation.pdf. (Accessed: 26th November 2018)

156. Lee, N. K. *et al*. Magnetic Resonance Imaging of Ferumoxytol-Labeled Human Mesenchymal Stem Cells in the Mouse Brain. *Stem Cell Rev. Reports* **13**, 127–138 (2017).

157. Khurana, A. *et al*. Ferumoxytol: A new, clinically applicable label for stem-cell tracking in arthritic joints with MRI. *Nanomedicine* **8**, 1969–1983 (2013).

158. Bashir, M. R., Bhatti, L., Marin, D. & Nelson, R. C. Emerging applications for ferumoxytol as a contrast agent in MRI. *J. Magn. Reson. Imaging* **41**, 884–898 (2015).

159. Gutova, M. *et al*. Magnetic Resonance Imaging Tracking of Ferumoxytol-Labeled Human Neural Stem Cells: Studies Leading to Clinical Use. *Stem Cells Transl. Med.* **2**, 766–775 (2013).

160. Mcbride, W. Subdural hematoma in adults: Prognosis and management. *UpToDate* (2020). Available at: https://www-uptodate-com.libproxy.lib.unc.edu/contents/subdural-hematoma-in-adults-prognosis-and-management?search=cerebral hematoma&source=search_result&selectedTitle=2~150&usage_type=default&display_rank=2#H7. (Accessed: 20th February 2020)

161. Venton, G. *et al*. Risk factors of Ganciclovir-related neutropenia after allogeneic stem cell transplantation: A retrospective monocentre study on 547 patients. *Clin. Microbiol. Infect.* **20**, 160–166 (2014).

162. Nihi, F. *et al*. Testicular effects following in utero exposure to the antivirals acyclovir and ganciclovir in rats. *Toxicol. Sci.* **139**, 220–233 (2014).

163. Faqi, A. S., Klug, A., Merker, H. J. & Chahoud, I. Ganciclovir induces reproductive hazards in mate rats after short-term exposure. *Hum. Exp. Toxicol.* **16**, 505–511 (1997).

164. Valganciclovir: Drug information. *UpToDate* (2020). Available at: https://www-uptodate-com.libproxy.lib.unc.edu/contents/valganciclovir-drug-information?search=valganciclovir drug information&source=panel_search_result&selectedTitle=1~49&usage_type=panel&kp_tab=drug_general&display_rank=1. (Accessed: 18th February 2020)

165. Portnow, J. *et al*. Neural stem cell-based anticancer gene therapy: A first-in-human study in recurrent high-grade glioma patients. *Clin. Cancer Res.* **23**, 2951–2960 (2017).

166. Thaci, B. *et al*. Pharmacokinetic study of neural stem cell-based cell carrier for oncolytic virotherapy: targeted delivery of the therapeutic payload in an orthotopic brain tumor model. *Cancer Gene Ther.* **19**, 431–442 (2012).

167. Robertson, F. L., Marqués, M.-A., Torrejón, M.-T., Morrison, G. M. & Pollard, S. M. Experimental models and tools to tackle glioblastoma. (2019). doi:10.1242/dmm.040386

168. Chen, L., Zhang, Y., Yang, J., Hagan, J. P. & Li, M. Vertebrate animal models of glioma: Understanding the mechanisms and developing new therapies. *Biochim Biophys Acta* **1836**, 158–165 (2013).

169. Berweiler, U., Krone, A. & Tonn, J. C. *Reservoir systems for intraventricular chemotherapy. Z Journal of Neuro-Oncology* **38**, (1998).

170. Ganipineni, L. P., Danhier, F. & Préat, V. Drug delivery challenges and future of chemotherapeutic nanomedicine for glioblastoma treatment. *J. Control. Release* **281**, 42–57 (2018).

171. Burnet, N. G., Jefferies, S. J., Benson, R. J., Hunt, D. P. & Treasure, F. P. Years of life lost (YLL) from cancer is an important measure of population burden - And should be considered when allocating research funds. *Br. J. Cancer* **92**, 241–245 (2005).

172. Ohgaki, H. Epidemiology of Brain Tumors. in *Cancer Epidemiology: Modifiable Factors* (ed. Verma, M.) 323–342 (Humana Press, 2009). doi:10.1007/978-1-60327-492-0_14

173. Aboody, K. S. *et al*. Neural stem cells display extensive tropism for pathology in adult brain: Evidence from intracranial gliomas. *Proc. Natl. Acad. Sci.* **97**, 12846–12851 (2000).

174. Owonikoko, T. K. *et al*. Current approaches to the treatment of metastatic brain tumours. *Nat. Rev. Clin. Oncol.* **11**, 203–222 (2014).

175. Dey, M. *et al*. Intranasal Oncolytic Virotherapy with CXCR4-Enhanced Stem Cells Extends Survival in Mouse Model of Glioma. *Stem Cell Reports* **7**, 471–482 (2016).

176. Lettry, V., Hagler, S. B., Khagi, S. & Hingtgen, S. D. Tumor-homing stem cell therapy for brain cancer. *Curr. Surg. Reports* **5**, (2017).

177. Metz, M. Z. *et al*. Neural Stem Cell-Mediated Delivery of Irinotecan-Activating Carboxylesterases to Glioma: Implications for Clinical Use. *Stem Cells Transl. Med.* **2**, 983–992 (2013).

178. Ahmed, A. U. *et al*. Neural stem cell-based cell carriers enhance therapeutic efficacy of an oncolytic adenovirus in an orthotopic mouse model of human glioblastoma. *Mol. Ther.* **19**, 1714–1726 (2011).

179. Mooney, R. *et al*. Neural stem cells improve intracranial nanoparticle retention and tumor-selective distribution. *Futur. Oncol.* **10**, 401–415 (2014).

180. Zhang, N. *et al*. Soft Hydrogels Featuring In-Depth Surface Density Gradients for the Simple Establishment of 3D Tissue Models for Screening Applications. *SLAS Discov. Adv. Life Sci. R&D* **22**, 635–644 (2017).

181. Haessler, U., Kalinin, Y., Swartz, M. A. & Wu, M. An agarose-based microfluidic platform with a gradient buffer for 3D chemotaxis studies. *Biomed. Microdevices* **11**, 827–835 (2009).

182. Zhang, Z.-N. *et al*. Layered hydrogels accelerate iPSC-derived neuronal maturation and reveal migration defects caused by MeCP2 dysfunction. *Proceedings of the National Academy of Sciences of the United States of America* **113**, 3185–90 (2016).

183. Pradhan, S., Hassani, I., Clary, J. M. & Lipke, E. A. Polymeric Biomaterials for In Vitro Cancer Tissue Engineering and Drug Testing Applications. *Tissue Eng. Part B Rev.* **22**, 470–484 (2016).

184. Bonetto, F. *et al*. A large-scale 19F MRI-based cell migration assay to optimize cell therapy. *NMR Biomed.* **25**, 1095–1103 (2012).

185. Tam, R. Y., Smith, L. J. & Shoichet, M. S. Engineering Cellular Microenvironments with Photo- and Enzymatically Responsive Hydrogels: Toward Biomimetic 3D Cell Culture Models. *Acc. Chem. Res.* **50**, 703–713 (2017).

186. Kendall, S. E. *et al*. Neural Stem Cell Targeting of Glioma Is Dependent on Phosphoinositide 3-Kinase Signaling. *Stem Cells* **26**, 1575–1586 (2008).

187. Salehi-Nik, N. *et al*. Engineering Parameters in Bioreactor's Design: A Critical Aspect in Tissue Engineering. *Biomed Res. Int.* **2013**, 15 (2013).

188. Lee, H. Y. *et al*. C-MYC drives breast cancer metastasis to the brain, but promotes synthetic lethality with TRAIL. *Mol. Cancer Res.* **17**, 544–554 (2019).

189. Okolie, O. *et al*. Reactive astrocytes potentiate tumor aggressiveness in a murine glioma resection and recurrence model. *Neuro. Oncol.* **18**, 1622–1633 (2018).

190. An, J. *et al*. Effects of FSTL1 on cell proliferation in breast cancer cell line MDA-MB-231 and its brain metastatic variant MDA-MB-231-BR. *Oncol. Rep.* **38**, 3001–3010 (2017).

191. Kim, S.-H. Investigating breast cancer metastasis to brain in pre-clinical mouse models of metastasis. (2016).

192. Wang, H.-L., Miyauchi, M. & Takata, T. Migration of osteoblastic cells on various guided bone regeneration membranes. *Clin. Oral Impl. Res* **12**, 332–338 (2001).

193. Shah, A. R. *et al*. Migration of Co-cultured Endothelial Cells and Osteoblasts in

Composite Hydroxyapatite/Polylactic Acid Scaffolds. *Ann. Biomed. Eng.* **39**, 2501–2509 (2011).

194. Bružauskaitė, I., Bironaitė, D., Bagdonas, E. & Bernotienė, E. Scaffolds and cells for tissue regeneration: different scaffold pore sizes—different cell effects. *Cytotechnology* **68**, 355–369 (2016).

195. Barnes, C. P., Sell, S. A., Boland, E. D., Simpson, D. G. & Bowlin, G. L. Nanofiber technology: Designing the next generation of tissue engineering scaffolds. *Adv. Drug Deliv. Rev.* **59**, 1413–1433 (2007).

196. McCullen, S. D. *et al.* Characterization of electrospun nanocomposite scaffolds and biocompatibility with adipose-derived human mesenchymal stem cells. *Int. J. Nanomedicine* **2**, 253–63 (2007).

197. Pomfret, R., Miranpuri, G. & Sillay, K. The substitute brain and the potential of the gel model. *Ann. Neurosci.* **20**, 118–22 (2013).

198. Gillies, G. T., Allison, S. W. & Tissue, B. M. Positive pressure infusion of fluorescent nanoparticles as a probe of the structure of brain phantom gelatins. *Nanotechnology* **13**, 308 (2002).

199. Shih, H.-C. *et al.* Microfluidic Collective Cell Migration Assay for Study of Endothelial Cell Proliferation and Migration under Combinations of Oxygen Gradients, Tensions, and Drug Treatments. *Sci. Rep.* **9**, 8234 (2019).

200. Rørth, P. Collective Cell Migration. *Annu. Rev. Cell Dev. Biol.* **25**, 407–429 (2009).

201. Amberg, R. *et al.* Design of a migration assay for human gingival fibroblasts on biodegradable magnesium surfaces. *Acta Biomater.* **79**, 158–167 (2018).

202. Rijal, G. *et al.* Porcine breast extracellular matrix hydrogel for spatial tissue culture. *Int. J. Mol. Sci.* **19**, (2018).

203. Banerjee, A. *et al.* The influence of hydrogel modulus on the proliferation and differentiation of encapsulated neural stem cells. *Biomaterials* **30**, 4695–4699 (2009).

204. Georges, P. C. & Janmey, P. A. Cell type-specific response to growth on soft materials. *J. Appl. Physiol.* **98**, 1547–1553 (2005).

205. Levental, I., Georges, P. C. & Janmey, P. A. Soft biological materials and their impact on cell function. *Soft Matter* **3**, 299–306 (2007).

206. iDISCO protocol. (2015). Available at: https://idisco.info/idisco-protocol/. (Accessed: 15th September 2018)

207. Shah, K. *et al.* Bimodal Viral Vectors and In Vivo Imaging Reveal the Fate of Human Neural Stem Cells in Experimental Glioma Model. *J. Neurosci.* **28**, 4406–4413 (2008).

208. Perla, K. M. Ri., Venegas, O. G. & Toms, S. A. *Chemradiation treatment of glioblastoma multiforme: Treatment guidelines and considerations*. (2019).

209. K., S. Stem cell-based therapies for tumors in the brain: Are we there yet? *Neuro. Oncol.* **18**, 1066–1078 (2016).

210. Normand, V., Lootens, D. L., Amici, E., Plucknett, K. P. & Aymard, P. New Insight into Agarose Gel Mechanical Properties. *Biomacromolecules* **1**, 730–738 (2000).

211. Tumbleston, J. R. *et al*. Continuous liquid interface production of 3D objects. *Science (80-.).* **347**, 1349–1352 (2015).

212. Desimone, J. M., Ermoshkin, A., Ermoshkin, N. & Sarnulski, E. T. Continuous liquid interphase printing. (2014).

213. Bloomquist, C. J. *et al*. Controlling release from 3D printed medical devices using CLIP and drug-loaded liquid resins. *J. Control. Release* **278**, 9–23 (2018).

214. Carbon | Life Sciences. (2021). Available at: https://www.carbon3d.com/industries/life-sciences/. (Accessed: 18th February 2021)

215. Ware, H. O. T., Farsheed, A. C., Baker, E., Ameer, G. & Sun, C. Fabrication Speed Optimization for High-resolution 3D-printing of Bioresorbable Vascular Scaffolds. in *Procedia CIRP* **65**, 131–138 (Elsevier B.V., 2017).

216. Deng, X. *et al*. 3D printing of robust and biocompatible poly(ethylene glycol)diacrylate/nano-hydroxyapatite composites via continuous liquid interface production . *J. Mater. Chem. B* **9**, 1315–1324 (2021).

217. Ware, H. O. T. *et al*. High-speed on-demand 3D printed bioresorbable vascular scaffolds. *Mater. Today Chem.* **7**, 25–34 (2018).

218. Godbe, J. M. *et al*. Gelator Length Precisely Tunes Supramolecular Hydrogel Stiffness and Neuronal Phenotype in 3D Culture. *ACS Biomater. Sci. Eng.* **6**, 1196–1207 (2020).

219. Dems, D. *et al*. Multivalent Clustering of Adhesion Ligands in Nanofiber-Nanoparticle Composites. *Acta Biomater.* **119**, 303–311 (2021).

220. Daly, M. L., Klawa, S. J. & Freeman, R. New Functions Emerging from Peptide-DNA Materials. in *Peptide-based Biomaterials* (ed. Guler, M. O.) 459–486 (2021).